-8872 108 P.

cs W080217I

AR 86-2

Aeronautical Report 86-2

THEORETICAL ANALYSIS OF THE ELECTRICAL ASPECTS OF THE BASIC ELECTRO-IMPULSE PROBLEM IN AIRCRAFT DE-ICING APPLICATIONS

BY

Robert A. Henderson
and
Robert L. Schrag

Aeronautical Engineering Department
Wichita State University
Wichita, Kansas 67208

Technical Report
for
NASA Lewis Research Center (NAG-3-284)
NASA Technical Monitor: J. J. Reimann

June 1986

(NASA-CR-176808) THEORETICAL ANALYSIS OF THE ELECTRICAL ASPECTS OF THE BASIC ELECTRO-IMPULSE PROBLEM IN AIRCRAFT DE-ICING APPLICATIONS (Wichita State Univ.) 108 p HC A06/MF A01 CSCL 01C G3/05

N86-26330
Unclas
43454 8872

Preface

This report is a part of the research and development project on aircraft de-icing by the electromagnetic impulse method. This project has been sponsored by the Lewis Research Center of the National Aeronautics and Space Administration under grant number NAG-3-284. The grant administrator was Mr. John J. Reinmann. For the previous four years, many tests had been run in the NASA Icing Research Tunnel and three sets of flight tests were performed. These, plus various laboratory tests, have resulted in a semi-empirical technology for designing an electro-impulse de-icing (EIDI) system.

However, the empirical method is inadequate when a very different geometry, material or size is encountered. A computative solution is needed which permits prediction of the de-icing effect for a given configuration and electrical circuitry. This report, which is principally the Ph.D. dissertation of Robert A. Henderson under the direction of Prof. Robert L. Schrag, attempts to do the first part of a full computer simulation of EIDI. The pressure/time produced by the method in this report would be necessary input for a computer code giving the structural dynamic response of a given configuration. The configurations in mind are leading edge portions of aircraft wings, engine nacelle inlets and rotor blades. Applications, however, are not limited to these applications.

The author acknowledges the assistance of NASA-Lewis Research Center, both for the support of the whole EIDI project at Wichita State University and for the opportunity to work at NASA-Lewis during the summer of 1985. The assistance of Drs. R. Joseph Shaw, Bill Ford and Avram Sidi during that time is gratefully expressed.

TABLE OF CONTENTS

		PAGE
1.	INTRODUCTION	1
	1.1 Electro-Impulse Phenomenon and De-Icing	1
	1.2 Scope of Dissertation	3
	1.3 Organization of Dissertation	3
2.	THE ELECTRIC CIRCUIT MODEL	8
3.	TRANSMISSION LINE MODEL OF THE FIELD PROBLEM	12
	3.1 Introduction	12
	3.2 Geometry of a Prototype EIDI System	12
	3.3 The Field Equations	14
	3.4 Development of the Transmission Line Model	16
4.	ANALYSIS STRUCTURE	22
	4.1 Introduction	22
	4.2 Method of Calculating Coil Impedance	22
	4.3 Radial Magnetic Induction and Azimuthal Electric Intensity	25
	4.3.1 Target Surface Facing Coil	25
	4.3.2 Target Surface Opposite Coil	30
	4.4 Calculation of the Axial Magnetic Field Using the Transmission Line Model	31
	4.5 Force Between Target and Coil	32
	4.6 Impulse Delivered to Target	33
5.	A SPECIFIC SYSTEM EXAMPLE, INCLUDING EXPERIMENTAL RESULTS	34
	5.1 Definition of the System	34
	5.2 Coil Impedance Measurements	36
	5.3 Current Waveform	36
	5.4 Magnetic Field Measurements	37
	5.5 Measurement of Impulse to Target	41
6.	COMPUTER ANALYSIS ON THE SYSTEM EXAMPLE	42
	6.1 Introduction	42
	6.2 Coil Impedance	42
	6.3 Current Waveform	45
	6.3.1 Introduction	45
	6.3.2 Current Before Clamp Diode Conduction	47
	6.3.3 Current After Clamp Diode Conduction	50
	6.3.4 Combining Pre- and Post Clamp Diode Conduction Current	52
	6.4 Magnetic Induction	53

6.4.1 Introduction 53
6.4.2 Radial Magnetic Induction on the Coil Side Face of the Target 54
6.4.3 Axial Magnetic Induction on the Coil Side Face of the Target 58
6.4.4 Magnetic Induction on the Opposite Face of the Target 60
6.5 Force Versus Time 62
6.6 Impulse 65

7. CONCLUSION AND RECOMMENDATIONS FOR FURTHER WORK 67

7.1 Conclusion 67
7.1.1 Summary 67
7.1.2 Contributions by the Author 68
7.2 Recommendations for Future Work 69

APPENDIX A: FORTRAN SOURCE CODE FOR CALCULATING COIL RESISTANCE INCREASE DUE TO TARGET 72

APPENDIX B: FORTRAN SOURCE CODE FOR CALCULATING COIL CURRENT BEFORE CLAMP DIODE CONDUCTION 76

APPENDIX C: CALCULATION OF $K'(\lambda)$ 79

APPENDIX D: FORTRAN SOURCE CODE FOR CALCULATING RADIAL TIME DOMAIN MAGNETIC INDUCTION ON THE COIL SIDE SURFACE OF THE TARGET 83

APPENDIX E: FORTRAN SOURCE CODE FOR FORCE CALCULATION AT TIME T=50 MICROSECONDS 95

APPENDIX F: NOTATION AND LIST OF SYMBOLS 97

REFERENCES 102

VITA 105

CHAPTER ONE

INTRODUCTION

1.1 ELECTRO-IMPULSE PHENOMENON AND DE-ICING

In a paper presented January 8, 1986, at the 24th AIAA Aerospace Sciences Meeting in Reno, Nevada, [1] author R. D. Rudich cited aircraft icing as the direct cause of four of the thirty two weather related fatal accidents reported in the paper. While this may not seem like a significant number, the loss of human lives in these four accidents could have been prevented if the aircraft involved had been able to cope successfully with the icing conditions they encountered.

The purpose of this dissertation is to present methods of analyzing the electromagnetic aspects of a new method of de-icing both private and commercial aircraft. This new de-icing method, referred to as Electro Impulse De-Icing (abbreviated EIDI), holds the promise of being superior to the present aircraft de-icing methods in terms of the energy expended in removing accreted ice [42].

The EIDI concept is not new. In May 1939, Great Britain issued a patent to Mr. Rudolf Goldschmidt covering the basic EIDI mechanism [2]. However, no commercial development of an EIDI system in the free world proceeded from this patent. It has only been within the last 5 years that the unavailability of bleed air from the new high bypass ratio engines used on the next generation commercial aircraft has caused attention to again be directed to the commercial use of an EIDI system for removing ice from aircraft.

The simplest practical EIDI system consists of a spirally wound coil of rectangular cross section conductor mounted with its axis of symmetry perpendicular to the metal surface to be de-iced. An initially charged capacitor is discharged through this coil, and the resulting magnetic field from the coil's current causes eddy currents in the metal. The force exerted on these eddy currents by the coil's magnetic field is initially in such a direction as to cause the coil and the metal surface to separate. It is this force that causes ice on the metal surface to crack, and subsequently to be removed from the surface.

A considerable body of literature concerned with the electromagnetic aspects of a coil placed next to a conducting surface has accumulated. Levy [8] and Grover [9] present methods of calculating terminal impedances. Dodd and Deeds [10] discuss both impedance calculations and eddy current distributions. Onoe [11] is apparently the first researcher to apply a Hankel transformation in the calculation of impedances. Onoe's method is further developed and extended by El-Markabi and Freeman [4] to include calculation of the force between the coil and conductor when the coil current is a sinusoid. Bowley et. al. [43] discuss the use of the magnetic vector potential in calculating the impulse delivered to the conductor by a transient current in the coil. Lewis [44] summarizes the use of the Bowley et. al. method for designing a coil to deliver a specific impulse in an electro-impulse de-icing installation.

1.2 SCOPE OF DISSERTATION

An experimental set-up of a prototype EIDI system was assembled at The Wichita State University by Dr. Robert Schrag. An experimental study of the electro-impulse phenomenon in this system was made by Dr. Schrag utilizing field diagnostics methods [3]. Axial and radial components of the magnetic field were measured on both sides of the rigidly held aluminum "target" plate. The data were then used to deduce the total mechanical force versus time, and the mechanical impulse strength. Impulse strength was also measured directly with a ballistic pendulum. This experimental study provided results which will be used to verify theoretical predictions from the mathematical model used in this dissertation.

In this dissertation, the physical phenomena involved in the prototype EIDI system of Dr. Schrag's experiment will be investigated analytically and numerically. Specifically, the following tasks will be undertaken.

1. A mathematical model for the total electrical problem will be devised. It will employ a transmission line analogy to handle the electromagnetic field portion of the system, and a frequency domain model for the circuit portion.

2. The math model will be solved by computer for the specific set of conditions that existed in Dr. Schrag's diagnostics experiment, and the calculated and experimental results will be compared.

1.3 ORGANIZATION OF DISSERTATION

Figure 1 summarizes the analysis structure developed in this dissertation to predict the behavior of the prototype EIDI system briefly described in Section 1.1. Each of the blocks in this figure

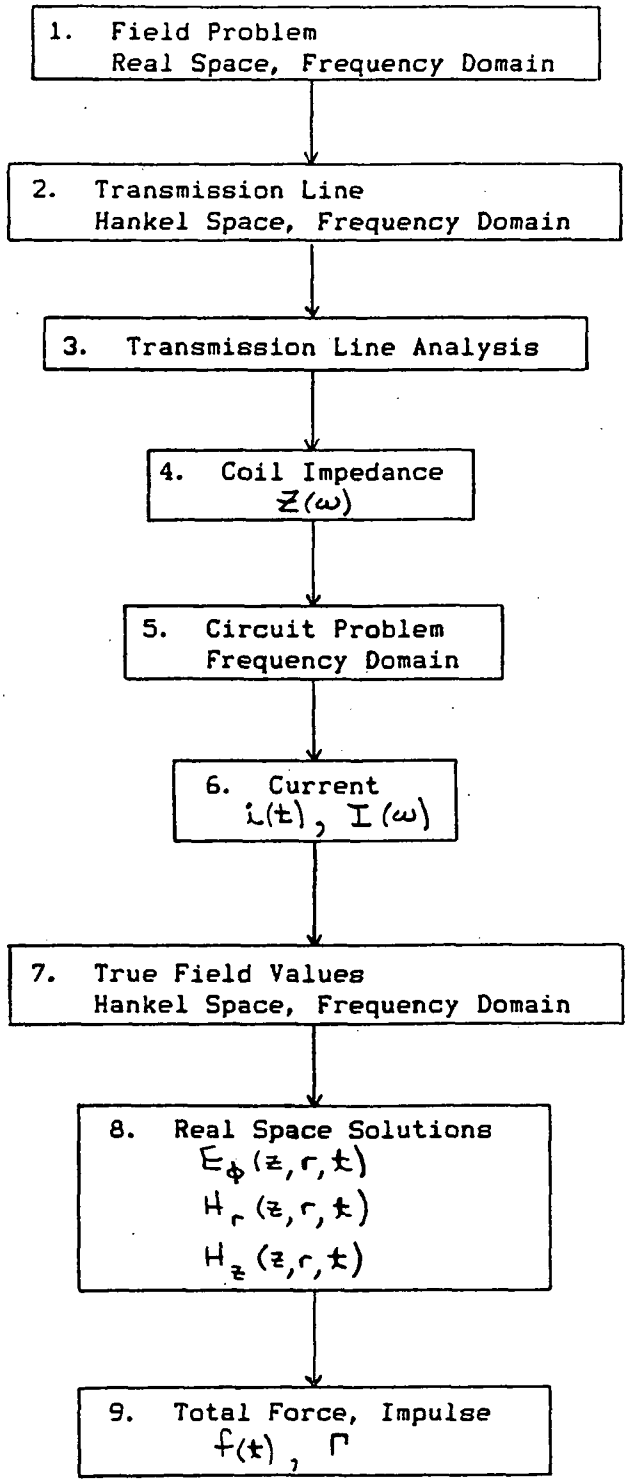

<u>FIGURE 1</u>
Analysis Flow Diagram

represents a stage in the procedure for determining the force-time profile on a rigid coil placed next to a fixed conducting plane when a capacitor is discharged through the coil.

In Block 1 of Figure 1, Maxwell's equations are written for the coil and metal target of the physical system. A simple model of the coil is proposed that stresses the geometrical symmetry of the system, eliminating several terms from the Maxwell equations. Chapter 3 discusses this modeling of the coil and metal target, and shows that application of a Hankel transform to the model equations results in a conceptual replacement of the field problem with an infinite set of transmission line problems (Block 2).

In Block 3 of Figure 1, the analysis of the transmission line model is performed. The methods of this analysis, for steady state sinusoidal conditions, may be found in Chapter 4. Chapters 3 and 4 provide the basic theoretical developments, with the results of the analyses in Chapter 4 applied in Chapter 6 to Dr. Schrag's prototype experimental EIDI system, described in Chapter 5. Modeling of the circuit used to provide energy to the coil is discussed in Chapter 2 for the specific experimental system of Chapter 5.

Once the transmission line model of the coil and target has been established in Block 3, Figure 1 shows two possible next steps in the analysis. One of these next steps, calculation of the true field values (Block 7), requires a knowledge of the coil current. Accordingly, one proceeds from the transmission line analysis in Block 3 to the Block 4 calculation of the coil impedance, required for calculating the coil current. Use of the transmission line model for calculating the part of the impedance of the coil that is due to the interaction between the coil and target is developed theoretically in Section 4.2 of Chapter 4, and applied to the impedance calculation of the coil in the prototype EIDI system in Section 6.2 of Chapter 6.

Coil impedance obtained in Block 4 is added to the calculated skin effect loss resistance in the coil, and with this total coil impedance the problem of calculating coil current, using the circuit models presented in Chapter 2, is addressed. This is Block 5, discussed in Section 6.3 of Chapter 6 for the prototype EIDI system described in Chapter 5.

Knowledge of the frequency spectrum of the coil current allows the calculation of the true field values in Hankel-Fourier space, shown in Block 7 and developed theoretically in Section 4.3 of Chapter 4. Performing an inverse Hankel transformation on these fields results in Fourier space (frequency domain) fields. An inverse discrete Fourier transform applied to the Fourier space fields provides the time domain behavior of the electric and magnetic fields, shown in Block 8. This procedure is discussed in Section 6.4 of Chapter 6 for the prototype EIDI system.

Finally, the real space axial and radial magnetic induction fields on the coil side face of the metal plate provide the necessary information for calculating the total force on the target as a function of time, as shown in Block 9. Theoretical development of the force equation is in Section 4.5 of Chapter 4, with Section 6.5 of Chapter 6 describing the numerical implementation of this force calculation for the prototype EIDI system. Calculation of the impulse delivered to the target is discussed theoretically in Section 4.6 of Chapter 4, and its application to the prototype EIDI system is described in Section 6.6 of Chapter 6.

Chapter 7 contains a summary of the results obtained, a description of the original contributions made by the author, and some suggestions for improving the procedures described in this dissertation for modeling the electrical aspects of an EIDI system.

CHAPTER TWO

THE ELECTRIC CIRCUIT MODEL

Modeling of the electronics providing power to the de-icing coil in an EIDI system is performed with the desired output from the model in mind. Since it is the coil current in conjunction with the physical configuration of the coil and wing skin that determines the magnetic fields responsible for the forces on the skin, the current in the circuit was chosen as the primary variable.

Testing of a prototype EIDI system began at The Wichita State University in 1982. The part of this system that provides power to the coil is shown in Figure 5A (page 35). This system was chosen as the basic physical configuration for which a circuit model would be derived. This circuit model is then analyzed to determine the shape of the coil current. A simple circuit model that is suggested by the physical system in Figure 5A is shown in Figure 6E (page 47). This is the basic circuit model, valid when the clamp diode across the capacitor is not conducting.

Justification for modeling the EIDI system as a lumped parameter circuit was provided by the experimental verification of the absence in the signals present of any significant frequency components having wavelengths comparable to the physical dimensions of the system. Because of the complex electromagnetic interaction between the coil and the skin next to it, it was felt that time domain modeling of the coil's terminal v-i characteristics would be too complex to be of much use. Consequently, a frequency domain approach was chosen for analyzing the circuit, making the model of the coil a linear frequency dependent impedance.

The presence of the SCR and the clamp diode across the capacitor makes the circuit model nonlinear, so that straightforward Fourier (frequency domain) techniques are not applicable. This difficulty is circumvented by performing a piecewise linear analysis of the circuit. In this analysis, the physical circuit is modeled by one of two possible circuits, depending on the state of the clamp diode. Initially, when the SCR has just been triggered, the diode is assumed off (an open circuit) and the model of Figure 6E (page 47) is used for analysis. In addition to calculating the current in this circuit, the capacitor voltage is also calculated. When this voltage first becomes negative, the clamp diode is modeled as coming into immediate forward conduction. This diode then acts as a short circuit, resulting in the circuit model shown in Figure 6F (page 51). All subsequent (in time) circuit calculations are then performed with this model.

Theoretical justification for modeling both the SCR and the clamp diode as simple on-off switches is now provided. However, the ultimate justification for such an outright dismissal of the effects of both the SCR and the clamp diode in determining the current waveform comes from observing how closely the predicted current waveform (using the models that ignore the non-ideal nature of the SCR and diode) agrees with the measured waveform. This will be shown in Chapter 6.

In a practical EIDI system, the voltage on the energy storage capacitor prior to its discharge is 1000 to 1500 volts. When the SCR is triggered into conduction, its voltage drop is on the order of 1 volt, which is small compared to the capacitor voltage, and so may be ignored in determining the circuit current. In addition to ignoring the voltage drop across the SCR, the dynamics of the SCR are also not modeled. Such dynamics are, in the EIDI circuit, primarily manifested in the failure of the SCR to trigger into instantaneous full forward conduction upon initiation of a forward gate current. However, modern SCR design techniques [5], [6], [7] have resulted in turn-on times that are short compared to the time required for a significant change in the coil current in the experimental EIDI prototype system. The SCR used in the prototype system had a di/dt rating of 800 amps/ microsecond, while the maximum observed rate of change in the circuit was 15 amps/microsecond.

A similar consideration of the voltage levels in the circuit results in the conclusion that the approximately 1 volt forward drop across the clamp diode is not a primary factor in determining circuit current. When the diode is off, its transition capacitance is insignificant compared to the capacitance of the energy storage capacitor. Reverse leakage current in the diode is ignored due to the large energy storage capacitor in parallel with the diode and the relatively small time in which the electrical events of interest take place in the circuit. With the diode in forward conduction, the sum of its transition and diffusion capacitances are small enough that, to a first approximation, they may be ignored in the circuit model.

In constructing the EIDI prototype experimental configuration, care was exercised to minimize parasitics in the circuit. Special low inductance and resistance cable was used to connect the energy storage capacitor to the coil. However, both of these cable parameters were measured in the prototype system and are taken into account in the circuit model. The energy storage capacitor, which was physically several units in parallel, used copper strap for wiring connections to minimize inductance and resistance parasitics. The ESR (equivalent series resistance) and ESL (equivalent series inductance) of the capacitors were felt to be small, and are not modeled. If, in a particular EIDI installation, these parasitics are not small, they can be taken into account by adding lumped elements in series with the energy storage capacitor in the circuit model.

Accurate frequency domain modeling of the coil is the most difficult feat in constructing the circuit model, and is discussed in Chapter 4.

CHAPTER THREE

TRANSMISSION LINE MODEL OF THE FIELD PROBLEM

3.1 INTRODUCTION

The transmission line model of the coil and metal plate is the heart of the prototype EIDI system model. It is this model that is expected to account for the complex electromagnetic interactions between the coil and plate. These interactions help establish the impedance presented at the coil terminals, and so are a factor in determining the coil current. This current is important in determining the force on the plate.

3.2 GEOMETRY OF A PROTOTYPE EIDI SYSTEM

Figure 3A shows the profile of the physical coil-metal plate con-

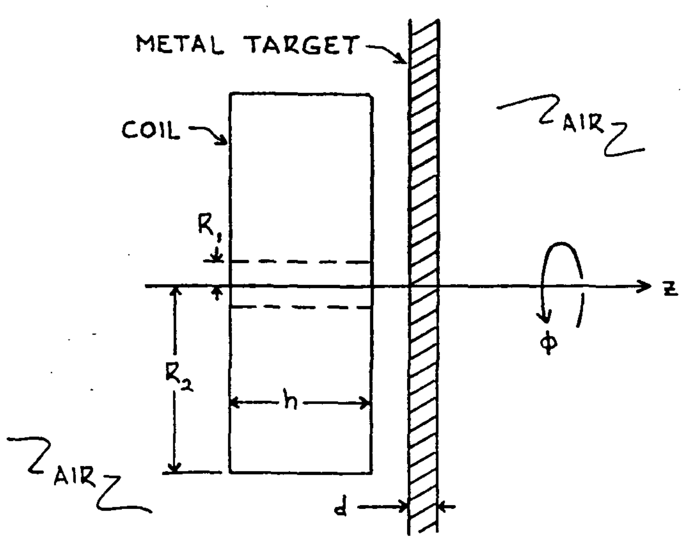

FIGURE 3A
COIL-TARGET GEOMETRY

figuration we have chosen to model. The coil has the shape of a short ($h \ll R_2$) thick walled ($R_1 \ll R_2$) hollow cylinder with an inside radius R_1 and an outside radius R_2, whose axis is perpendicular to a flat metal plate (henceforth called the "target") of thickness d extending to infinity in all radial directions. An air gap exists between the coil and target, both of which are assumed rigid and stationary in space.

Most of the coils used in EIDI applications have been round, at least prior to a possible bending of the coil to conform to the curved leading edge of a wing. The flat geometry of Figure 3A is a reasonable model of such a coil, provided that the radius of curvature of the coil, after being shaped to conform to the wing, is much greater than the coil outer radius R_2.

The assumption that the coil and target remain separated by a fixed distance would be reasonable if the initial separation distance was much larger than the maximum change in separation distance obtained when the capacitor is discharged through the coil. Such an inequality in separation distances may not hold in a practical EIDI installation. Alternatively, the fixed separation distance assumption would be justified if the force "impulse" delivered to the plate by the coil was so short that the plate acquired only a small velocity, with negligible displacement, for the duration of the "impulse". This does not generally happen in a practical EIDI system. In fact, a well designed installation has the target move from zero to maximum displacement within the duration of the "impulse". With ice loading present, however, the displacement may be small compared to the initial separation distance.

3.3 THE FIELD EQUATIONS

The approach that appears to be the most fruitful for modeling the coil and target in our prototype EIDI system is presented in a paper by El-Markabi and Freeman [4]. We now describe their approach, emphasizing those aspects of the theory that are most appropriate to the analysis of the model of the prototype system of Figure 3A. The reader is referred to El-Markabi and Freeman [4] for the more general theory.

Current in the coil of Figure 3A is assumed to be entirely phi directed. A slight modeling error is introduced by this assumption, since a radial component of current actually exists in a practical coil due to the spiral winding of the coil. By neglecting this small radial current, a model having azimuthal symmetry is obtained. Consequently, the model shows no phi dependence in any of its field quantities, the electric field contains only a phi component, and the magnetic field contains only axial and radial components.

Because most of the spectral energy of the current in a practical EIDI coil is confined to relatively low frequencies, a quasi-static situation is assumed. The displacement current term in Ampere's Law is ignored.

With these assumptions, Maxwell's equations written for Figure 3A become

$$\frac{\partial E_\phi(z,r,t)}{\partial z} = \mu \frac{\partial H_r(z,r,t)}{\partial t}$$

$$\frac{1}{r}\frac{\partial}{\partial r}\left[r E_\phi(z,r,t)\right] = -\mu \frac{\partial H_z(z,r,t)}{\partial t}$$

$$\frac{\partial H_r(z,r,t)}{\partial z} - \frac{\partial H_z(z,r,t)}{\partial r} = \sigma E_\phi(z,r,t)$$

Partial differentiation with respect to time can be eliminated from these equations by taking the Fourier transform. Differentiation with respect to time is then replaced with multiplication by the $j\omega$ operator. Performing this transformation, we obtain the following equations (note that we have not introduced new symbols for the transformed field quantities, but have instead simply replaced their time variable argument t with the Fourier transform variable omega)

$$\frac{\partial E_\phi(z,r,\omega)}{\partial z} = j\omega\mu H_r(z,r,\omega) \tag{1}$$

$$\frac{1}{r}\frac{\partial}{\partial r}\left[r E_\phi(z,r,\omega)\right] = -j\omega\mu H_z(z,r,\omega) \tag{2}$$

$$\frac{\partial H_r(z,r,\omega)}{\partial z} - \frac{\partial H_z(z,r,\omega)}{\partial r} = \sigma E_\phi(z,r,\omega) \tag{3}$$

Equation (1) contains only the phi component of E and the radial component of H. By combining equations (2) and (3) in such a fashion as to eliminate the axial component of H, we would have another equation containing only the phi component of E and the radial component of H. This elimination yields

$$\frac{\partial H_r}{\partial z} = \sigma E_\phi + \frac{\partial H_z}{\partial r} = \sigma E_\phi + \frac{\partial}{\partial r}\left[\frac{-1}{j\omega\mu}\frac{1}{r}\frac{\partial}{\partial r}(r E_\phi)\right]$$

$$\frac{\partial H_r}{\partial z} = \sigma E_\phi - \frac{1}{j\omega\mu}\frac{\partial}{\partial r}\left[\frac{1}{r}\frac{\partial}{\partial r}(r E_\phi)\right] \tag{4}$$

At this point, we introduce a mathematical tool that is of considerable use here. This tool is the Hankel transform of order n, defined by [12]

$$\mathcal{H}\{f(r)\} \triangleq \int_0^\infty f(r)\, r\, J_n(\lambda r)\, dr = F(\lambda)$$

with the inverse transform

$$\mathcal{H}^{-1}\{F(\lambda)\} = \int_0^\infty F(\lambda)\, \lambda\, J_n(\lambda r)\, d\lambda = f(r)$$

Although the introduction of an additional transform introduces difficulties of its own, it provides an even greater amount of simplification, and makes possible the transmission line model of the coil-target electromagnetic field problem.

If a Hankel transform of order 1 is applied with respect to the variable r in equation (4), the following result is obtained [11], [12] (note that we have again not introduced new symbols for the transformed quantities, simply replacing their spatial variable argument r with the Hankel transform variable lambda)

$$\frac{\partial H_r(z,\lambda,\omega)}{\partial z} = \left(\sigma + \frac{\lambda^2}{j\omega\mu}\right) E_\phi(z,\lambda,\omega) \qquad (5)$$

The advantage of equation (5) over equation (4) is that equation (5) contains partial derivatives with respect to only the z coordinate, in effect becoming an ordinary differential equation (if one allows "constants of integration" for such an equation to be arbitrary functions of all variables except z). If the same Hankel transform is applied to equation (1), we obtain

$$\frac{\partial E_\phi(z,\lambda,\omega)}{\partial z} = j\omega\mu H_r(z,\lambda,\omega) \qquad (6)$$

Equations (5) and (6) are two coupled ordinary differential equations that are recognizable as the canonical transmission line equations. The solutions of these equations are well known [13], [14], [15].

3.4 DEVELOPMENT OF THE TRANSMISSION LINE MODEL

Because equations (5) and (6) are identical in form to the equations describing voltage and current on an ordinary transmission line, we now introduce the symbols $\hat{V}$ and $\hat{I}$ (each of which is a function of position z along the coil axis, the Fourier variable omega, and the Hankel variable lambda) to represent the phi component of E and the radial component of H respectively. Then equations (5) and (6) become

$$\frac{\partial \hat{I}}{\partial z} = \left(\sigma + \frac{\lambda^2}{j\omega\mu}\right) \hat{V} \tag{7}$$

$$\frac{\partial \hat{V}}{\partial z} = j\omega\mu \hat{I} \tag{8}$$

Differentiating equation (7) with respect to z, we have

$$\frac{\partial^2 \hat{I}}{\partial z^2} = \left(\sigma + \frac{\lambda^2}{j\omega\mu}\right) \frac{\partial \hat{V}}{\partial z}$$

Substitution of equation (8) into this last equation yields

$$\frac{\partial^2 \hat{I}}{\partial z^2} = j\omega\mu \left(\sigma + \frac{\lambda^2}{j\omega\mu}\right) \hat{I}$$

$$\frac{\partial^2 \hat{I}}{\partial z^2} = \left(\lambda^2 + j\omega\mu\sigma\right) \hat{I} \tag{9}$$

Similarly, we differentiate equation (8) to obtain

$$\frac{\partial^2 \hat{V}}{\partial z^2} = j\omega\mu \frac{\partial \hat{I}}{\partial z}$$

Substitution of equation (7) into this equation yields

$$\frac{\partial^2 \hat{V}}{\partial z^2} = j\omega\mu \left(\sigma + \frac{\lambda^2}{j\omega\mu}\right) \hat{V}$$

$$\frac{\partial^2 \hat{V}}{\partial z^2} = \left(\lambda^2 + j\omega\mu\sigma\right) \hat{V} \tag{10}$$

Now define the complex propagation constant gamma in Fourier-Hankel space as

$$\gamma = \sqrt{\lambda^2 + j\omega\mu\sigma}$$

so that the general solutions to equations (9) and (10), assuming complex sinusoidal time variation of $\hat{V}$ and $\hat{I}$, may be written as

$$\hat{I} = \hat{I}_{0+} e^{-\gamma z} + \hat{I}_{0-} e^{\gamma z} \tag{11}$$

$$\hat{V} = \hat{V}_{o+} e^{-\gamma z} + \hat{V}_{o-} e^{\gamma z} \qquad (12)$$

where $\hat{I}_{o+}$, $\hat{I}_{o-}$ and $\hat{V}_{o+}$, $\hat{V}_{o-}$ are complex phasor functions of the Hankel variable lambda (we have suppressed the complex sinusoidal time variation $e^{j\omega t}$ in these solutions).

Note that we are conceptually dealing with an uncountably infinite set of transmission lines. Each transmission line is associated with a different value of lambda, where lambda is non-negative. The physical origin of this infinite number of transmission lines lies in our "compressing" the infinite radial variation in the real space field quantities H_r and E_ϕ at a given axial coordinate z into variables V and I localized to a single "point" (the corresponding z coordinate) on a Hankel space transmission line. It then takes an infinite number of transmission lines to account for the infinite number of possible values of the radius in the real space problem.

To derive an expression for the characteristic impedance of one of these Hankel space transmission lines, consider the case of a line having only a single frequency complex sinusoid traveling in the direction of increasing z. In agreement with ordinary transmission line theory, the negative sign in the exponents in equations (11) and (12) denotes propagation in the direction of increasing z. Then equations (11) and (12) become

$$\hat{I} = \hat{I}_{o+} e^{-\gamma z} \qquad (13)$$

$$\hat{V} = \hat{V}_{o+} e^{-\gamma z} \qquad (14)$$

Substitute the expressions for the current and voltage from equations (13) and (14) into equation (7)

$$-I_{o+}\gamma e^{-\gamma z} = \left(\sigma + \frac{\lambda^2}{j\omega\mu}\right) V_{o+} e^{-\gamma z}$$

From this equation, we obtain the defining expression for the characteristic impedance of a Hankel space transmission line as

$$Z_o \triangleq \frac{V_{o+}}{I_{o+}} = -\gamma \Big/ \left(\sigma + \frac{\lambda^2}{j\omega\mu}\right)$$

$$Z_o = \frac{-j\omega\mu}{\sqrt{\lambda^2 + j\omega\mu\sigma}}$$

This result differs by a negative sign from the expression given in El-Markabi and Freeman [4] for the line's characteristic impedance. One could argue that the negative branch of the square root function in the expression for the propagation coefficient gamma should be chosen, which would eliminate the negative sign in the characteristic impedance. However, calculations performed with a negative characteristic impedance results in predictions that are essentially in agreement with experimental measurements, whereas the use of a positive characteristic impedance predicts results that are not in agreement with experiment. Alternatively, one could propose that it is the positive sign that must be chosen for the exponents in equations (11) and (12) to correspond to propagation in the direction of increasing z. Such an assumption also results in predictions that are not in agreement with experiment.

Transformation of real space current sources into Hankel space is discussed in El-Markabi and Freeman [4]. They show that a disc of azimuthally directed uniform surface current of phasor value $\tilde{I}$, with an inner radius R_1 and an outer radius R_2, located on the z-axis, becomes a sinusoidal current source with phasor value

$$\frac{\tilde{I}}{R_2 - R_1} \int_{R_1}^{R_2} r\, J_1(\lambda r)\, dr$$

connected in parallel with the Hankel space transmission line. The z coordinate of this current source is the same as the z coordinate of the real space surface current from which it arose.

We have chosen three of these ideal azimuthally directed discs of uniform surface current to model the current distribution in the coil. The inner (outer) radius of the disc is equal to the inner (outer) radius of the coil. The middle disc is located at the axial center of the coil, while the two outer discs are each spaced out a distance of one-third of the coil's width from the center of the coil. See Figure 3B. Clearly, some error occurs here due to the localization of the model's current to these discs.

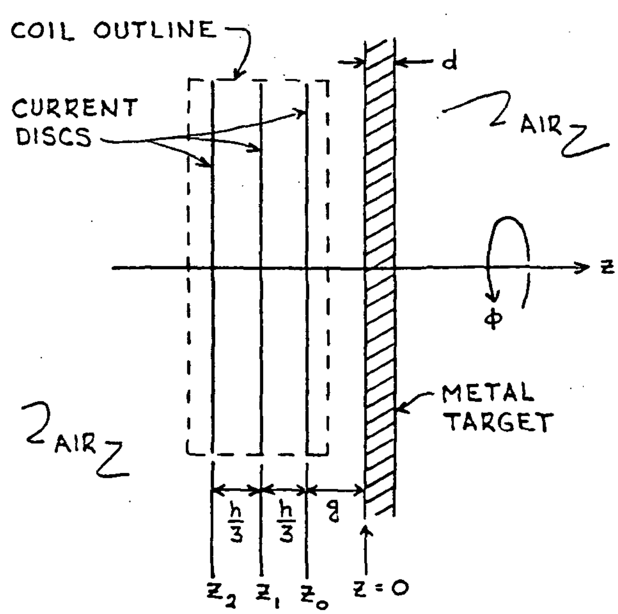

FIGURE 3B
CURRENT DISC MODEL OF COIL

Figure 3C shows the Hankel space transmission line configuration corresponding to the three current sheet model of the coil next to the target. All of our Hankel space calculations are based upon this model.

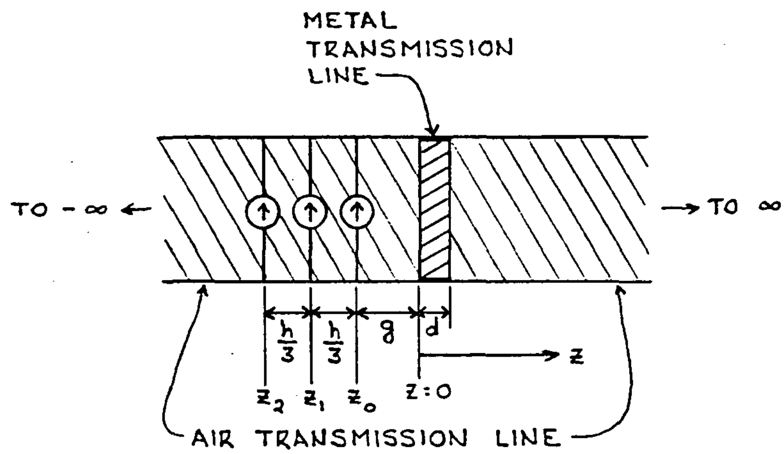

FIGURE 3C
HANKEL SPACE TRANSMISSION LINE MODEL
OF COIL AND TARGET

CHAPTER FOUR

ANALYSIS STRUCTURE

4.1 INTRODUCTION

In this chapter, the transmission line model of the coil and target developed in Chapter 3 and shown in Figure 3C is examined mathematically using conventional transmission line theory to predict the Fourier-Hankel space behavior of the model when it is in the sinusoidal steady state condition. The analyses performed in this chapter will assume each of the three current sources in Figure 3C has unit phasor value. In view of the analogy developed in Chapter 3, we will freely use the terms current and voltage in connection with the transmission line model to stand for the Fourier-Hankel transforms of the radial magnetic induction $B_r(z,r,t)$ and the azimuthal electric intensity $E_\phi(z,r,t)$ respectively. Throughout this chapter, reference should be made to Figure 3C for insight into the equations written and for identification of the variables used.

4.2 METHOD OF CALCULATING COIL IMPEDANCE

Although the part of the coil impedance that is independent of the properties of the ribbon conductor used to wind the coil is calculated in Hankel space, as shown in this section, one must begin the derivation of the expresion for the impedance in Fourier space. Only in the frequency domain does the concept of impedance make sense. We will calculate the coil impedance at a frequency omega by exciting the coil with a current source of phasor value 1, and finding the phasor voltage response at the coil terminals. The coil impedance is then numerically equal to this voltage response.

Our real (Fourier) space model of the coil is three ideal discs of azimuthally directed uniform surface current. We need to relate the electric fields induced in the different parts of this model to the single voltage that exists between the coil terminals. We approximate the voltage appearing at the coil terminals by the average of the voltages induced at the locations of the three discs of the model. Symbolically, we have

$$Z = \frac{\tilde{V}}{\tilde{I}} = \frac{\tilde{V}}{1} = \tilde{V} = \frac{1}{3}\left(\tilde{V}_0 + \tilde{V}_1 + \tilde{V}_2\right)$$

where $\tilde{V}_k$ represents the voltage induced at the location of the disc with axial coordinate z_k.

Because of the symmetry of our model, the voltage induced on a circular path (centered on the z axis) of radius r and axial coordinate z_k will be given by

$$2\pi r\, E_\phi(z_k, r, \omega)$$

The average voltage induced on the infinite number of circular paths between $r=R_1$ and $r=R_2$ is

$$\frac{1}{R_2 - R_1} \int_{R_1}^{R_2} 2\pi r\, E_\phi(z_k, r, \omega)\, dr$$

Multiplication of this expression by N, the number of turns in the actual coil, yields

$$\tilde{V}_k = \frac{2\pi N}{R_2 - R_1} \int_{R_1}^{R_2} r\, E_\phi(z_k, r, \omega)\, dr$$

which is the model-predicted voltage induced on an infinitesimally thin N turn coil having an inner radius R_1 and an outer radius R_2 located at z_k. Averaging these induced voltages over the three discs results in the phasor coil voltage

$$\tilde{V} = \frac{1}{3}\left\{ \frac{2\pi N}{R_2 - R_1} \int_{R_1}^{R_2} r \sum_{i=0}^{2} E_\phi(z_i, r, \omega)\, dr \right\} \tag{1}$$

$$\tilde{V} = Z$$

Because this expression is numerically equal to the coil impedance, we will replace the symbol $\tilde{V}$ by Z in further appearances of this expression.

The E fields that appear in (1) are frequency domain (Fourier space) E fields. In terms of the Fourier-Hankel space E fields, we can write these Fourier space E fields as

$$E_\phi(z_k, r, \omega) = \int_0^\infty E_\phi(z_k, \lambda, \omega)\, \lambda\, J_1(\lambda r)\, d\lambda \tag{2}$$

where we have again used the list of arguments to distinguish between different functions. Specifically, $E_\phi(z_k, r, \omega)$ is the Fourier transform of the real space azimuthal electric intensity $E_\phi(z_k, r, t)$, and $E_\phi(z_k, \lambda, \omega)$ is the Fourier-Hankel transform of the real space azimuthal electric intensity $E_\phi(z_k, r, t)$. Substituting (2) into (1) yields

$$Z = \frac{1}{3}\frac{2\pi N}{R_2 - R_1} \int_{R_1}^{R_2} \left[\sum_{i=0}^{2} \int_0^\infty E_\phi(z_i, \lambda, \omega)\, \lambda\, J_1(\lambda r)\, d\lambda \right] r\, dr$$

Interchanging the order of integration,

$$Z = 2\pi \int_0^\infty \left[\frac{N}{3(R_2 - R_1)} \int_{R_1}^{R_2} J_1(\lambda r)\, r\, dr \right] \sum_{i=0}^{2} E_\phi(z_i, \lambda, \omega)\, \lambda\, d\lambda$$

$$Z = 2\pi \int_0^\infty K'(\lambda) \sum_{i=0}^{2} E_\phi(z_i, \lambda, \omega)\, \lambda\, d\lambda \tag{3}$$

where
$$K'(\lambda) = \frac{N}{3(R_2 - R_1)} \int_{R_1}^{R_2} J_1(\lambda r)\, r\, dr$$

is the Hankel transformed current corresponding to an infinitesimally thin N turn coil of inner radius R_1 and outer radius R_2, carrying a phasor current of strength 1/3.

Expression (3) contains three Fourier-Hankel space electric fields (transmission line voltages) that conceptually arose from Fourier space phasor currents of value 1/3 on each of the three discs in Figure 3B. The "scaling factor" that relates Fourier-Hankel space fields due to unity Fourier space phasor coil current to Fourier-Hankel space voltages and currents due to unity phasor current in each of the three current sources in Figure 3C is $K'(\lambda)$. Then in terms of the Fourier-Hankel space voltage $E'_\phi(z_i, \lambda, \omega)$ due to unity phasor current in each of the Figure 3C current sources, (3) becomes

$$Z = 2\pi \int_0^\infty \left[K'(\lambda)\right]^2 \sum_{i=0}^{2} E'_\phi(z_i, \lambda, \omega)\, \lambda\, d\lambda \qquad (4)$$

Expression (4) is the result that we use to calculate the terminal impedance of the coil.

4.3 RADIAL MAGNETIC INDUCTION AND AZIMUTHAL ELECTRIC INTENSITY

4.3.1 Target Surface Facing Coil

We begin by calculating the characteristic impedance and the complex propagation constant of the air transmission line and the metal transmission line, referred to hereafter as the air line and the metal line respectively, using the results derived in Chapter 3. For the air line, the conductivity σ is equal to zero, and so

$$Z_a = -j\omega\mu / \sqrt{\lambda^2 + j\omega\mu\sigma} = -j\omega\mu/\lambda$$

$$\gamma_a = \sqrt{\lambda^2 + j\omega\mu\sigma} = \lambda$$

For the metal line, no simplification is possible and we have

$$Z_m = \frac{-j\omega\mu}{\sqrt{\lambda^2 + j\omega\mu\sigma}}$$

$$\gamma_m = \sqrt{\lambda^2 + j\omega\mu\sigma}$$

According to the analogy developed in Chapter 3, calculation of the total current and voltage at z=0 in Figure 3C is equivalent to calculation of the radial magnetic induction B_r and the azimuthal electric intensity E_ϕ on the coil side face of the target. We perform this current and voltage calculation by replacing the transmission line configuration for all z>0 with its equivalent impedance. Note that both sides of the metal line are connected to infinite lengths of air transmission line with characteristic impedance Z_a. The equivalent impedance looking to the right at z=0 in Figure 3C is

$$Z(0) = Z_m \frac{Z_a + Z_m \tanh(\gamma_m d)}{Z_m + Z_a \tanh(\gamma_m d)} \qquad (5)$$

Using this equivalent impedance, the current reflection coefficient at z=0 as seen from the air line is

$$\rho_H = \frac{Z_a - Z(0)}{Z_a + Z(0)}$$

and the total current at z=0 is then

$$\hat{I}_{total} = \hat{I}_{inc} + \hat{I}_{reflected} = (1 + \rho_H)\hat{I}_{inc} \qquad (6)$$

in terms of the incident current $\hat{I}_{inc}$, which must be due solely to the three current sources. Expression (6) may be simplified as follows.

$$\hat{I}_{total} = \left(1 + \frac{Z_a - Z(0)}{Z_a + Z(0)}\right)\hat{I}_{inc} = \frac{2Z_a}{Z_a + Z(0)}\hat{I}_{inc} \qquad (7)$$

Substituting (5) into (7) yields

$$\hat{I}_{total} = 2\hat{I}_{inc}\frac{Z_a}{Z_a + Z_m\dfrac{Z_a + Z_m\tanh(\gamma_m d)}{Z_m + Z_a\tanh(\gamma_m d)}}$$

which, upon replacing Z_a and Z_m by their defining expressions gives

$$\hat{I}_{total} = 2\hat{I}_{inc}\frac{1}{1 + \dfrac{\lambda}{\sqrt{\lambda^2 + j\omega\mu\sigma}}\,\dfrac{1 + \dfrac{\lambda^2}{\sqrt{\lambda^2 + j\omega\mu\sigma}}\tanh(\gamma_m d)}{\dfrac{\lambda}{\sqrt{\lambda^2 + j\omega\mu\sigma}} + \tanh(\gamma_m d)}} \qquad (8)$$

Now consider the current source in Figure 3C closest to the target. This source produces an incident current on the metal line at z=0 given by

$$\hat{I}_{inco} = \frac{1}{2}e^{-\gamma_a g} = \frac{e^{-\lambda g}}{2}$$

where the factor 1/2 comes from the equal division of the unity phasor amplitude current to both sides of the air line containing the current source. Total current incident at z=0 is by superposition given by

$$\hat{I}_{inc} = \frac{1}{2}e^{-\lambda g} + \frac{1}{2}e^{-\lambda(g+h/3)} + \frac{1}{2}e^{-\lambda(g+2h/3)}$$

$$\hat{I}_{inc} = \frac{1}{2}e^{-\lambda g}\left(1 + e^{-\lambda h/3} + e^{-2\lambda h/3}\right) \qquad (9)$$

Substituting (9) into (8) yields

$$\hat{I}_{total} = \frac{e^{-\lambda g}\left(1 + e^{-\lambda h/3} + e^{-2\lambda h/3}\right)}{1 + \frac{\lambda}{\sqrt{\lambda^2 + j\omega\mu\sigma}} \dfrac{1 + \frac{\lambda}{\sqrt{\lambda^2+j\omega\mu\sigma}} \tanh(\gamma_m d)}{\frac{\lambda}{\sqrt{\lambda^2+j\omega\mu\sigma}} + \tanh(\gamma_m d)}} \tag{10}$$

for the total steady state current $\hat{I}_{total}$ at z=0 due to unit strength complex sinusoidal excitation in each of the three current sources. Multiplying (10) by $K'(\lambda)I(\omega)$, where $I(\omega)$ is the Fourier transform of the current in the coil (and multiplication by $K'(\lambda)$ transforms a unity Fourier space current into the corresponding Fourier-Hankel space current), yields the desired result

$$\hat{I}(z=0) = \frac{I(\omega)\, K'(\lambda)\, e^{-\lambda g}\left(1 + e^{-\lambda h/3} + e^{-2\lambda h/3}\right)}{1 + \frac{\lambda}{\sqrt{\lambda^2 + j\omega\mu\sigma}} \dfrac{1 + \frac{\lambda}{\sqrt{\lambda^2+j\omega\mu\sigma}} \tanh(\gamma_m d)}{\frac{\lambda}{\sqrt{\lambda^2+j\omega\mu\sigma}} + \tanh(\gamma_m d)}} \tag{11}$$

for the Fourier-Hankel transform of the radial magnetic induction B_r on the coil side face of the metal target when the coil current spectrum is $I(\omega)$.

Calculation of the voltage is almost identical to the calculation of the current performed above. The voltage reflection coefficient is the negative of the current reflection coefficient,

$$\rho_E = \frac{Z(0) - Z_a}{Z(0) + Z_a}$$

Total voltage at z=0 is

$$\hat{V}_{total} = \hat{V}_{inc} + \hat{V}_{reflected} = (1+\rho_E)\hat{V}_{inc}$$

in terms of the incident voltage $\hat{V}_{inc}$. Expression (12) may be simplified as

$$\hat{V}_{total} = \left(1 + \frac{Z(0) - Z_a}{Z(0) + Z_a}\right)\hat{V}_{inc} = \frac{2Z(0)}{Z_a + Z(0)}\hat{V}_{inc} \qquad (13)$$

Substituting (5) into (13),

$$\hat{V}_{total} = 2\hat{V}_{inc} \frac{Z_m \dfrac{Z_a + Z_m \tanh(\gamma_m d)}{Z_m + Z_a \tanh(\gamma_m d)}}{Z_a + Z_m \dfrac{Z_a + Z_m \tanh(\gamma_m d)}{Z_m + Z_a \tanh(\gamma_m d)}}$$

which, upon replacing Z_a and Z_m by their defining expressions, gives

$$\hat{V}_{total} = \frac{2\hat{V}_{inc}}{1 + \dfrac{\sqrt{\lambda^2 + j\omega\mu\sigma}}{\lambda} \dfrac{\dfrac{\lambda}{\sqrt{\lambda^2 + j\omega\mu\sigma}} + \tanh(\gamma_m d)}{1 + \dfrac{\lambda}{\sqrt{\lambda^2 + j\omega\mu\sigma}}\tanh(\gamma_m d)}} \qquad (14)$$

Total incident voltage V_{inc} at z=0 is given by

$$\hat{V}_{inc} = Z_a \hat{I}_{inc} = \frac{j\omega\mu}{\lambda}\frac{1}{2}e^{-\lambda g}\left(1 + e^{-\lambda h/3} + e^{-2\lambda h/3}\right)$$

using (9) for $\hat{I}_{inc}$. Substituting this expression for $\hat{V}_{inc}$ into (14) yields

$$\hat{V}_{total} = \frac{\dfrac{j\omega\mu}{\lambda} e^{-\lambda g}\left(1 + e^{-\lambda h/3} + e^{-2\lambda h/3}\right)}{1 + \dfrac{\sqrt{\lambda^2 + j\omega\mu\sigma}}{\lambda} \dfrac{\dfrac{\lambda}{\sqrt{\lambda^2 + j\omega\mu\sigma}} + \tanh(\gamma_m d)}{1 + \dfrac{\lambda}{\sqrt{\lambda^2 + j\omega\mu\sigma}}\tanh(\gamma_m d)}} \qquad (15)$$

for the total voltage at z=0 due to unit strength complex sinusoidal excitation in each of the three current sources. Multiplying (15) by $K'(\lambda)I(\omega)$ yields the desired result

$$\hat{V}(z=0) = \frac{I(\omega)\,K'(\lambda)\,\frac{j\omega\mu}{\lambda}\,e^{-\lambda g}\left(1+e^{-\lambda h/3}+e^{-2\lambda h/3}\right)}{1+\frac{\sqrt{\lambda^2+j\omega\mu\sigma}}{\lambda}\;\frac{\frac{\lambda}{\sqrt{\lambda^2+j\omega\mu\sigma}}+\tanh(\gamma_m d)}{1+\frac{\lambda}{\sqrt{\lambda^2+j\omega\mu\sigma}}\tanh(\gamma_m d)}} \tag{16}$$

for the Fourier-Hankel transform of the azimuthal electric intensity E_ϕ on the coil side face of the target when the coil current spectrum is $I(\omega)$.

4.3.2 Target Surface Opposite Coil

Knowing the total voltage and current at z=0 (derived in Section 4.3.1 and given by (16) and (11) respectively) allows a simple transmission line inverse chain matrix calculation of the total voltage and current at z=d, which are the Fourier-Hankel transforms of the azimuthal electric intensity E_ϕ and the radial magnetic induction B_r on the surface of the metal target opposite the coil. Denoting these transforms of the fields on the coil side face of the target by $\hat{V}_n$ (given by (16) above) and $\hat{I}_n$ (given by (11) above), we have

$$\hat{V}_f = \hat{V}_n \cosh(\gamma_m d) - Z_m \hat{I}_n \sinh(\gamma_m d) \tag{17}$$

$$\hat{I}_f = -\hat{V}_n \frac{\sinh(\gamma_m d)}{Z_m} + \hat{I}_n \cosh(\gamma_m d) \tag{18}$$

where $\hat{V}_f$ and $\hat{I}_f$ denote total voltage (electric intensity) and current (magnetic induction) on the surface of the target opposite the coil.

4.4 CALCULATION OF THE AXIAL MAGNETIC FIELD USING THE TRANSMISSION LINE MODEL

The procedure that we use for calculating the force on the target is described in the next section, and requires both the radial and the axial components of the magnetic induction on the target surface next to the coil. The radial component of the magnetic intensity is available from the transmission line model by performing inverse Hankel and Fourier transformations on the calculated transmission line current at z=0, as discussed in Section 4.3.1. By using equation (2) in Chapter 3, it is also possible to calculate the axial component of the magnetic intensity (which does not have a transmission line analog) from the transmission line voltage, as shown below.

The azimuthal electric field is given in Fourier space by

$$E_\phi(z,r,\omega) = \mathcal{H}^{-1}\left\{V(z,\lambda,\omega)\right\} = \int_0^\infty V(z,\lambda,\omega)\,\lambda\,J_1(\lambda r)\,d\lambda \qquad (19)$$

Substituting (19) into equation (2) from Chapter 3, we have

$$H_z(z,r,\omega) = \frac{-1}{j\omega\mu}\,\frac{1}{r}\,\frac{\partial}{\partial r}\left\{r\,E_\phi(z,r,\omega)\right\}$$

$$H_z(z,r,\omega) = \frac{-1}{j\omega\mu r}\,\frac{\partial}{\partial r}\left\{r\int_0^\infty V(z,\lambda,\omega)\,\lambda\,J_1(\lambda r)\,d\lambda\right\} \qquad (20)$$

Interchanging the order of partial differentiation and integration in (20),

$$H_z(z,r,\omega) = \frac{-1}{j\omega\mu r}\int_0^\infty \frac{\partial}{\partial r}\left\{\lambda r\,J_1(\lambda r)\right\} V(z,\lambda,\omega)\,d\lambda \qquad (21)$$

Using the identity

$$\frac{d}{dx}\left\{x\,J_1(x)\right\} = x\,J_0(x)$$

(21) becomes

$$H_z(z,r,\omega) = \frac{-1}{j\omega\mu} \int_0^\infty V(z,\lambda,\omega)\, \lambda^2 J_0(\lambda r)\, d\lambda \qquad (22)$$

Equation (22) states that the axial component of the magnetic intensity H_z in Fourier space is given by the zero order inverse Hankel transform of the transmission line voltage at the corresponding z coordinate multiplied by lambda, with the result divided by $j\omega\mu$. Inverse Fourier transformation of the right hand side of (22) yields the desired time domain axial magnetic intensity.

4.5 FORCE BETWEEN TARGET AND COIL

Our procedure for calculating the total force between the target and the coil utilizes the Maxwell stress tensor, and is performed in real space (using the time domain fields). Stratton [41] shows that the total force F transmitted by a time varying electromagnetic field across a closed surface S is given by

$$\bar{F} = \oint_S \left[\varepsilon(\bar{E}\cdot\hat{n})\bar{E} + \frac{1}{\mu}(\bar{B}\cdot\hat{n})\bar{B} - \frac{1}{2}\left(\varepsilon E^2 + \frac{B^2}{\mu}\right)\hat{n} \right] da$$

where $\hat{n}$ is a unit vector normal to the surface. We take as our closed surface the plane z=0 (the coil side face of the target, "closed" at infinity). Since $\hat{n}=\hat{z}$, this integral reduces to

$$\bar{F} = \int_{r=0}^{\infty} \int_{\phi=0}^{2\pi} \left[\frac{B_z}{\mu}(B_z\hat{z} + B_r\hat{r}) - \frac{1}{2}\left(\varepsilon E_\phi^2 + \frac{B_z^2+B_r^2}{\mu}\right)\hat{z} \right] r\, d\phi\, dr$$

The total force tending to separate coil and target is just the z component of this force,

$$F_z = 2\pi \int_{r=0}^{\infty} \left(\frac{B_z^2}{2\mu} - \frac{\varepsilon E_\phi^2}{2} - \frac{B_r^2}{2\mu} \right) r\, dr$$

$$F_z = \frac{\pi}{\mu}\int_0^\infty (B_z^2 - B_r^2)\, r\, dr - \pi\varepsilon\int_0^\infty E_\phi^2\, r\, dr \qquad (23)$$

Our calculations of the fields E_ϕ, B_r, and B_z in the prototype experimental EIDI configuration described in Chapter 5 showed that the second integral in (23) is totally insignificant compared to the first integral. Some feeling for why this is true can be obtained by comparing the constants that multiply each of the integrals in (23).

$$\frac{\pi}{\mu} = \frac{\pi}{4\pi\times10^{-7}} = 2.5\times10^{6}$$

$$\pi\varepsilon \doteq \frac{\pi\, 10^{-9}}{36\pi} \doteq 2.8\times10^{-11}$$

Accordingly, we approximate (23) by

$$F_z(t) = \frac{\pi}{\mu}\int_0^\infty \left[B_z^2(t) - B_r^2(t)\right] dr \qquad (24)$$

Equation (24) is the result that we use to calculate force versus time.

4.6 IMPULSE DELIVERED TO TARGET

The impulse delivered to the stationary target is by definition given by the integral

$$\Gamma = \int_0^\infty F_z(t)\, dt \qquad (25)$$

where $F_z(t)$ is calculated using (24).

CHAPTER FIVE

A SPECIFIC SYSTEM EXAMPLE, INCLUDING EXPERIMENTAL RESULTS

5.1 DEFINITION OF THE SYSTEM

The prototype EIDI system constructed at The Wichita State University, and the results of the tests made on that system, have been described in detail by Dr. Robert Schrag [3]. Most of the material in this Chapter has been excerpted from Dr. Schrag's paper.

Figure 5A shows the prototype EIDI energy discharge system, omitting the capacitor charging circuit and the thyristor firing circuit. Two identical pulsing coils were operated in series, because that was the arrangement used in most of the de-icing tests. However, only one of the two coils was utilized in the coil-target assembly, which is detailed in Figure 5B.

The effective gap between the coil (copper) surface and the near surface of the target was .078 inch. A .032" thick 2024 T3 Aluminum disc was used as the target. Diameter of this disc was 5 inches. Two .05" thick phenolic spacer plates were used, one to maintain a fixed distance between the coil and the target, and the other to maintain the distance between the target and the rigid wooden support that prevented motion of the target. These plates could be removed, and a special magnetic field measuring plate (described in Section 5.4) inserted in their place in order to make measurements of the magnetic induction close to the surface of the target. Each coil consisted of

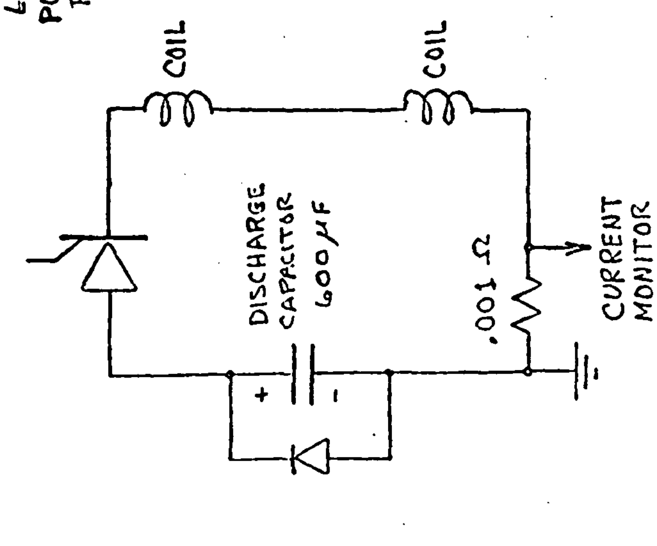

FIGURE 5A

ENERGY DISCHARGE
CIRCUIT

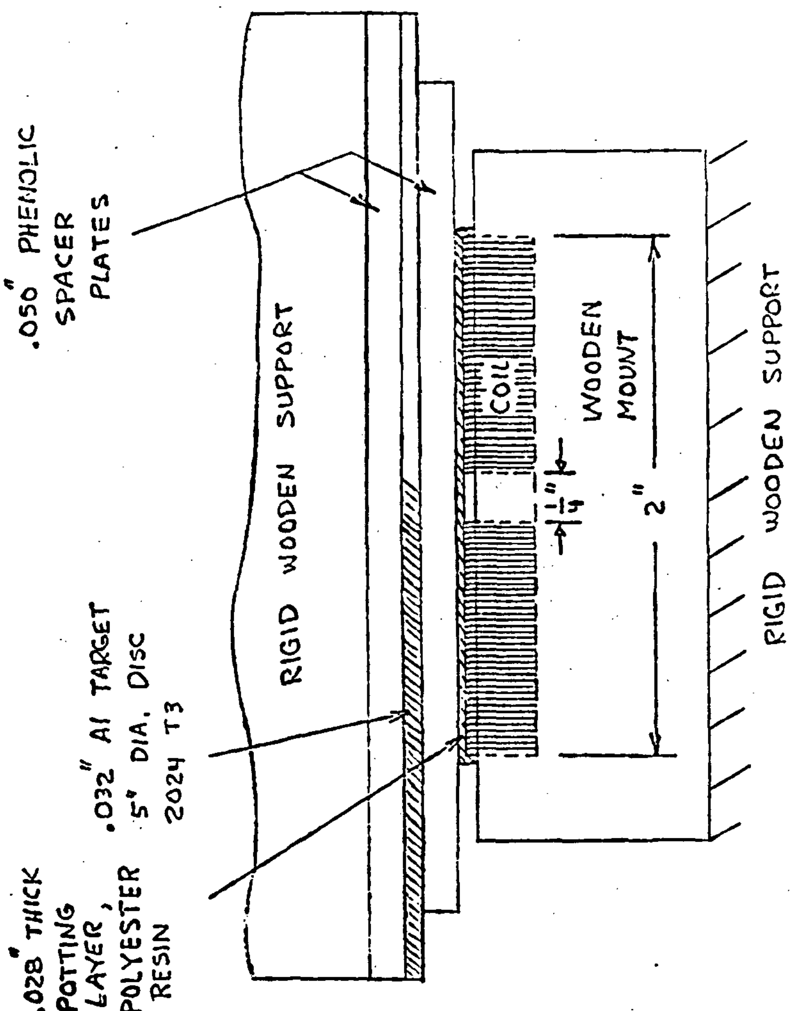

COIL DATA:
30 TURNS OF .024" × .183"
RECTANGULAR COPPER
WIRE, SINGLE LAYER
SPIRALLY WOUND

FIGURE 5B

DETAILS OF COIL · TARGET
ASSEMBLY

30 turns of .024" X .188" rectangular copper wire spirally wound in a single layer from an inner radius of .125" to an outer radius of 1". The initial capacitor voltage utilized for the experimental study was 400 volts.

5.2 COIL IMPEDANCE MEASUREMENTS

Impedance measurements on the coil next to the target were made using an impedance bridge. The inductance determined by these measurements, for several frequencies, appears in the table below. Impedance measurements were also made on the coil when the metal target was removed. The real part of the impedance measured on the coil without the target in place was subtracted from the real part of the impedance measured on the coil with the target in place. This increase in resistance due to the target is given in the table below.

RESISTANCE INCREASE AND INDUCTANCE - COIL AND METAL TARGET

Frequency (Hertz)	Inductance (Microhenries)	Resistance Increase (Milliohms)
500	18.6	8.2
1000	17.0	23.0
2000	14.6	48.0
4000	12.6	77.0

5.3 CURRENT WAVEFORM

Initially, current in the coil was measured indirectly by measuring the voltage across the .001 ohm non-inductive resistor in Figure 5A. Difficulties with this approach prompted the purchase of a current transformer from Pearson Electronics, Inc. Using this transformer and a storage oscilloscope, we observed the current shown in

Figure 5C.

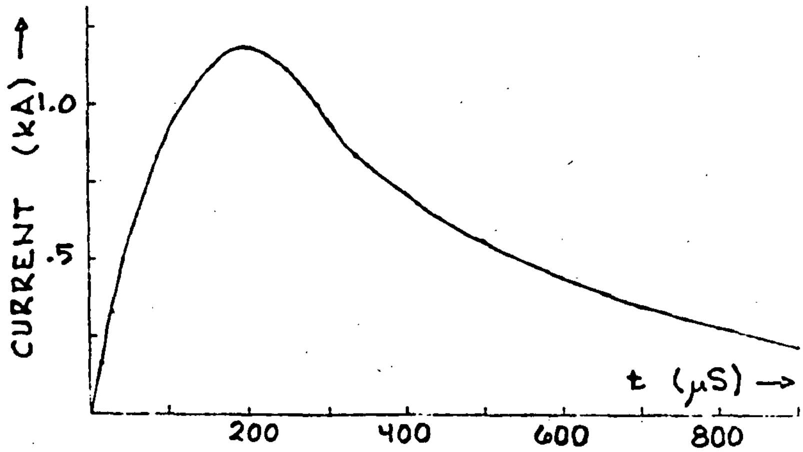

FIGURE 5C
COIL CURRENT

5.4 MAGNETIC FIELD MEASUREMENTS

A magnetic field measuring plate was constructed in the manner illustrated in Figure 5D. Shallow concentric grooves were cut into both sides of a .05 inch phenolic disc, with radius increments of .2",

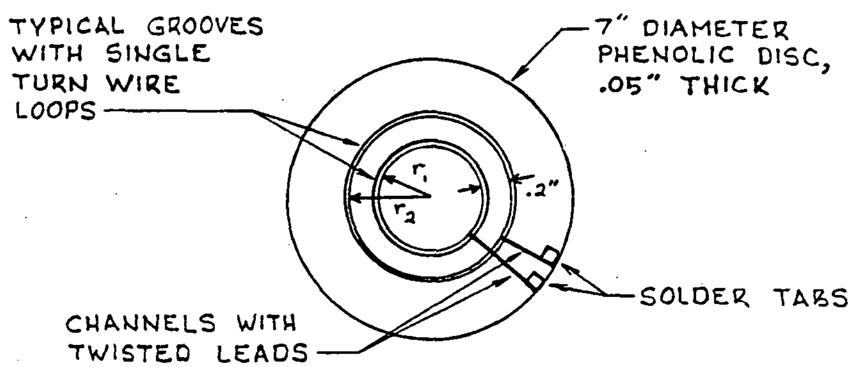

FIGURE 5D
PARTIAL ILLUSTRATION
FIELD MEASURING PLATE

starting at r=.2" and ending at r=2.0". Single turn loops of .006" diameter wire were then cemented into these grooves, and their twisted leads brought out to solder tabs through radial channels.

For measuring the fields on either side of the target, the measuring plate simply substituted for the corresponding phenolic spacer plate in Figure 5B. A measurement of the axial flux density was derived from the induced voltage in any two neighboring loops connected in series opposition. For the two loops illustrated in Figure 5D, for example,

$$B_z(t) = 1550 \frac{\int_0^t v(\tau)\, d\tau}{\pi (r_2^2 - r_1^2)}$$

where B_z is in teslas, r is in inches, and V is in volts. This value is the average axial flux density over the area between the two induction loops. In the further use of this result, we will assume the flux density to apply at a radius midway between the two loops.

To measure the radial component of flux density at any radius, the front and back loops at that radius are connected in series opposition, and calculations are made from

$$B_r(t) = 1550 \frac{\int_0^t v(\tau)\, d\tau}{2\pi r h}$$

where r is the radius of the two induction loops and h is their separation, both in inches.

Plots of the magnetic induction fields obtained from these tests with the target in place are shown at selected radii in Figures 5E, 5F, 5G, and 5H. All B_r data showed an anomolous behavior (irregularities) at r=.4" relative to r=.6". A separate check was made, in

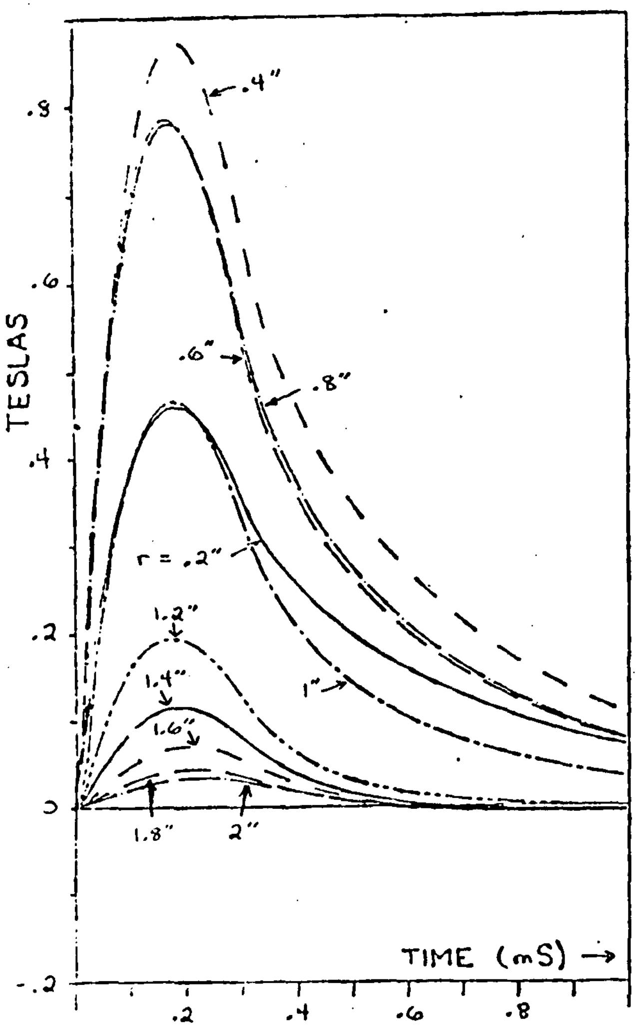

FIGURE 5E

B_r vs. TIME, NEAR SIDE

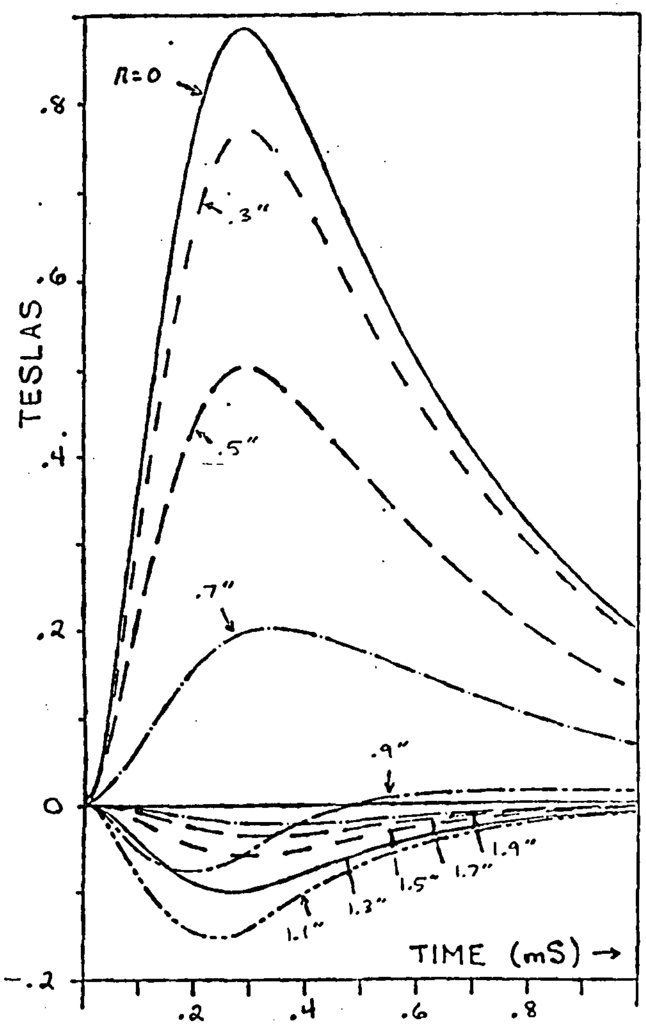

FIGURE 5F

B_z vs. TIME, NEAR SIDE

ORIGINAL PAGE IS
OF POOR QUALITY

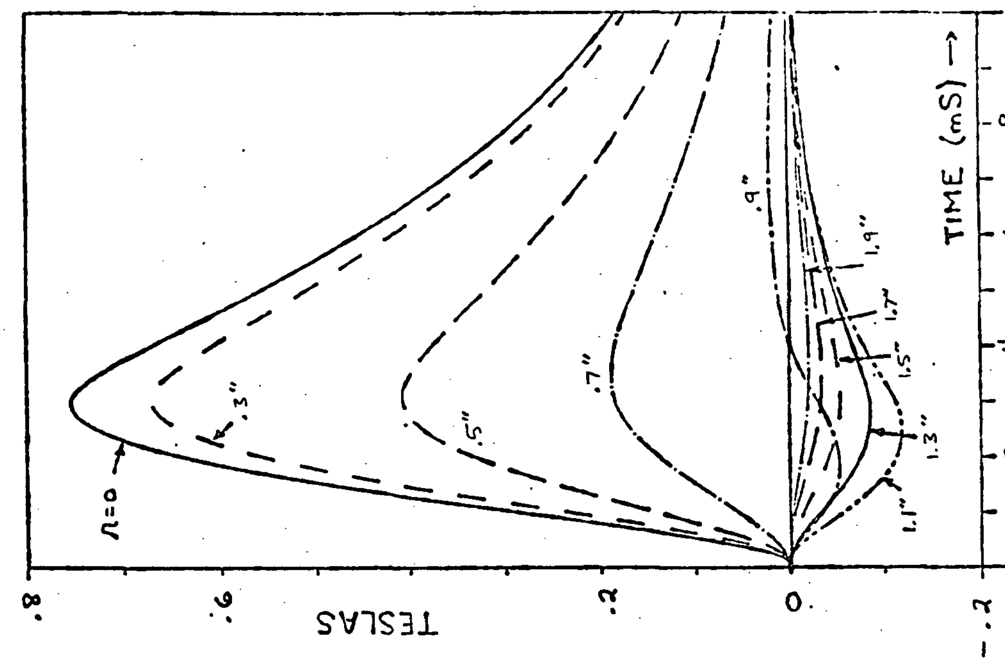

FIGURE 5H

B_z vs. TIME, FAR SIDE

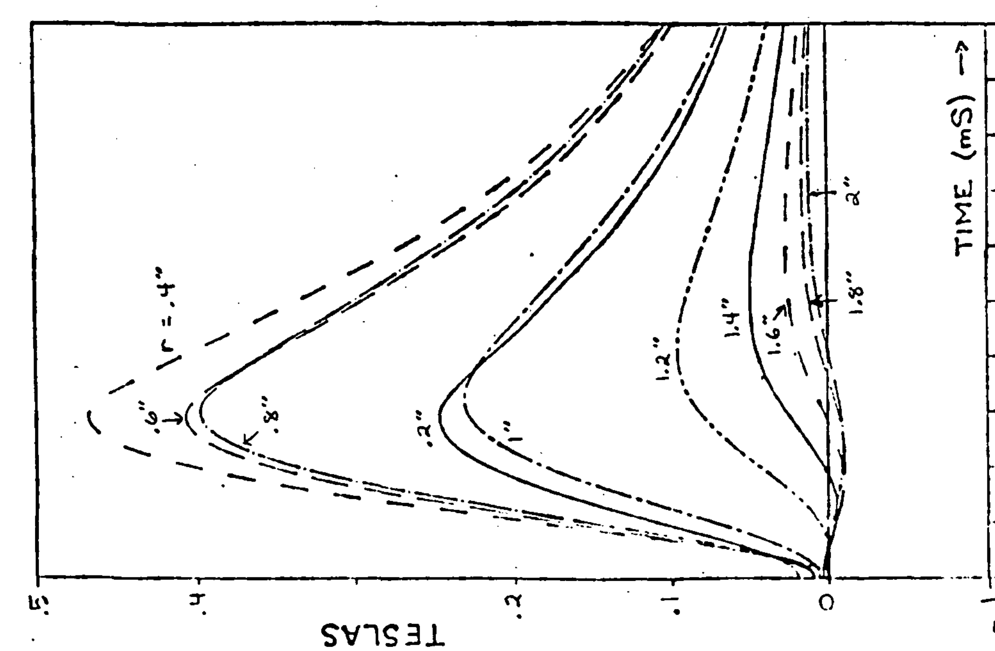

FIGURE 5G

B_r vs. TIME, FAR SIDE

which the plate was reversed (interchanging the two sides). This produced a reversal of the irregularities, so the effect was probably due to an inaccuracy in the construction of the plate.

5.5 MEASUREMENT OF IMPULSE TO TARGET

The final step in the experiment was the measurement of the impulse delivered to the target when the capacitor was discharged through the coil. This was done indirectly, using a ballistic pendulum. The impulse so measured was approximately .012 lb-sec.

CHAPTER SIX

COMPUTER ANALYSIS ON THE SYSTEM EXAMPLE

6.1 INTRODUCTION

Theoretical background for the numerical computations described in this chapter were developed in Chapters 3 and 4. This chapter will concentrate on a description of the numerical methods used to implement the theoretical development contained in these earlier chapters to predict the performance of the prototype EIDI system described in Chapter 5. The sections that follow are arranged in the order of the Figure 1 Analysis Flow Diagram, beginning with Block 4 of that diagram. This is the order in which the computations were actually accomplished.

All computations were performed in FORTRAN IV on an IBM 370. Source code was compiled with the IBM furnished G level compiler.

6.2 COIL IMPEDANCE

Equation (4) of Chapter 4, repeated as equation (1) below, is the coil impedance predicted by the transmission line model. Numerical evaluation of the integral in (1) is discussed in this section.

$$Z(\omega) = 2\pi \int_0^\infty [K'(\lambda)]^2 \sum_{i=0}^{2} E'_\phi(z_i, \lambda, \omega)\, d\lambda \qquad (1)$$

Two common methods are in use to allow quadrature of an improper integral such as the integral above [21]. In the first method, a transformation of variables is performed prior to construction of an algorithm for estimating the value of the integral. This transformation is chosen in such a manner that the new integral has finite limits. The second method simply replaces the infinite upper limit with a finite upper limit, selected such that the part of the integral thus ignored contributes little to the true value of the integral. Such a method can be employed only if the integrand decays sufficiently rapidly as the variable of integration increases. Since the controlling factor in the leading behavior of the asymptotic expansion, as lambda tends to infinity, of the integrand in (1) is $e^{-\lambda g}$, with g a constant, the second method was chosen for use in the numerical evaluation of (1).

A large amount of high quality mathematical software is available today [22], [23]. Because of the complexity and cost of writing quality mathematical algorithms, most numerical analysts suggest that complex scientific calculations be performed using algorithms written by experts [24], [25]. An 8 panel adaptive Newton-Cotes algorithm entitled QUANC8, described in [25], was chosen to perform the quadrature in (1). A user of QUANC8 may select the relative and absolute error performances desired, and the program then attempts to estimate the value of the integral within the selected error criteria. One of the parameters in the subroutine QUANC8 is an output variable that contains an estimated error bound on the returned value.

Direct computer evaluation of (1) consumes a large amount of CPU time, and is consequently expensive. This is due mostly to the appearance of the factor $[K'(\lambda)]^2$ in the integrand. (Note that $K'(\lambda)$ is defined by an integral containing a Bessel function. This makes K' oscillatory, shown in Figure 6A.) It was possible to decrease this cost considerably by calculating $K'(\lambda)$ using QUANC8 and fitting a cubic spline function to the calculated $K'(\lambda)$ for use in evaluating (1). The algorithms used for generating the spline function coeffic-

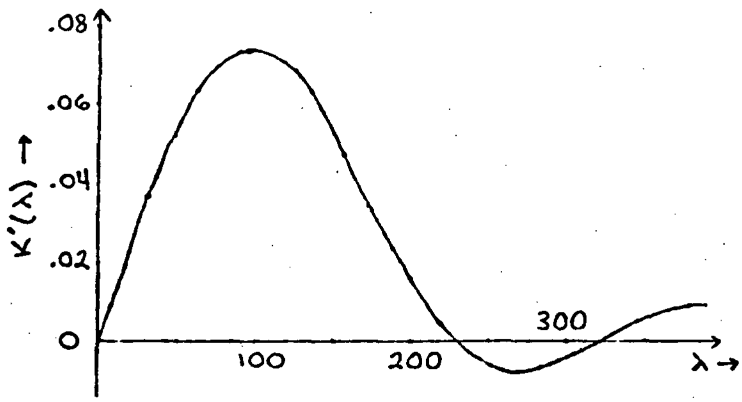

FIGURE 6A
OSCILLATORY
NATURE OF $K'(\lambda)$

ients and for evaluating the spline function at a given argument are entitled SPLINE and SEVAL, respectively, and are described in [25].

Once a spline function approximation for $K'(\lambda)$ was available, QUANC8 was used to individually estimate the real part (the coil resistance increase due to the metal target) and the imaginary part (the coil reactance) of (1) at selected frequencies. Appendix A contains a listing of the complete program, with the subroutines referred to, for evaluating the real part of (1). A simple modification of this program allows the imaginary part of the impedance to be evaluated.

Initial estimates of the real and imaginary parts of the integral in (1) were obtained using an upper limit of 680. Following this, the programs were run again with an upper limit of 240. Little difference was seen in the results of the two calculations, leading to the conclusion that the coil resistance and inductance estimates were good.

Figure 6B shows the effects of the upper limit of integration in evaluating the imaginary part of the integral in (1) for three different frequencies.

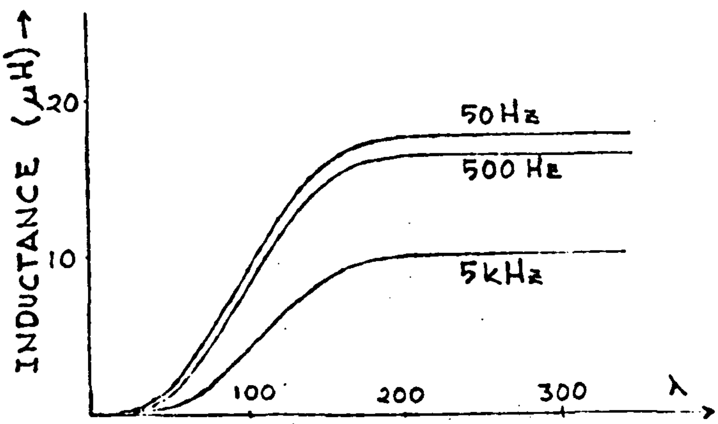

FIGURE 6B
CALCULATED INDUCTANCE
VS.
UPPER INTEGRATION LIMIT

Figures 6C and 6D on the following page show the resistance increase and inductance calculated as described above. Measured values of these parameters are also shown for comparison.

6.3 CURRENT WAVEFORM

6.3.1 Introduction

As discussed in Chapter 2, three factors preclude a simple calculation of the coil current in the EIDI prototype system. These three factors are the nonlinear diode and SCR, and the presence of the metal target next to the coil.

The effects of the target on the coil were taken into account by calculating the coil resistance increase and inductance at several frequencies, as described in the previous section. These two frequency dependent parameters were then approximated with cubic spline functions, again using the subroutine SPLINE. This provided the

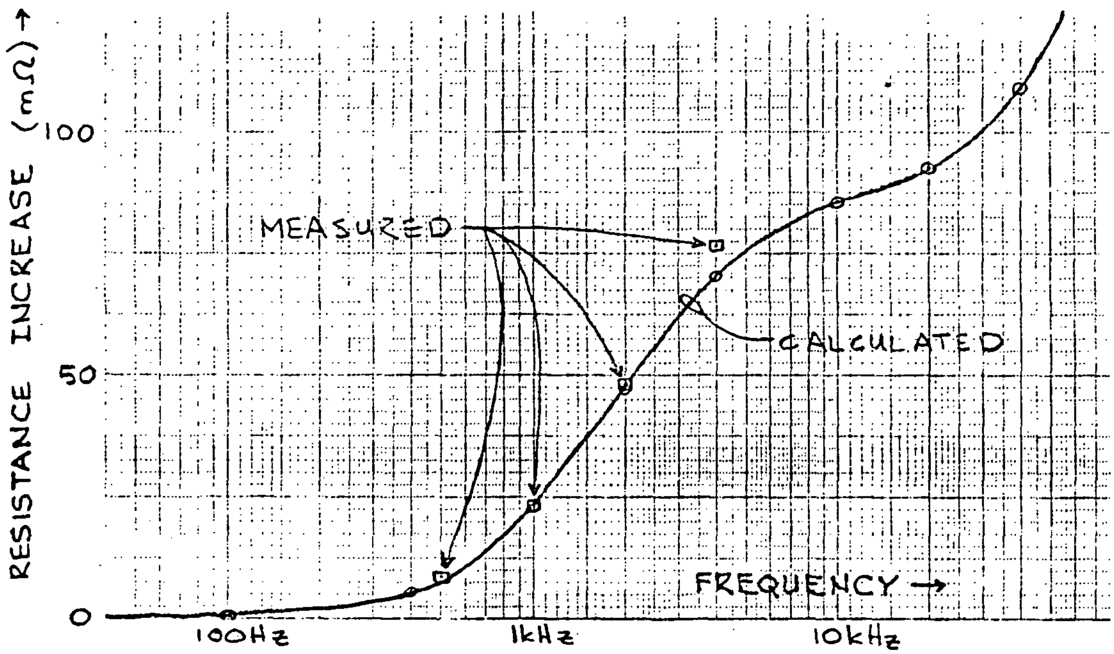

FIGURE 6C

COIL RESISTANCE INCREASE DUE TO METAL TARGET

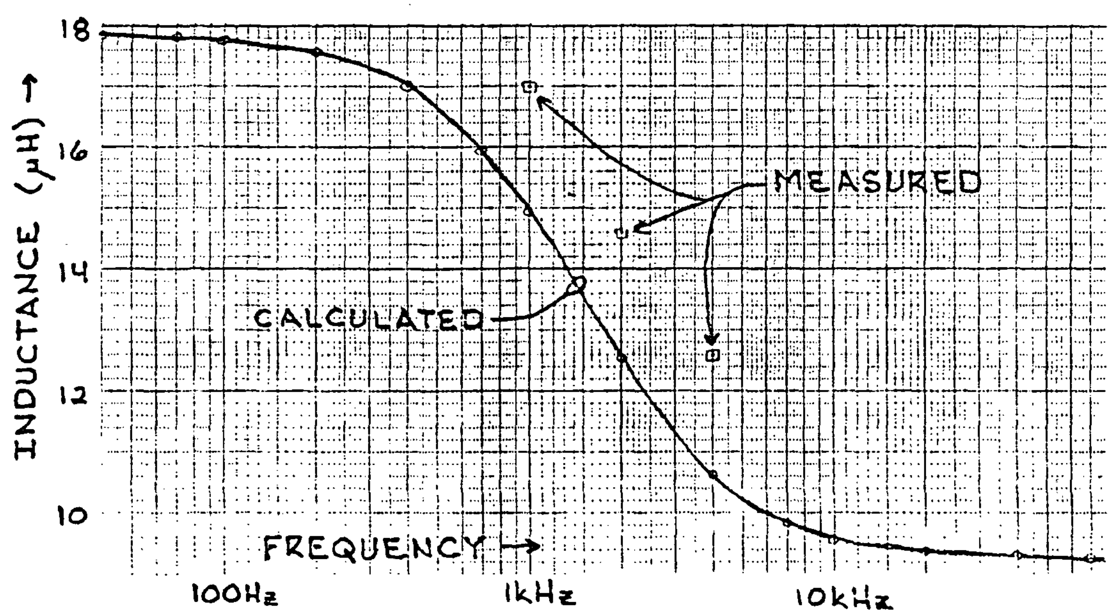

FIGURE 6D

COIL INDUCTANCE IN PRESENCE OF METAL TARGET ability to calculate computationally inexpensive yet sufficiently accurate coil impedances for use in frequency domain circuit calculations.

6.3.2 Current Before Clamp Diode Conduction

Although the circuit is nonlinear due to the diode and SCR, it is amenable to treatment in a piecewise linear fashion. The frequency domain model of the circuit, valid between the time the SCR is initially triggered and the time the capacitor voltage becomes zero, is shown in Figure 6E. In this Figure, the EIDI system capacitor is modeled as an ideal discharged capacitor in series with a voltage

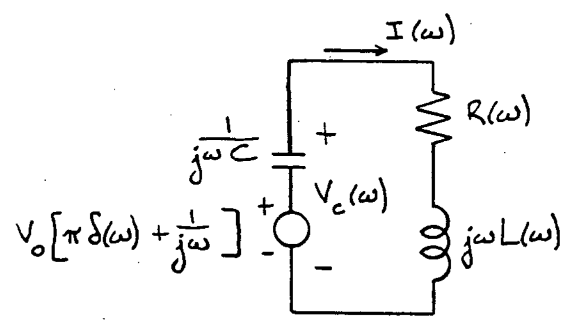

FIGURE 6E
FREQUENCY DOMAIN
CIRCUIT MODEL
CLAMP DIODE OFF

source. This voltage source has a value of zero volts for all time prior to t=0. At t=0, it instantly rises to the amplitude and polarity V_o of the initial voltage on the actual capacitor, modeling the triggering of the SCR into instantaneous full forward conduction. Voltages and currents calculated from this model are good approximations to their corresponding quantities in the physical EIDI prototype circuit as long as the diode in parallel with the capacitor is not conducting.

The frequency dependent resistor appearing in Figure 6E is a composite lumped model of several loss mechanisms in the physical circuit. It includes the loss in the coil due to the presence of the metal target next to the coil (calculated as described in the previous section), resistance of the ribbon conductor used to wind the coil (corrected for skin effect), and the resistance of the cable used to connect the coil and capacitor. Resistance in the cable was modeled as frequency independent, with a measured D.C. value of .054 ohms. Coil winding resistance was calculated from

$$R_{AC} = R_{DC} \; \mathrm{Real}\left\{ \frac{h}{2} \, \frac{1+j}{\delta} \, \coth\left(\frac{h}{2} \, \frac{1+j}{\delta} \right) \right\}$$

where

R_{DC} = D.C. coil resistance = .0235 ohms
h = coil thickness = .00477 meters
δ = copper skin depth = $1/\sqrt{\pi f \mu \sigma}$
f = frequency in Hertz
μ = copper permeability = $4\pi \times 10^{-7}$ henries/meter
σ = copper conductivity = 3.48×10^{7} mhos/meter

Resistance R_{AC} applies to both the coil next to the target and the idler coil (see Figure 5A).

Similarly, the frequency dependent inductance L in Figure 6E arises from more than one source. First, there is the inductance of the coil next to the target (calculated in the section above). Second, the idler coil and cable connecting the capacitor to the coil had a combined measured inductance of 23 microhenries, which was assumed to be independent of frequency. As these two inductances are in series in the circuit, they are added together to obtain a value for L.

The leakage reactance and measuring circuit impedance reflected into the actual circuit by the current transformer used to measure the current were felt to be too small to be significant, and were not included in the Figure 6E model.

By inspection, the Fourier transform of the current in Figure 6E is given by

$$I(\omega) = \frac{V_o\left[\pi\delta(\omega) + \frac{1}{j\omega}\right]}{\frac{1}{j\omega C} + R(\omega) + j\omega L(\omega)}$$

$$= \frac{CV_o\left[\pi j\omega\delta(\omega) + 1\right]}{1 + j\omega CR(\omega) - \omega^2 CL(\omega)}$$

$$I(\omega) = \frac{CV_o}{1 - \omega^2 CL(\omega) + j\omega CR(\omega)} \qquad (2)$$

Note that the delta distribution multiplies its own argument, and consequently contributes nothing to the time domain current i(t). Equation (2) is the basis for the current calculation, valid until the capacitor voltage becomes zero and the clamp diode in parallel with the capacitor begins conducting. For simplicity and cost considerations, an inverse discrete Fourier transform (IDFT) [36] was chosen to approximately invert $I(\omega)$. To sufficiently minimize the effects of the IDFT approximation to the continuous inverse Fourier transform, a 1024 point transform with a sample time of 5 microseconds was chosen. This makes the folding frequency 100kHz, which is considerably above any significant frequencies measured in the spectrum of the current in the prototype EIDI system. The 200kHz frequency window of the IDFT is sufficiently large that "windowing" effect errors in the time domain response are not too great. (These errors are primarily manifested as Gibbs' ripples on the intitial current calculated in Section 6.3.3, described in Section 6.3.4 and shown in Figure 6G.)

Appendix B contains a listing of the program used to calculate the coil current in the manner described above.

In order to determine how long a time this calculated current approximates the actual circuit current, a second calculation was performed using the circuit model in Figure 6E. The model predicts a frequency domain voltage corresponding to the physical EIDI capacitor voltage of

$$V_c(\omega) = V_o\left[\pi\,\delta(\omega) + \frac{1}{j\omega}\right] - \frac{V_o\left[\pi\,\delta(\omega) + \frac{1}{j\omega}\right]\frac{1}{j\omega C}}{\frac{1}{j\omega C} + R(\omega) + j\omega L(\omega)}$$

$$V_c(\omega) = CV_o\,\frac{j\omega L(\omega) + R(\omega)}{(j\omega)^2 CL(\omega) + j\omega CR(\omega) + 1} \tag{3}$$

The term involving the delta distribution again contributes nothing to the inverse Fourier integral yielding the time domain voltage, and is dropped from consideration to yield (3). A 1024 point 5 microsecond sample time IDFT was used to approximately calculate the inverse Fourier transform of (3). Output from this program showed that the capacitor voltage would slew negatively through zero volts at t=279 microseconds. This is the time at which the diode across the capacitor is modeled as coming into conduction and acting as a short circuit. Beyond this time the model of Figure 6E is no longer valid, and consequently the current predicted by the model is no longer correct.

6.3.3 Current After Clamp Diode Conduction

Once the diode comes into conduction, the model of the EIDI circuit for all future time is as shown in Figure 6F. The inductance

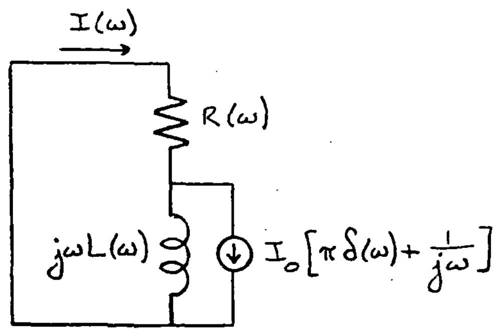

FIGURE 6F
FREQUENCY DOMAIN
CIRCUIT MODEL
CLAMP DIODE ON

and resistance in this circuit have the same physical significance that they had in Figure 6E, and their values are calculated for any desired frequency using the same algorithms. For computational convenience, time is "reset" to zero in this circuit, even though the circuit does not come into existance until t=279 microseconds in the Figure 6E circuit. Since the current in the coil is not initially zero, the circuit's magnetic energy storage is modeled by including a DC current source in parallel with a frequency dependent inductance. This current source is zero for all time prior to t=0, and for all future time has a D.C. value I_o equal to the value of the current in the Figure 6E circuit at the time the capacitor voltage became zero.

Current in the Figure 6F circuit is given in the frequency domain by

$$I(\omega) = I_o\left[\pi\delta(\omega) + \frac{1}{j\omega}\right] \frac{j\omega L(\omega)}{j\omega L(\omega) + R(\omega)}$$

$$I(\omega) = I_o \frac{L(\omega)}{j\omega L(\omega) + R(\omega)} \qquad (4)$$

Note that the term containing the delta distribution once again contributes nothing to the inverse Fourier transform of $I(\omega)$, and is dropped in (4). An IDFT was used to calculate the approximate inverse

Fourier transform of $I(\omega)$ given in (4), in exactly the same manner that the expression for $I(\omega)$ in (3) was inverted. The program is very similar to the one used in the Section 6.3.2 current calculation, contained in Appendix B.

6.3.4 Combining Pre- and Post Clamp Diode Conduction Current

Because of the presence of the current source in parallel with the inductor in Figure 6F, the current in this circuit model is discontinuous at t=0. Consequently, the current cannot be bandlimited. An inherent assumption in the use of the IDFT to approximately calculate a continuous inverse Fourier transform is that the signal is bandlimited. The time domain current calculated by the IDFT showed a small amount of ripple during the first 100 microseconds due to the current spectrum not being bandlimited. Prior to "joining" in time the current predicted by the Figure 6E model with the current predicted by the Figure 6F model, this ripple was eliminated by graphically choosing current values lying close to the IDFT predicted values that joined smoothly with the current from the Figure 6E model. Figure 6G illustrates this procedure. Current ripple amplitude was 54 amps peak to peak at t=10 microseconds, decaying to 1 amp peak to peak at t=75 microseconds, with time measured in the Figure 6F model. Figure 6H shows how good the agreement is between this piecewise linear model predicted current and the current measured in the prototype EIDI circuit.

With the model predicted current now available at 5 microsecond intervals from t=0 to t=5.12 milliseconds, a 1024 point 5 microsecond sample time DFT was performed on the current samples to estimate the

Fourier transform I (ω) of the model current. This transform is needed for use in calculating the magnetic induction fields from the Hankel space transmission line coil-target model, as discussed in the next section.

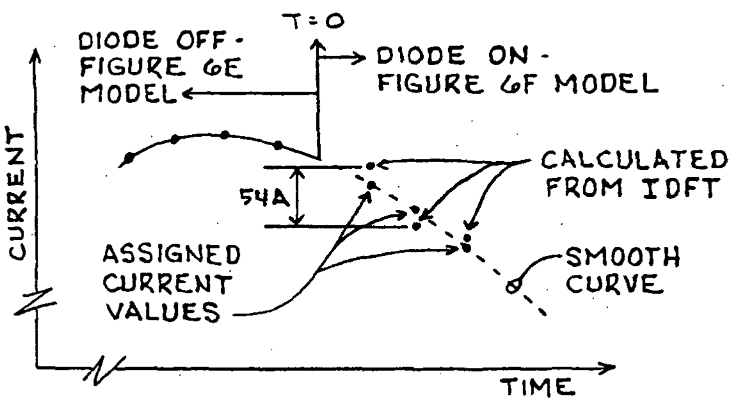

FIGURE 6G
PRE- AND POST- CLAMP DIODE CONDUCTION CURRENT

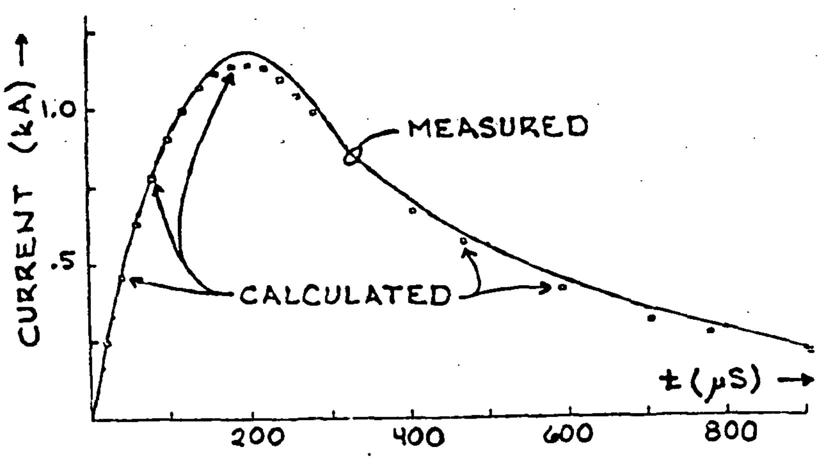

FIGURE 6H
COIL CURRENT

6.4 MAGNETIC INDUCTION

6.4.1 Introduction

Knowledge of the radial and axial magnetic induction on the coil side face of the target is required for calculation of the total force on the target. Although conceptually simple, the numerical calculation of these two fields presented more computational difficulties than were encountered in the combined total of all other calculations performed. Initial attempts at calculating the magnetic induction, performed using single precision arithmetic and using professionally written quadrature routines, produced results that were incorrect by orders of magnitude.

6.4.2 Radial Magnetic Induction on the Coil Side Face of the Target

Expression (5) shows the iterated improper integral that is to be evaluated numerically to calculate the time domain radial magnetic induction $B_r(0,r,t)$. This integral is the inverse Fourier-Hankel transform of the total current at z=0 given by (11) of Chapter 4.

$$B_r(0,r,t) = \mu \int_{\omega=-\infty}^{\infty} e^{j\omega t}\, I(\omega) \quad \times \tag{5}$$

$$\int_{\lambda=0}^{\infty} \frac{K'(\lambda)\, e^{-\lambda g}\left[1 + e^{-\lambda h/3} + e^{-2\lambda h/3}\right] J_1(\lambda r)\, \lambda\, d\lambda}{1 + \dfrac{\lambda}{\sqrt{\lambda^2 + j\omega\mu\sigma}} \; \dfrac{1 + \dfrac{\lambda}{\sqrt{\lambda^2+j\omega\mu\sigma}} \tanh(\gamma_m d)}{\dfrac{\lambda}{\sqrt{\lambda^2+j\omega\mu\sigma}} + \tanh(\gamma_m d)}} \, d\omega$$

Quadrature of iterated integrals is almost always difficult [21]. One of the most common methods of evaluating such integrals, the Monte Carlo method, could not even be considered for use in (5) due to the enormity of the very expensive and random complex function evaluations required by such an approach. Furthermore, the integrand in (5) is extremely oscillatory, having both positive and negative complex values, due to the Bessel function in the inverse Hankel transform, the function $K'(\lambda)$, and the complex exponential in the inverse Fourier transform. Quadrature of such integrands is all but impossible using Monte Carlo methods due to extreme smearing [25], [26]. It is the oscillatory nature of the integrand in (5) that makes its evaluation difficult.

After much trial and error, a workable approach to quadrature of the integral in (1) was obtained, and is described in this section. No claim is made for optimality or near optimality in this approach. After many computations of the magnetic induction had been performed using this procedure, it became apparent that simplifications could be made, while still obtaining sufficient accuracy. However, these simplifications have not been tested, and the original approach to quadrature of the integral in (5) will be described.

Measurements of the radial magnetic induction near the coil side face of the target in the EIDI prototype system provide some insight into a suitable numerical procedure for evaluating the integral in (1). The Fourier transforms of these observed fields are smooth (higher order derivatives with respect to frequency are small) with most of the energy confined to relatively low frequencies. This suggested the use of an IDFT to numerically perform the inverse Fourier transformation in (1). Further impetus for use of the IDFT is given by noting that the DFT procedure for calculating the Fourier transform $I(\omega)$ of the current, described in the preceding section, yielded transform values at equally spaced frequencies. These are the appropriate frequencies for calculating a 1024 point IDFT, with a 5 microsecond sample time, of the Fourier space radial magnetic induction. However, numerical evaluation of the inverse Hankel transform in (5) at the 513 frequencies needed for calculating a 1024 point IDFT yielding a real sequence is prohibitively expensive. This expense was avoided by using the previously noted fact that the expected Fourier transform of the magnetic induction is smooth, with most of the energy confined to low frequencies. Accordingly, the inverse Hankel transform in (5) was evaluated at only 77 frequencies, chosen to provide a reasonable representation of the behavior of the Fourier transform of the known radial magnetic induction. Spline function approximations were then fitted to the real and imaginary parts of the calculated inverse Hankel transforms. The IDFT routine to calculate the desired time domain magnetic induction uses these spline functions to form $B_r(0,r,\omega)$ at the 1024 frequencies needed.

With a procedure for evaluating the inverse Fourier integral in (1) available, a search for a suitable method for quadrature of the inverse Hankel integral was initiated. The infinite upper limit of this integral was simply replaced with a suitably large finite upper limit, due to the controlling factor in the leading behavior of the asymptotic expansion of the integrand being $e^{-\lambda g}$. With the problem of the infinite upper limit gone, the remaining difficulties may be divided into two somewhat overlapping classes.

Selection of a suitable algorithm for performing the quadrature is essential if accurate results are to be obtained. Most of the common quadrature algorithms are incapable of dealing with oscillatory integrals without some help. Even with the best of help, examples of problems where these algorithms completely fail abound. This has given rise to highly specialized techniques for quadrature involving oscillatory integrands [27], [28], [29], [30]. The use of one of these specialized algorithms was avoided by writing a double precision Gaussian quadrature routine [21], [31]. This routine was then used to perform the inverse Hankel integration in (5) over the range $0 < \lambda < 10$, then over the range $10 < \lambda < 20$, etc., stopping when the desired upper limit of integration had been reached. The results of these integrations, which can be interpreted as terms in a sequence that are to be summed, were then added together first using straightforward addition, and then using the Euler series summation convergence acceleration algorithm DTEUL from the NASA Lewis Research Analysis Center Software Library [34]. For each radius at which the radial magnetic induction was evaluated, and for each of the 77 Fourier frequencies, good agreement was achieved between the results of these two summation methods.

Several different finite upper limits were used to take the place of the infinite upper limit in the inverse Hankel quadrature. It was experimentally determined that upper limits greater than 1000 resulted in very little change in the calculated induction fields.

The second problem area concerned the precision of the FORTRAN implemented on the 370. Single precision floating point word length on the IBM 370 is approximately 7 decimal digits (24 bit mantissa) [25]. This is insufficient for nearly all complex scientific calculations [32], [33]. Double precision floating point word length on the 370 is approximately 15 decimal digits (56 bit mantissa) [25], and was used for all computations involving the inverse Hankel integral. Without the use of double precision arithmetic, inverse Hankel quadrature was impossible due to smearing.

Although the use of double precision greatly reduced the effects of smearing, it created problems of its own. A double precision Bessel function, and a double precision algorithm for $K'(\lambda)$ become necessary to evaluate (5). Simply converting a single precision algorithm for $K'(\lambda)$ to double precision does not yield sufficient accuracy to obtain good results. Double precision Bessel function algorithms were unavailable at The Wichita State University. Double precision algorithms were written for $J_0(x)$ and $J_1(x)$. The double precision algorithm that was written for $K'(\lambda)$ is described in Appendix C. Finally, the complete program for calculating the time domain radial magnetic induction, given by (5), may be found in Appendix D. Figure 6I provides a comparison between the measured radial magnetic induction close to the coil side face of the target, and the predicted radial magnetic induction on the coil side face of the target (output from the program in Appendix D).

6.4.3 Axial Magnetic Induction on the Coil Side Face of the Target

The magnetic induction B_z on the target next to the coil is calculated by performing an inverse Fourier transform on (22) in Section 4.4 of Chapter 4. Then

$$B_z(o, r, t) = \mu \mathcal{F}^{-1}\{H_z(o, r, t)\}$$

$$= \mu \mathcal{F}^{-1}\left\{\frac{-1}{j\omega}\int_0^\infty V(o,\lambda,\omega)\lambda^2 J_o(\lambda r)\,d\lambda\right\}$$

where $V(o, \lambda, \omega)$ is given by (16) in Section 4.3.1 of Chapter 4. Substituting (16) from Chapter 4 into the above,

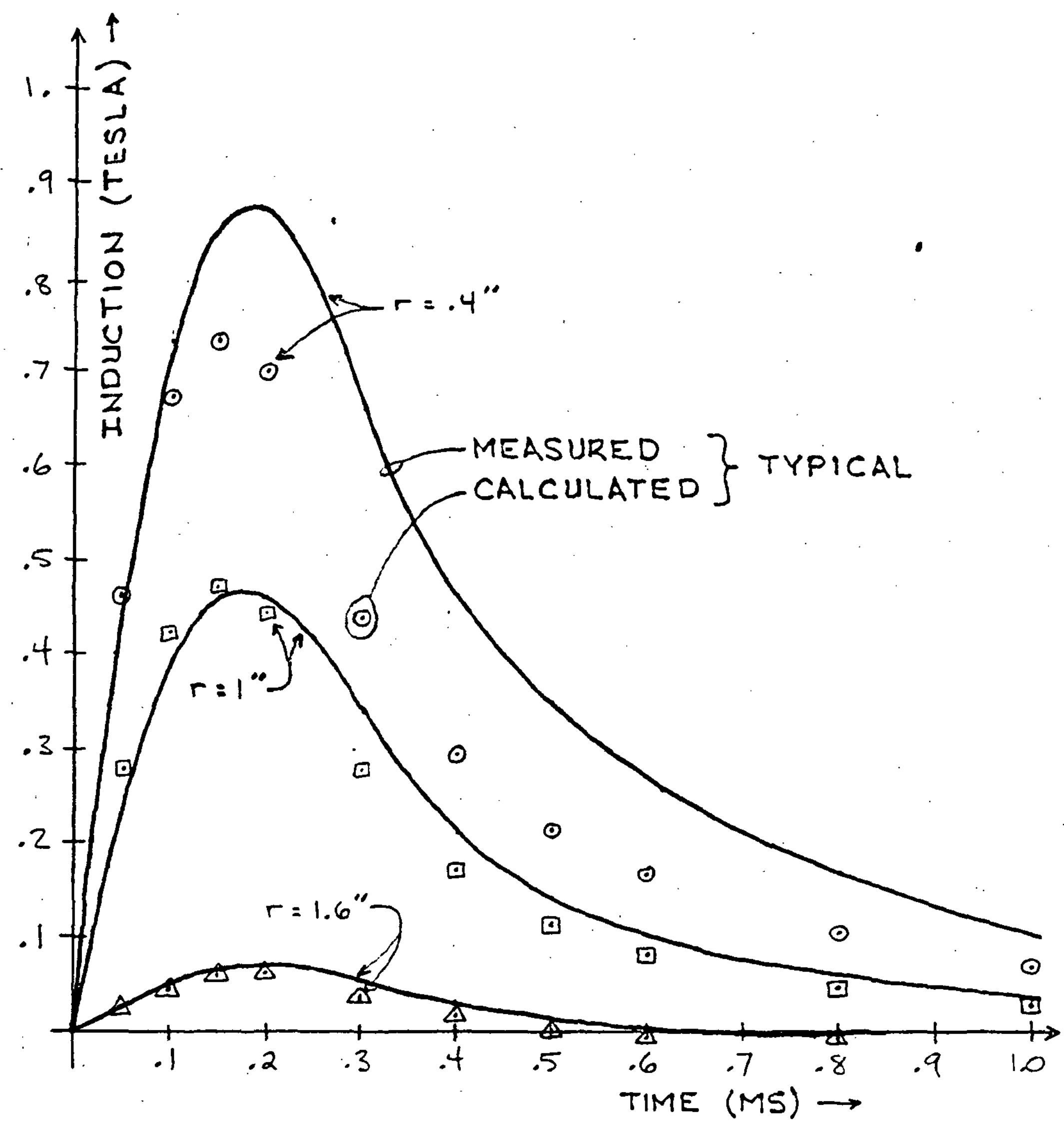

FIGURE 6I
B_r VS. TIME, NEAR SIDE

$$B_z(0,r,t) = -\mu \int_{\omega=-\infty}^{\infty} e^{j\omega t}\, I(\omega) \quad \times \tag{6}$$

$$\int_{\lambda=0}^{\infty} \frac{K'(\lambda)\mu\lambda e^{-\lambda g}\left(1+e^{-\lambda h/3}+e^{-2\lambda h/3}\right) J_0(\lambda r)\, d\lambda}{1+\dfrac{\sqrt{\lambda^2+j\omega\mu\sigma}}{\lambda}\;\dfrac{\dfrac{\lambda}{\sqrt{\lambda^2+j\omega\mu\sigma}}+\tanh(\gamma_m d)}{1+\dfrac{\lambda}{\sqrt{\lambda^2+j\omega\mu\sigma}}\tanh(\gamma_m d)}}\, d\omega$$

The similarity between (5) and (6) is evident, even though the order of the inverse Hankel transforms is different. Because of this similarity, the algorithms developed to perform the quadrature in (5) were used, with only evident minor changes necessary, to perform the quadrature in (6). A comparison at several different radii between the measured axial magnetic induction close to the coil side face of the target and the calculated axial magnetic induction on the surface of the target closest to the coil is shown in Figure 6J.

6.4.4 Magnetic Induction on the Opposite Face of the Target

Although it was not needed in the calculation of the force between the coil and target, the magnetic induction on the side of the target away from the coil was calculated for comparison with the measured induction close to the same target surface. Section 4.3 in Chapter 4 derived expressions for the total voltage V, and total current I, at the junction between the metal line and air line opposite the current sources. These quantities correspond respectively to the azimuthal electric intensity and the radial magnetic induction on the surface of the target opposite the coil.

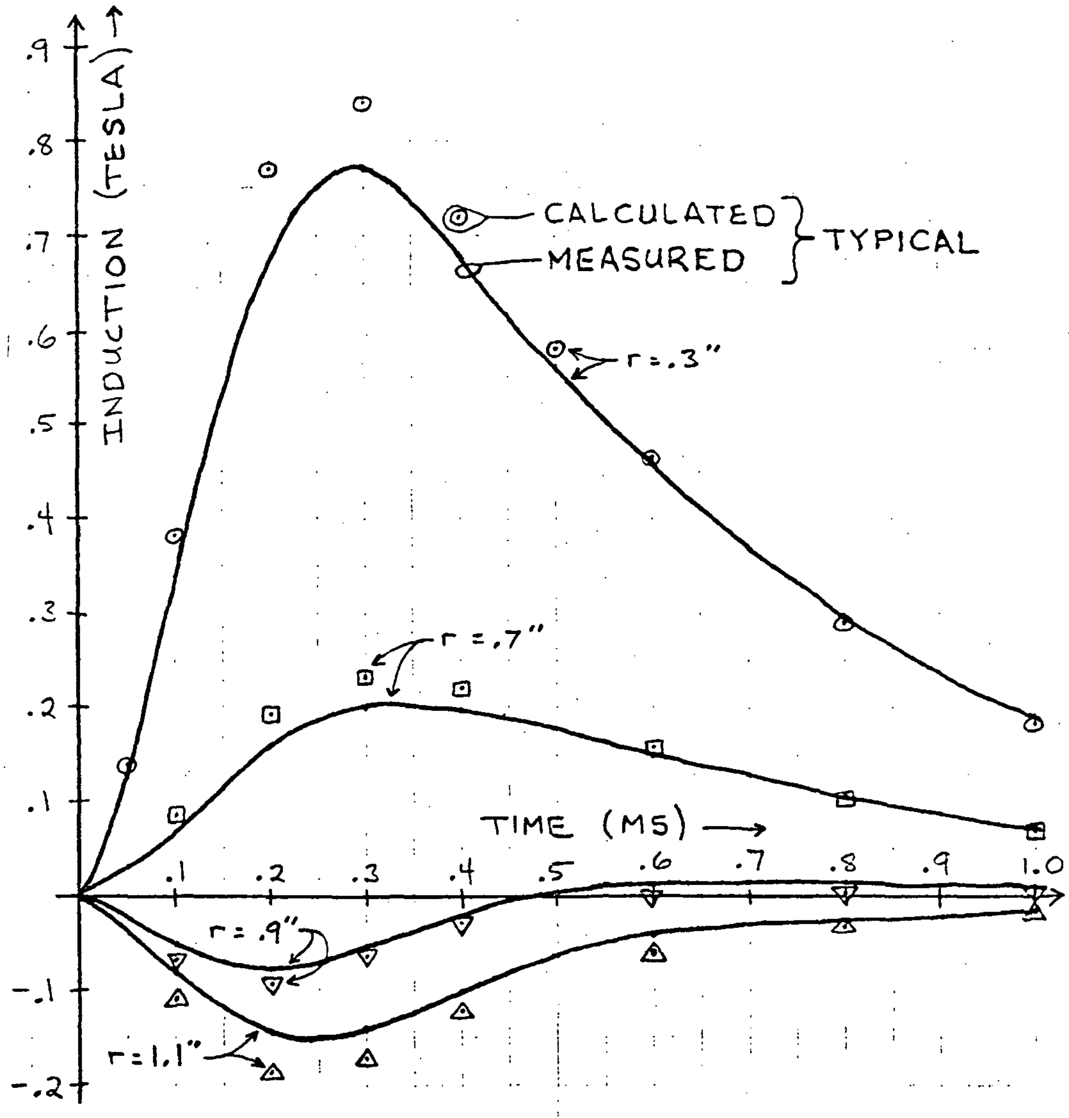

FIGURE 6J
B_z VS. TIME, NEAR SIDE

Inverse Fourier-Hankel transformation similar to that in (5), but with the integrand corresponding to the current I, given in Section 4.3, yields the radial magnetic induction. Only minor changes are necessary in the program whose listing appears in Appendix D to calculate the induction. Figure 6K provides a comparison between the measured and calculated radial magnetic induction close to and on the target surface away from the coil.

Inverse Fourier-Hankel transformation similar to that in (6), but with the integrand corresponding to the voltage V, given in Section 4.3, yields the axial magnetic induction. Figure 6L shows the comparison between the measured and calculated axial induction close to and on the target surface away from the coil.

6.5 FORCE VERSUS TIME

It was shown in Section 4.5 of Chapter 4 that the total force between the coil and target is given approximately by

$$F_z(t) \doteq \frac{\pi}{\mu}\int_0^{\infty}\left[B_z^2(0,r,t) - B_r^2(0,r,t)\right] r\, dr \qquad (7)$$

For use in this integral, radial magnetic induction was calculated at 5 microsecond intervals at radii .01 inch, .2 inch, and in .2 inch increments up to a maximum of 2.0 inch, on the surface of the target closest to the coil using the algorithms described in Section 6.4.2. Axial magnetic induction was also calculated at 5 microsecond intervals at radii .01 inch, .1 inch, and in .2 inch increments up to 1.9 inch, on the same target surface using the algorithms described in Section 6.4.3. Cubic spline functions were then fitted to the squares of the radial variation of these two magnetic fields at times 0, 50,

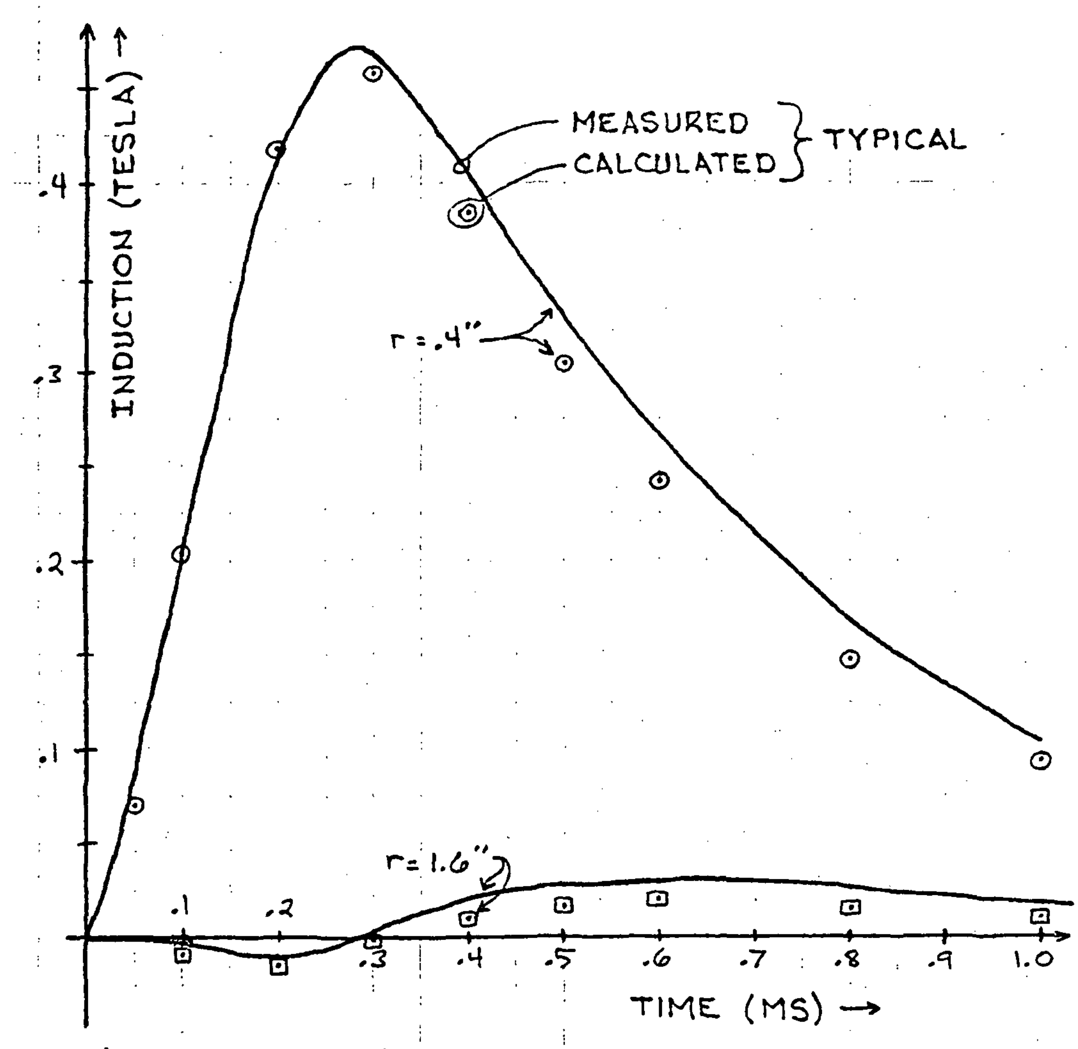

FIGURE 6K
B_r VS. TIME, FAR SIDE

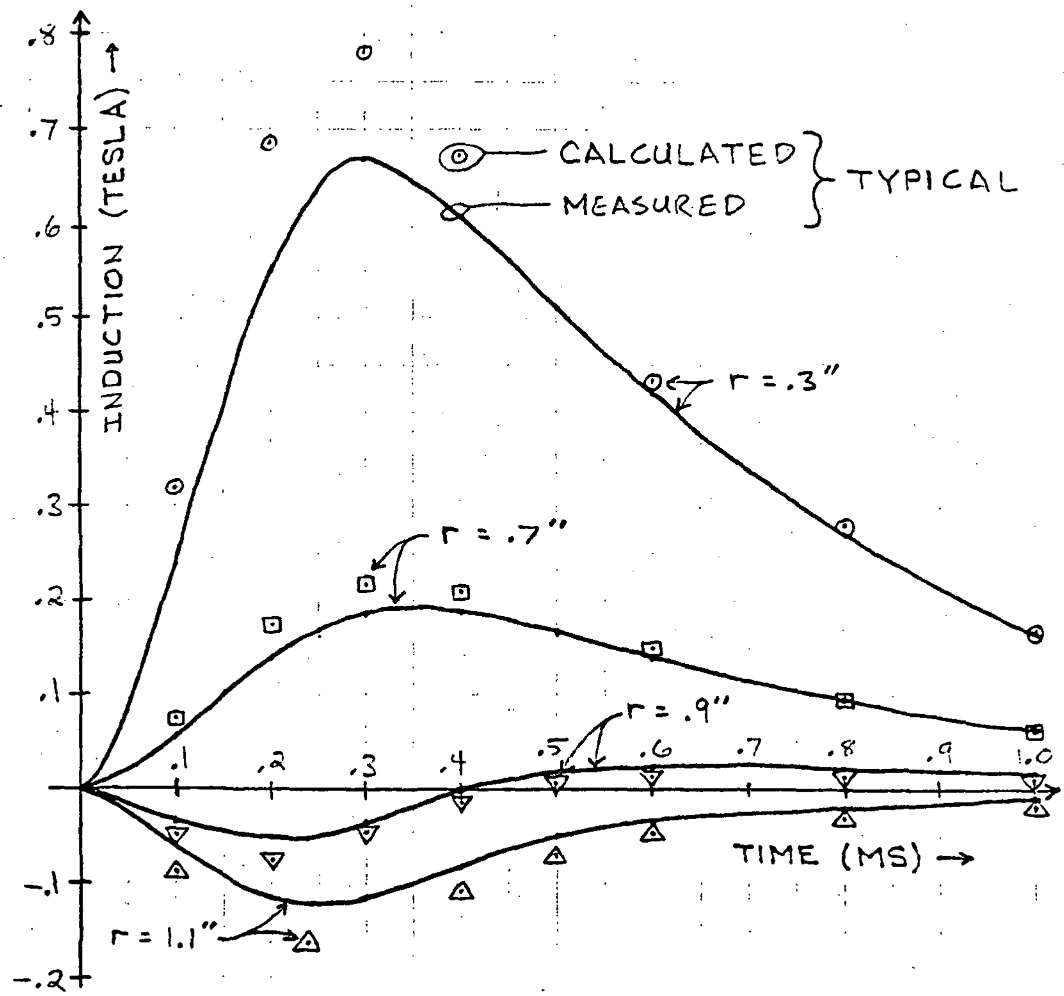

FIGURE 6L
B_z VS. TIME, FAR SIDE

100, 150, ..., 900, and 1125, 1400, and 2000 microseconds for use in performing the quadrature indicated in (7), using an upper limit of 1.9 inches. The quadrature was done exactly (to the limit of the machine arithmetic) on the spline function approximations to the squared fields by integrating the cubic polynomial form of the spline function between knots, and using the spline function coefficients in the result. Appendix E contains a listing of the FORTRAN program for performing this force calculation at t=50 microseconds.

Figure 6M shows the force versus time calculated using this procedure.

6.6 IMPULSE

Equation (25) in Chapter 4, repeated below, was used to calculate

$$\Gamma = \int_0^\infty F_z(t)\, dt$$

the impulse delivered to the target by the coil. A spline function was fitted, with time as the variable, to the force calculated in Section 6.5 above. An exact integration was performed on the cubic polynomials of the spline function between knots, with the result that the impulse calculated was .008 lb-sec. This is lower than the .012 lb-sec impulse measured using a ballistic pendulum. It should be noted that the quadrature of the force integral in (7) above used an upper limit of r=1.9 inches instead of infinity. Although the induction decays as the radius tends to infinity, an unknown part of the force has been ignored by not taking the induction fields at radii greater than 1.9 inches into account.

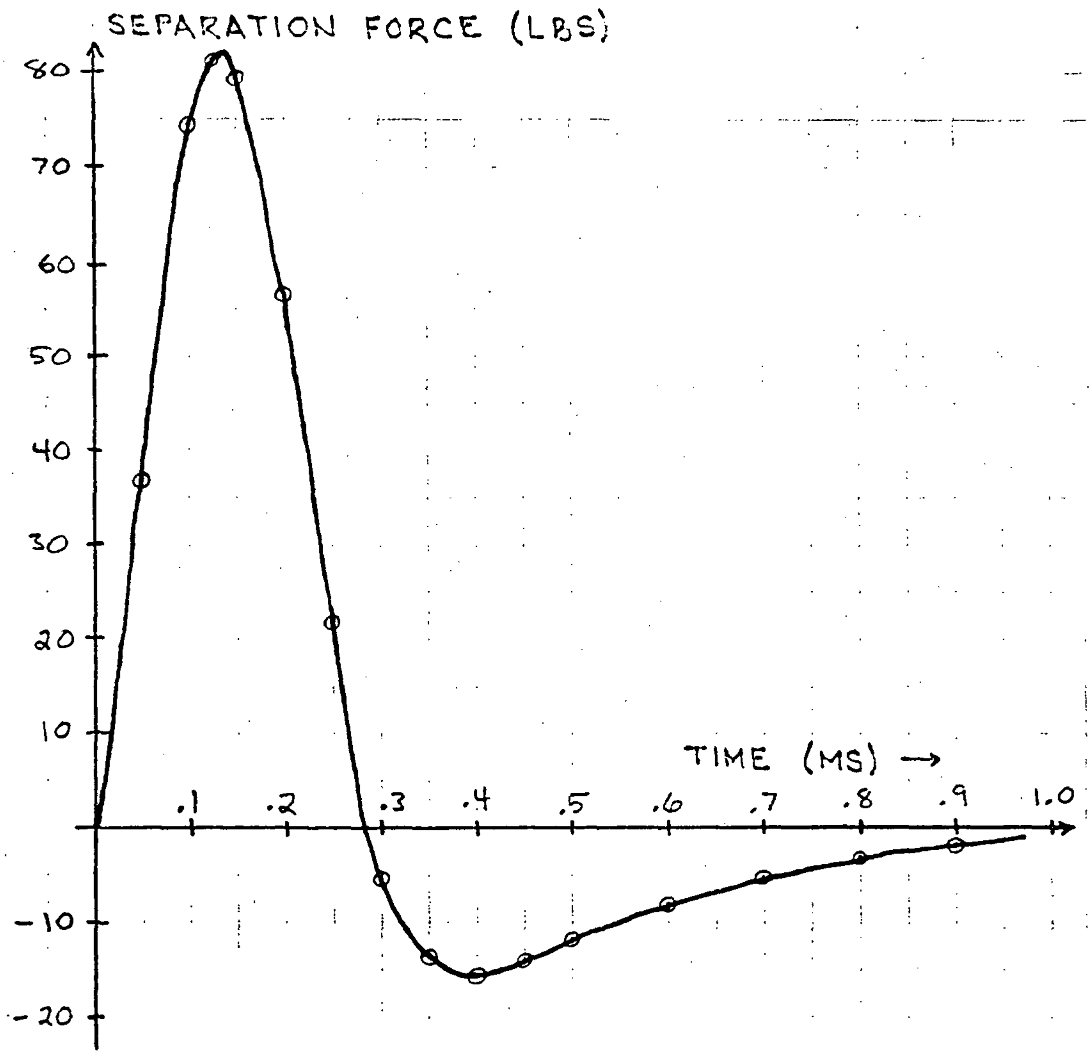

FIGURE 6M
FORCE BETWEEN COIL AND TARGET

CHAPTER SEVEN

CONCLUSION AND RECOMMENDATIONS FOR FURTHER WORK

7.1 CONCLUSION

7.1.1 Summary

A method of modeling the electrical system aspects of a coil and metal target configuration resembling a practical Electro-Impulse De-Icing installation, and a simple circuit for providing energy to the coil, was presented. The model was developed in sufficient theoretical detail to allow the generation of computer algorithms for the current in the coil, the magnetic induction on both surfaces of the target, the force between the coil and target, and the impulse delivered to the target. These algorithms were applied to a specific prototype EIDI test system for which the current, magnetic fields near the target surfaces, and impulse had previously been measured.

Coil impedance was the first quantity calculated using the algorithms. Agreement between the impedance calculated and the impedance measured was seen to be very good for the resistive part, and reasonable for the reactive part. Despite the simple model used for the circuit providing energy to the coil, excellent agreement was obtained between the predicted and measured coil current.

Measured and predicted magnetic induction fields were not directly compared, due to the fields having been measured close to, but not on, the target surfaces using spatial averaging methods. The only fields calculated were on the target surfaces, for use in calculation of the force between the coil and target. Nevertheless, there was seen to be very reasonable agreement between measured and calculated magnetic fields. The character of the time variation of these fields changed considerably with radial distance from the axis, and the algorithms correctly predicted these changes.

Calculation of the impulse easily provided the greatest disagreement between a predicted and measured quantity, with a -33% error in the calculated impulse. Impulse was measured using a ballistic pendulum containing the metal target, so, for this measurement, the metal target was no longer held rigid when the capacitor was discharged through the coil. This does not satisfy the model assumption of a stationary system. However, the period of the pendulum was sufficiently long that, during the time interval when most of the force was developed on the target, negligible motion of the pendulum should theoretically have occured. Motion of the target during the measurement of the impulse is not felt to be a satisfactory explanation for the discrepancy between the measured and calculated impulse. It was mentioned in Section 6.6, where the calculation of the impulse was described, that the infinite upper limit in the integral yielding the theoretical impulse had been replaced with a finite upper limit for the purpose of quadrature, thus incurring an unknown error. Our procedure for quadrature of the impulse integral is felt to be the most likely source of error in the calculated impulse.

7.1.2 Contributions by the Author

Reference [4] provided most of the basic methods used in this dissertation in modeling the interaction between the coil and target.

It was shown that an error had occured in the definition given in [4] of the characteristic impedance of a Hankel space transmission line, and the corrected definition was used in the theoretical development of the model. For many transmission line calculations, this error does not become evident because impedances occur in ratios (e.g., the voltage and current reflection coefficient calculations in Section 4.3.1).

Reference [4] provided no method of calculating the axial magnetic induction $B_z(z,r,t)$ from the transmission line model. An integral solution for this field, in terms of the transmission line voltage, was derived in Section 4.4. This solution allowed the use of nearly all of the algorithms developed for the calculation of the radial magnetic induction $B_r(z,r,t)$ in calculating the axial magnetic induction $B_z(z,r,t)$.

The most significant contribution of this work was the development of FORTRAN algorithms for performing the inverse Fourier-Hankel transformations yielding the induction fields, described in Section 6.4. While the author made no theoretical contributions in developing these algorithms, several diverse results from the fields of numerical analysis and approximation theory had to be applied in concert to create a working algorithm. During this development, an algorithm for the generation of Struve functions of the first and second orders was developed that, according to a computer search of the literature, is the most accurate reported.

7.2 RECOMMENDATIONS FOR FUTURE WORK

If the methods developed in this dissertation are to be applicable as design tools for EIDI systems, the algorithms for the calculation of the magnetic induction fields should be made more efficient. These algorithms, listed in Appendix D, take nearly half an hour of CPU time on the IBM 370 to calculate either the axial or the radial magnetic induction versus time at one specific radius. Both the radial and axial components are required, each at eleven different radii, for the force calculation described in Section 6.5. A minimum of eleven hours of CPU time is too great for the evaluation of the force-time profile of a proposed EIDI configuration. The least desirable feature of the methods presented in this dissertation is the inordinate CPU time required for the calculation of the induction fields. A sophisticated convergence acceleration routine could perhaps be devised specifically for more economic calculation of the induction fields.

Human intervention is required to proceed along the Analysis Flow Diagram of Figure 1 (page 4) in evaluating a specific EIDI system. This is because the outputs from the various programs, represented by such Figure 1 quantities as the coil impedance $Z(\omega)$, the current $i(t)$ and $I(\omega)$, are not in the form required as the inputs for the program at the next block in Figure 1. A significant amount of design automation could be accomplished by writing one long program, using as a skeleton the programs developed for this dissertation, that will take as input the geometry of the coil-target configuration and the circuit used to provide energy to the coil, and provide as output a force-time profile and the total impulse delivered to the target.

Not all possibilities have been exhausted in the search for an analytical (or semianalytical) solution to the EIDI design problem.

Perturbation techniques have been suggested as a possible method for analytical Hankel inversion in the calculation of the magnetic induction, and should be investigated, as this is the area suffering the greatest computational expense. Furthermore, analytical solutions (if sufficiently simple) are often capable of providing insight into a problem not provided by numerical solutions.

ORIGINAL PAGE IS
OF POOR QUALITY

APPENDIX A

FORTRAN SOURCE CODE FOR CALCULATING COIL RESISTANCE INCREASE DUE TO TARGET

```
C   FILE:  FEB21R FORTRAN
C   PROGRAM TO ESTIMATE RCOIL, USING VALUES OF LAMBDA FROM 0 TO 680.
C
C    VALUES OF THE E-FIELD ARE GENERATED DIRECTLY USING THE CODE
C    FROM THE FILE FEB2 FORTRAN.  VALUES OF KPRIME ARE OBTAINED FROM A
C    SPLINE FUNCTION APPROXIMATION.  VALUES OF RCOIL CALCULATED WILL BE
C    USED IN A NUMERICAL INVERSE FOURIER TRANSFORM TO CALCULATE CIRCUIT
C    QUANTITIES.
C
C   INITIALIZE
C
       COMMON W
       DATA PI/3.14159265/
       TWOPI=2.*PI
C
C   MAIN PROGRAM USING QUANC8
C
       A=0.01
       U=680.
C   PRINT OUTPUT HEADINGS
       WRITE(6,50) A,U
   50 FORMAT(' RESULTS OF NUMERICAL INTEGRATION FROM LAMBDA =',F4.1,' TO
     1',F6.1/)
C   GENERATE FREQUENCIES IN HERTZ
       DO 10 I=1,4
       DO 10 J=1,4
C   GENERATE FREQUENCIES IN A 1 - 2 - 4 - 7 SEQUENCE
       F=10.**I
       IF(J.EQ.2) F=2.*F
       IF(J.EQ.3) F=4.*F
       IF(J.EQ.4) F=7.*F
       W=TWOPI*F
       RELERR=1.E-8
       ABSERR=0.
       CALL QUANC8(A,U,ABSERR,RELERR,RESULT,ERREST,NOFUN,FLAG)
C   INTEGRATION DONE - OUTPUT COIL RESISTANCE CALCULATED
       RCOIL=TWOPI*RESULT*1000.
   10 WRITE(6,1010) F,RCOIL,ERREST
 1010 FORMAT(' FREQUENCY= ',F6.0,5X,'RCOIL= ',F7.3,' MILLIOHMS',5X,
     1'ERREST= ',E12.5)
       STOP
       END
C
C   COPIED SUBROUTINE QUANC8 FOLLOWS
       SUBROUTINE QUANC8(A,B,ABSERR,RELERR,RESULT,ERREST,NOFUN,FLAG)
       REAL FUN, A, B, ABSERR, RELERR, RESULT, ERREST, FLAG
       INTEGER NOFUN
       REAL W0,W1,W2,W3,W4,AREA,X0,F0,STONE,STEP,COR11,TEMP
       REAL QPREV,QNOW,QDIFF,QLEFT,ESTERR,TOLERR
       REAL QRIGHT(31),F(16),X(16),FSAVE(8,30),XSAVE(8,30)
       INTEGER LEVMIN,LEVMAX,LEVOUT,NOMAX,NOFIN,LEV,NIM,I,J
       LEVMIN = 1
       LEVMAX = 30
       LEVOUT = 6
       NOMAX = 5000
```

```
      NOFIN = NCMAX - 8*(LEVMAX-LEVOUT+2**(LEVOUT+1))
      W0 = 3956.0/14175.0
      W1 = 23552.0/14175.0
      W2 = -3712.0/14175.0
      W3 = 41984.0/14175.0
      W4 = -18160.0/14175.0
      FLAG = 0.0
      RESULT = 0.0
      COR11 = 0.0
      ERREST = 0.0
      AREA = 0.0
      NOFUN = 0
      IF(A.EQ.B) RETURN
      LEV = 0
      NIM = 1
      X0 = A
      X(16) = B
      QPREV = 0.0
      F0 = FUN(X0)
      STONE = (B-A)/16.0
      X(8) = (X0 + X(16))/2.0
      X(4) = (X0 + X(8))/2.0
      X(12) = (X(8) + X(16))/2.0
      X(2) = (X0 +X(4))/2.0
      X(6) = (X(4) + X(8))/2.0
      X(10) = (X(8) + X(12))/2.0
      X(14) = (X(12) + X(16))/2.0
      DO 25 J = 2,16,2
         F(J) = FUN(X(J))
   25 CONTINUE
      NOFUN = 9
   30 X(1) = (X0 + X(2))/2.0
      F(1) = FUN(X(1))
      DO 35 J = 3,15,2
         X(J) = (X(J-1) + X(J+1))/2.0
         F(J) = FUN(X(J))
   35 CONTINUE
      NOFUN = NOFUN + 8
      STEP = (X(16) - X0)/16.0
      QLEFT = (W0*(F0 + F(8)) + W1*(F(1) +F(7)) + W2*(F(2) +F(6))
     1 +W3*(F(3) + F(5)) + W4*F(4))*STEP
      QRIGHT(LEV+1)=(W0*(F(8)+F(16))+W1*(F(9)+F(15))+W2*(F(10)+F(14))
     1 +W3*(F(11)+F(13))+W4*F(12))*STEP
      QNOW = QLEFT + QRIGHT(LEV+1)
      QDIFF = QNOW - QPREV
      AREA = AREA + QDIFF
      ESTERR = ABS(QDIFF)/1023.0
      TOLERR = AMAX1(ABSERR,RELERR*ABS(AREA))*(STEP/STONE)
      IF(LEV.LT.LEVMIN) GO TO 50
      IF(LEV.GE.LEVMAX) GO TO 62
      IF(NOFUN.GT.NOFIN) GO TO 60
      IF(ESTERR.LE.TOLERR) GO TO 70
   50 NIM = 2*NIM
      LEV = LEV +1
      DO 52 I = 1, 8
         FSAVE(I,LEV) = F(I+8)
         XSAVE(I,LEV) = X(I+8)
   52 CONTINUE
      QPREV = QLEFT
      DO 55 I = 1, 8
         J = -I
         F(2*J+18) = F(J+9)
         X(2*J+18) = X(J+9)
   55 CONTINUE
      GO TO 30
   60 NOFIN = 2*NOFIN
      LEVMAX=LEVOUT
      FLAG=FLAG+(B-X0)/(B-A)
      GO TO 70
```

```
   62 FLAG=FLAG+1.0
   70 RESULT=RESULT+QNOW
      ERREST=ERREST+ESTERR
      COR11=COR11+QDIFF/1023.0
   72 IF(NIM.EQ.2*(NIM/2)) GO TO 75
      NIM= NIM/2
      LEV = LEV-1
      GO TO 72
   75 NIM = NIM + 1
      IF(LEV.LE.0) GO TO 80
      QPREV = QRIGHT(LEV)
      X0 = X(16)
      F0 = F(16)
      DO 78 I = 1, 8
         F(2*I) = FSAVE(I,LEV)
         X(2*I) = XSAVE(I,LEV)
   78 CONTINUE
      GO TO 30
   80 RESULT = RESULT + COR11
      IF(ERREST.EQ.0.0) RETURN
   82 TEMP = ABS(RESULT) + ERREST
      IF(TEMP.NE.ABS(RESULT)) RETURN
      ERREST = 2.0*ERREST
      GO TO 82
      END
C
C  COPIED SUBPROGRAM SEVAL FOLLOWS
      REAL FUNCTION SEVAL(N,U,X,Y,B,C,D)
      REAL U,X(N),Y(N),B(N),C(N),D(N)
      DATA I/1/
      IF(I.GE.N) I=1
      IF(U.LT.X(I)) GOTO 10
      IF(U.LE.X(I+1)) GOTO 30
   10 I=1
      J=N+1
   20 K=(I+J)/2
      IF(U.LT.X(K)) J=K
      IF(U.GE.X(K)) I=K
      IF(J.GT.I+1) GOTO 20
   30 DX=U-X(I)
      SEVAL=Y(I)+DX*(B(I)+DX*(C(I)+DX*D(I)))
      RETURN
      END
C
C  SUBPROGRAM FUN(LAMB) TO EVALUATE THE INTEGRAND FOR QUANC8
      FUNCTION FUN(LAMB)
      REAL LAMB,KPRI,MUO/12.56637E-7/,LAMBDA(48),KPRIME(48),B(48),C(48),
     1D(48)
      COMMON W
      COMPLEX CMPLX,CSQRT,CEXP,ZPDZA,IN,ZXDZA,RHOT,H,E,T1,HR2,HRO,CC,CG,
     1BC,BG,AC,AG,ZA,ZASQ,E2,E1,E3,H3,EPO,HR1
      DATA SIGMA/1.74E7/,HD3/.00159/,G/.00278/,DD/.0008128/,IFLAG/1/
C  READ IN SPLINE INTERPOLATION DATA FROM FILE KPSPL COEFF
C  FIRST CHECK TO SEE IF COEFFICIENTS ALREADY READ
      IF(IFLAG.NE.1) GOTO 10
      DO 1 I=1,48
    1 READ(2,1000) LAMBDA(I),KPRIME(I),B(I),C(I),D(I)
 1000 FORMAT(F6.1,4(1X,E15.6))
C  FIRST, EVALUATE THE REAL AND IMAGINARY PARTS OF THE E-FIELDS REQUIRED
C   FOR THE INTEGRATION - USES CODE FROM FILE FEB2 FORTRAN
C  FOLLOW STEPS OUTLINED IN "METHOD"
      IF(LAMB.EQ.0.) LAMB=1.E-20
   10 ZPDZA=(1.,0.)/CSQRT(CMPLX(1.,W*MUO*SIGMA/(LAMB*LAMB)))
      T=EXP(-LAMB*HD3)
      IN=CMPLX((T*T+T+1)*EXP(-LAMB*G),0.)
      RHOT=((1.,0.)-ZPDZA)/((1.,0.)+ZPDZA)
      T1=RHOT*CEXP(CMPLX(-2.*LAMB*DD,0.)/ZPDZA)
      ZXDZA=((1.,0.)+T1)*ZPDZA/((1.,0.)-T1)
      H3=IN/((1.,0.)+ZXDZA)
      ZA=CMPLX(0.,W*MUO/LAMB)
      E3=H3*ZXDZA*ZA
```

```
C   CALCULATE EP2
      T=EXP(LAMB*G)
      AG=CMPLX((T+1./T)/2.,0.)
      BG=CMPLX((T-1./T)/2.,0.)*ZA
      ZASQ=ZA*ZA
      CG=BG/ZASQ
      E2=AG*E3+BG*H3
      HR2=CG*E3+AG*H3
      EP2R=REAL(E2)
      EP2I=AIMAG(E2)
C   CALCULATE EP1
      T=EXP(LAMB*HD3)
      AC=CMPLX((T+1./T)/2.,0.)
      BC=CMPLX((T-1./T)/2.,0.)*ZA
      CC=BC/ZASQ
      E1=AC*E2+BC*(HR2-(1.,0.))
      HR1=CC*E2+AC*(HR2-(1.,0.))
      EP1R=REAL(E1)
      EP1I=AIMAG(E1)
C   CALCULATE EP0
      EP0=AC*E1+BC*(HR1-(1.,0.))
      EP0R=REAL(EP0)
      EP0I=AIMAG(EP0)
C   EVALUATE KPRI USING THE SPLINE INTERPOLATION
      KPRI=SEVAL(48,LAMB,LAMBDA,KPRIME,B,C,D)
C   NOW EVALUATE THE INTEGRAND AND RETURN
      FUN=LAMB*KPRI*KPRI*(EP2R+EP1R+EP0R)
      IFLAG=2
      RETURN
      END
```

```
RESULTS OF NUMERICAL INTEGRATION FROM LAMBDA = 0.0 TO 680.0

FREQUENCY=     10.     RCOIL=    0.004 MILLIOHMS     ERREST=  0.96085E-13
FREQUENCY=     20.     RCOIL=    0.017 MILLIOHMS     ERREST=  0.11895E-11
FREQUENCY=     40.     RCOIL=    0.068 MILLIOHMS     ERREST=  0.14812E-11
FREQUENCY=     70.     RCOIL=    0.207 MILLIOHMS     ERREST=  0.16755E-10
FREQUENCY=    100.     RCOIL=    0.418 MILLIOHMS     ERREST=  0.23993E-10
FREQUENCY=    200.     RCOIL=    1.589 MILLIOHMS     ERREST=  0.30565E-09
FREQUENCY=    400.     RCOIL=    5.592 MILLIOHMS     ERREST=  0.38682E-09
FREQUENCY=    700.     RCOIL=   13.841 MILLIOHMS     ERREST=  0.34003E-09
FREQUENCY=   1000.     RCOIL=   22.783 MILLIOHMS     ERREST=  0.33792E-09
FREQUENCY=   2000.     RCOIL=   47.373 MILLIOHMS     ERREST=  0.52783E-08
FREQUENCY=   4000.     RCOIL=   70.588 MILLIOHMS     ERREST=  0.41543E-08
FREQUENCY=   7000.     RCOIL=   81.442 MILLIOHMS     ERREST=  0.58640E-08
FREQUENCY=  10000.     RCOIL=   85.525 MILLIOHMS     ERREST=  0.64146E-08
FREQUENCY=  20000.     RCOIL=   92.622 MILLIOHMS     ERREST=  0.39609E-08
FREQUENCY=  40000.     RCOIL=  109.270 MILLIOHMS     ERREST=  0.49584E-08
FREQUENCY=  70000.     RCOIL=  142.962 MILLIOHMS     ERREST=  0.64945E-08
```

APPENDIX B

FORTRAN SOURCE CODE FOR CALCULATING
COIL CURRENT BEFORE CLAMP DIODE CONDUCTION

```
C     PROGRAM TO PERFORM NUMERICAL FOURIER INTEGRAL INVERSION TO CALCULATE
C      THE CURRENT IN THE COIL IN THE WING CIRCUIT (BEFORE THE
C      DIODE CLAMP CUTS IN).  THIS PROGRAM INCLUDES THE FREQUENCY
C      DEPENDENCE OF THE COIL RESISTANCE AND INDUCTANCE.  OUTPUT FROM THIS
C      PROGRAM WILL BE USED TO CALCULATE THE SPECTRUM OF THE CURRENT.
C      THIS PROGRAM IS ADAPTED FROM SERCJR FORTRAN.
C
      COMPLEX F1(2048),CMPLX,CONJG
      REAL L,LSIMID
      DATA N/2048/,T/5.E-6/,C/600.E-6/,RCABLE/.054/,RDC/.047/,LSIMID/23.
     *E-6/,PI/3.141593/
      TTOT=FLOAT(N)*T
      DELTAF=1./TTOT
      DELTAW=2.*PI*DELTAF
      KODE=-1
C
C     FORM COMPLEX SPECTRUM MATRIX
C
      IEND=N/2+1
      DO 5 I=1,IEND
      W=FLOAT(I-1)*DELTAW
C     CHECK FOR FREQUENCY W=0
      IF(W.NE.0.) GOTO 3
      R=RCABLE+RDC+.004E-3
      L=LSIMID+17.865E-6
      GOTO 4
C     W .NE. 0  -  CALCULATE RESISTANCE R AS THE SUM OF 3 TERMS: A CONSTANT
C      D.C. TERM (RCABLE); SKIN EFFECT IN COIL (RAC); AND LOSS IN SKIN OF
C      WING (COILR)
    3 R=RCABLE+RAC(W)+COILR(W)
C     CALCULATE INDUCTANCE AS THE SUM OF 2 TERMS: A CONSTANT TERM DUE TO
C      THE SIMMONDS AND IDLER (LSIMID); AND A TERM DUE TO THE COIL IN THE
C      WING (COILL)
      L=LSIMID+COILL(W)
C     NOW FORM THE CONSTANTS USED IN EVALUATION OF THE FOURIER TRANSFORM
C      OF THE TIME VARYING PART OF THE CIRCUIT CURRENT
    4 P1=L*C
      P2=R*C
C     NOW FORM THE MATRIX VALUES
    5 F1(I)=(1.,0.)/CMPLX(1.-W*W*P1,W*P2)
      ISTART=N/2+2
      DO 7 I=ISTART,N
    7 F1(I)=CONJG(F1(N+2-I))
C
      CALL FFT(KODE,N,DELTAF,F1,10)
C
C     EXPRESS TTOT IN MILLISEC, T IN MICROSEC
      TTOTP=TTOT*1000.
      TP=T*1.E6
C     BEGIN OUTPUT OF RESULTS
      WRITE(6,201) N,TTOTP,TP
  201 FORMAT('1NUMBER OF POINTS=',I4/' TOTAL TIME INTERVAL= ',F7.3,' MIL
     1LISEC',/' SAMPLING PERIOD= ',F7.3,' MICROSEC'//' OUTPUT FROM PROGR
     2AM MAY22A FORTRAN'//)
      WRITE(6,100)
  100 FORMAT('  CIRCUIT CURRENT    -    FREQUENCY DEPENDENT L, R'//'    T
     1IME(MSEC)',5X,'  TOTAL CURRENT RESPONSE'/,T23,'REAL',15X,'IMAG'/)
      FSC=400.*C
      DO 20 I=1,100
      DT=FLOAT(I-1)*T*1000.
      F1(I)=CMPLX(FSC,0.)*F1(I)
   20 WRITE(6,200) DT,F1(I)
  200 FORMAT(1X,F12.3,1X,2(F15.5,5X))
   10 STOP
      END
```

ORIGINAL PAGE IS
OF POOR QUALITY

```
      FUNCTION RAC(W)
C
C   SUBPROGRAM TO EVALUATE SKIN EFFECT RESISTANCE RAC OF COIL AS A
C    FUNCTION OF THE RADIAN FREQUENCY W
C
      COMPLEX CMPLX,CEXP,TAU,TAUHD2,T1,T1R
      REAL MU/1.256637E-6/
      DATA H/.00477/,SIGMA/3.48E7/,RDC/.047/
      DELTA=SQRT(2./(W*MU*SIGMA))
      TAU=(1.,1.)/CMPLX(DELTA,0.)
      TAUHD2=TAU*CMPLX(H/2.,0.)
      T1=CEXP(TAUHD2)
      T1R=(1.,0.)/T1
      RAC=RDC*REAL(TAUHD2*(T1+T1R)/(T1-T1R))
      RETURN
      END
      FUNCTION COILR(W)
C
C   SUBPROGRAM TO EVALUATE COIL RESISTANCE COILR (DUE TO PROXIMITY OF
C    WING SKIN) AS A FUNCTION OF THE RADIAN FREQUENCY W
C
      REAL FREQ(24),RCOIL(24),BR(24),CR(24),DR(24)
      DATA PI/3.141593/,IFLAG/1/
      IF (IFLAG.NE.1) GOTO 5
C   READ IN COEFFICIENTS FROM FILE RCOIL COEFF FOR SPLINE FUNCTION
C    INTERPOLATION
      DO 1 I=1,24
    1 READ(2,100) FREQ(I),RCOIL(I),BR(I),CR(I),DR(I)
  100 FORMAT(F8.0,4(1X,E15.6))
      TWOPI=2.*PI
      IFLAG=-1
    5 F=W/TWOPI
      IF (F.GT.10.) GOTO 10
      COILR=.004E-3
      RETURN
   10 COILR=SEVAL(24,F,FREQ,RCOIL,BR,CR,DR)*1.E-3
      RETURN
      END
      REAL FUNCTION SEVAL(N,U,X,Y,B,C,D)
C
C   COPIED SUBPROGRAM SEVAL FOLLOWS - EVALUATES SPLINE
C
      REAL U,X(N),Y(N),B(N),C(N),D(N)
      DATA I/1/
      IF(I.GE.N) I=1
      IF(U.LT.X(I)) GOTO 10
      IF(U.LE.X(I+1)) GOTO 30
   10 I=1
      J=N+1
   20 K=(I+J)/2
      IF(U.LT.X(K)) J=K
      IF(U.GE.X(K)) I=K
      IF(J.GT.I+1) GOTO 20
   30 DX=U-X(I)
      SEVAL=Y(I)+DX*(B(I)+DX*(C(I)+DX*D(I)))
      RETURN
      END
      FUNCTION COILL(W)
C
C   SUBPROGRAM TO EVALUATE COIL INDUCTANCE COILL AS A FUNCTION OF THE
C    RADIAN FREQUENCY W
C
      REAL FREQ(16),LCOIL(16),BL(16),CL(16),DL(16)
      DATA PI/3.141593/,IFLAG/1/
      IF (IFLAG.NE.1) GOTO 5
C   READ IN COEFFICIENTS FROM FILE LCOIL COEFF FOR SPLINE FUNCTION
C    INTERPOLATION
      DO 1 I=1,16
    1 READ(3,100) FREQ(I),LCOIL(I),BL(I),CL(I),DL(I)
  100 FORMAT(F6.0,4(1X,E15.6))
      TWOPI=2.*PI
      IFLAG=-1
    5 F=W/TWOPI
      IF (F.GT.10.) GOTO 10
      COILL=17.865E-6
      RETURN
   10 IF(F.GE.70.E3) GOTO 20
      COILL=SEVAL(16,F,FREQ,LCOIL,BL,CL,DL)*1.E-6
      RETURN
   20 COILL=9.263E-6
      RETURN
      END
```

```
      SUBROUTINE FFT(KODE,N,DELTA,X,*)
C
C    PROGRAM TO IMPLEMENT THE FAST FOURIER TRANSFORM WHEN THE NUMBER OF
C     DATA POINTS IS AN INTEGER POWER OF TWO.  TAKEN FROM PAGES 264-265
C     OF "METHODS OF DISCRETE SIGNAL AND SYSTEM ANALYSIS", BY JONG.
C
      COMPLEX X(N),W,X1,CMPLX
      IR=0
      N1=N
    5 N2=N1/2
      IF(N2*2.NE.N1) GOTO 100
      IR=IR+1
      N1=N2
      IF(N1.GT.1)GOTO 5
      PN=6.283185/N
      L=N/2
      IR1=IR-1
      K1=0
      DO 30 IS=1,IR
   15 DO 20 I=1,L
      K=K1+1
      KPL=K+L
      AM=KBITR(K1/2**IR1,IR)
      IF(AM.NE.0.) GOTO 18
      X1=X(KPL)
      GOTO 19
   18 ARG=AM*PN
      C=COS(ARG)
      S=-KODE*SIN(ARG)
      W=CMPLX(C,S)
      X1=W*X(KPL)
   19 X(KPL)=X(K)-X1
      X(K)=X(K)+X1
   20 K1=K1+1
      K1=K1+L
      IF(K1.LT.N) GOTO 15
      K1=0
      IR1=IR1-1
   30 L=L/2
      DO 40 K=1,N
      K1=KBITR(K-1,IR)+1
      IF(K1.LE.K) GOTO 40
      X1=X(K)
      X(K)=X(K1)
      X(K1)=X1
   40 CONTINUE
      IF(DELTA.EQ.1.) RETURN
      DO 50 K=1,N
   50 X(K)=DELTA*X(K)
      RETURN
  100 WRITE(6,101) N
  101 FORMAT(//,' *** N= ',I6,' IS NOT A POWER OF 2, FFT RUN ABORTED ***
     1')
      RETURN
      END
      FUNCTION KBITR(K,IR)
C
      KBITR=0
      K1=K
      DO 1 I=1,IR
      K2=K1/2
      KBITR=2*KBITR+K1-2*K2
    1 K1=K2
      RETURN
      END
```

APPENDIX C

CALCULATION OF $K'(\lambda)$

The function we have called $K'(\lambda)$ arises from the transformation of real space current discs into Hankel space. By definition,

$$K'(\lambda) = \frac{30}{3(R_2 - R_1)} \int_{R_1}^{R_2} x \, J_1(\lambda x) \, dx \tag{1}$$

Straightforward quadrature of (1) using the Newton-Cotes algorithm QUANC8 was initially performed for generating values of $K'(\lambda)$ for use in approximating $K'(\lambda)$ with a cubic spline function. This provided sufficient accuracy for use in numerical calculation of coil impedance, as described in Section 6.2. Attempts at calculating the radial magnetic induction using this spline function approximation for $K'(\lambda)$ were a total failure. This appendix describes a procedure for calculating the function $K'(\lambda)$ that is accurate to 14 digits when implemented in double precision FORTRAN on an IBM 370.

The integral in (1) can be evaluated in closed form in terms of named special functions. Change variables,

$$\lambda x = y \quad \Rightarrow \quad dx = dy/\lambda$$

$$x = R_1 \quad \Rightarrow \quad y = \lambda R_1$$

$$x = R_2 \quad \Rightarrow \quad y = \lambda R_2$$

so that (1) becomes

$$K'(\lambda) = \frac{10}{R_2 - R_1} \int_{\lambda R_1}^{\lambda R_2} \frac{y}{\lambda} J_1(y) \frac{dy}{\lambda}$$

$$K'(\lambda) = \frac{10}{R_2 - R_1} \frac{1}{\lambda^2} \int_{\lambda R_1}^{\lambda R_2} y J_1(y)\, dy \qquad (2)$$

From reference [18],

$$\int J_1(y)\, y\, dy = \frac{\pi y}{2}\left[J_1(y) H_0(y) - H_1(y) J_0(y)\right]$$

where $H_0(x)$ and $H_1(x)$ are Struve functions of orders 0 and 1 respectively [18], [19], and $J_0(x)$ and $J_1(x)$ are Bessel functions of the first kind of orders 0 and 1 respectively. Using this result in (2) yields

$$K'(\lambda) = \frac{5\pi y}{\lambda^2 (R_2 - R_1)}\left[J_1(y) H_0(y) - H_1(y) J_0(y)\right]\Bigg|_{y=\lambda R_1}^{\lambda R_2} \qquad (3)$$

In order to use this result, double precision algorithms for generating the Bessel and Struve functions must be available. Double precision Bessel functions are readily available, but Struve functions are not. A computer search of the literature resulted in a reference to a Naval Research Laboratory report that contained FORTRAN source code for generating integer order Struve functions with positive arguments [36]. We were unable to make use of this code because it used subroutines to which we did not have access.

For several years, mathematicians have been aware of the desirability of using truncated Jacobi series of Chebyshev polynomials for numerical approximation of various special functions [37], [38]. Luke [37] provides coefficients b_n and c_n for Chebyshev series expansions

$$H_0(x) = \frac{x}{8} \sum_{n=0}^{\infty} b_n T_{2n}\left(\frac{x}{8}\right), \qquad |x| \le 8$$

$$H_1(x) = \sum_{n=0}^{\infty} c_n T_{2n}\left(\frac{x}{8}\right), \qquad |x| \le 8$$

where $T_{2n}(x)$ is a Chebyshev polynomial of the first kind of order 2n. All coefficients having magnitudes greater than 10^{-20} are given, allowing generation of $H_0(x)$ and $H_1(x)$ with 20 decimal digit accuracy for arguments whose magnitude is less than 8 [39]. Using the identity

$$T_{2n}(x) = T_n(2x^2-1)$$

and retaining sufficient terms for 15 digit accuracy, these series expansions become

$$H_0(x) \doteq \frac{x}{8}\sum_{n=0}^{14} b_n T_n\left[2\left(\frac{x}{8}\right)^2-1\right] \quad , \qquad |x| \le 8 \tag{4}$$

$$H_1(x) \doteq \sum_{n=0}^{14} c_n T_n\left[2\left(\frac{x}{8}\right)^2-1\right] \quad , \qquad |x| \le 8 \tag{5}$$

Then for arguments λ such that $\lambda R_1 < 8$, the expression on the right hand side of (3) is evaluated using (4) and (5). Chebyshev polynomials are evaluated in double precision arithmetic using the subroutine DCNPS from the NASA Lewis Research Analysis Center Software Library [40].

Luke also lists coefficients d_n and e_n for the series

$$H_0(x) - Y_0(x) \doteq \frac{2}{\pi x}\sum_{n=0}^{19} d_n T_{2n}\left(\frac{8}{x}\right) , \qquad x \ge 8$$

$$H_1(x) - Y_1(x) \doteq \frac{2}{\pi}\sum_{n=0}^{16} e_n T_{2n}\left(\frac{8}{x}\right) , \qquad x \ge 8$$

for 15 digit accuracy. The functions $Y_0(x)$ and $Y_1(x)$ are Bessel functions of the second kind of orders 0 and 1 respectively. Rather than use these series directly to evaluate $H_0(x)$ and $H_1(x)$ for arguments greater than 8, some simplification is possible. Writing

$$H_0(x) \doteq \frac{2}{\pi x}\sum_{n=0}^{19} d_n T_{2n}\left(\frac{8}{x}\right) + Y_0(x) \triangleq A_0(x) + Y_0(x)$$

$$H_1(x) \doteq \frac{2}{\pi} \sum_{n=0}^{16} e_n T_{2n}\left(\frac{8}{x}\right) + Y_1(x) \triangleq A_1(x) + Y_1(x)$$

and substituting these expressions for $H_0(x)$ and $H_1(x)$ into the expression $J_1(x)H_0(x)-H_1(x)J_0(x)$ appearing in (3), and suppressing the argument x, we have

$$\begin{aligned} J_1 H_0 - H_1 J_0 = J_1[A_0+Y_0] - [A_1+Y_1]J_0 & \\ &= J_1 A_0 - A_1 J_0 + J_1 Y_0 - Y_1 J_0 \\ &= J_1 A_0 - A_1 J_0 + \frac{2}{\pi x} \end{aligned}$$

using a well known property of the Wronskian of Bessel functions of the first and second kinds [18]. Thus, the expression on the right hand side of (3) can be written as

$$\frac{5\pi y}{\lambda^2(R_2-R_1)}\left[J_1(y)\,A_0(y) - A_1(y)\,J_0(y) + \frac{2}{\pi y}\right]$$

when it is to be evaluated at an argument $y = \lambda R_n > 8$.

Using these results, $K'(\lambda)$ can be evaluated from (3) for non-negative values of the argument to at least 14 digit accuracy.

APPENDIX D

FORTRAN SOURCE CODE FOR CALCULATING RADIAL TIME DOMAIN MAGNETIC INDUCTION ON THE COIL SIDE SURFACE OF THE TARGET

```
C   FILE:  WAUG2 FORTRAN                V1.3
C
C   PROGRAM TO CALCULATE THE RADIAL COMPONENT OF THE MAGNETIC INDUCTION
C    AT THE COIL SIDE FACE OF THE SKIN, AT A RADIAL DISTANCE RINCH
C    FROM THE COIL AXIS.  ADAPTED FROM SOURCE.AUG2 V1.0 BROUGHT TO WSU
C    FROM NASA LEWIS AUGUST 85.
C
C        *****      CAUTION      *****
C
C    DARRAY SHOULD HAVE DIMENSION NARRAY, AND DHINTL SHOULD HAVE
C    DIMENSION NINTL.  IN THE FUNCTIONS DFCT(I) AND DFUN(DX), DARRAY
C    SHOULD HAVE DIMENSION NARRAY.  NARRAY+1=NINTL
C    IN ADDITION, THE ARRAY IERFLG SHOULD BE DIMENSIONED AS
C      IERFLG(2,77,NARRAY).
C
C        *****      CAUTION      *****
C
C   V1.1   -   ADDED THE ABILITY TO STORE AND PRINT THE FLAGS ASSOCIATED
C              WITH EACH INDIVIDUAL GAUSSIAN QUADRATURE.
C   V1.2   -   CHANGED ABSOLUTE AND RELATIVE ERROR REQUESTS TO 1.D-12 IN
C              INVERSE HANKEL TRANSFORM QUADRATURE.
C              CHANGED PRINT FORMATS TO ALLOW SPOOLING OUTPUT TO MY READER.
C   V1.3   -   ADDED OUTER LOOPING ABILITY TO CALCULATE MAGNETIC INTENSITY
C              AT SEVERAL RADII.
C
      IMPLICIT REAL*8 (D)
      COMPLEX CURR(77),CURNT,CFHR(1024),CMUO/(12.56637E-7,0.)/
      REAL*8 DARRAY(100),DHINTL(101),DHRRO(77),DHIRO(77)
      REAL*4 DELTA
      REAL MONTH/'JAN '/,DAY/' 14 '/,VERS/'V1.3'/
      REAL OMEGA(77),HRRO(77),HIRO(77),HRSB(77),HRSC(77),
     *HRSD(77),HISB(77),HISC(77),HISD(77),RINCH/.01/
      INTEGER IERFLG(2,77,100)
      DATA NARRAY/100/,NINTL/101/
      EXTERNAL DFUN,DFCT
      COMMON DARRAY,CURNT,IFUN,R,TWOPIF
C
C   BLOCK 1   -   READ COIL CURRENT SPECTRUM (STEP T) (POSITIVE FREQUENCIES
C                 ONLY) FROM FILE CURRSPEC DATA (LOGICAL DEVICE 5).
C                 FREQUENCIES ARE STORED IN OMEGA(I) WITH THE CORRESPONDING
C                 CURRENT SPECTRAL VALUE IN CURR(I).
C
C   READ CURRENT SPECTRUM (HEADINGS HAVE BEEN REMOVED FROM THE FILE
C    CURRSPEC DATA)
      DO 10 I=1,77
   10 READ (5,1000) OMEGA(I),CURR(I)
 1000 FORMAT(T19,E12.5,T36,E13.5,T51,E13.5)
C
C   OUTER LOOP TO CONTROL RADIUS AT WHICH MAGNETIC INDUCTION IS
C    CALCULATED
C
C     DO 30 IRADUS=16,20,2
C     RINCH=FLOAT(IRADUS)/10.
C   EXPRESS R IN METERS
      R=RINCH*.0254
C
C   BLOCK 2   -   CALCULATE INVERSE HANKEL TRANSFORM OF THE MAGNETIC
C                 INTENSITY.  THIS IS DONE AT EACH OF THE DIFFERENT
C                 FREQUENCIES OMEGA(I), I=1,2,....,77.  THE FREQUENCY
C                 OMEGA IS PASSED TO THE SUBPROGRAM FUN THRU THE COMMON
C                 VARIABLE TWOPIF.  THE COMPLEX VALUE OF THE CURRENT
C                 SPECTRUM AT THIS FREQUENCY IS PASSED TO FUN THRU THE
C                 COMMON VARIABLE CURNT.
C
C   CALCULATE THE REAL*8 ARRAY OF UPPER AND LOWER INTEGRATION LIMITS
C    USED IN FORMING THE SEQUENCE OF MAGNETIC INTENSITIES.
      DSTEP=10.D0
      DO 1 I=1,NINTL
    1 DHINTL(I)=DFLOAT(I-1)*DSTEP
```

```
C   PRINT HEADINGS
        WRITE(6,9000) VERS,MONTH,DAY,DHINTL(NINTL)
 9000 FORMAT('  1OUTPUT FROM WAUG2 FORTRAN ',A4,10X,A4,A4,/,'  UPPER INVE
     *RSE HANKEL TRANSFORM INTEGRATION LIMIT = ',D13.5//)
        WRITE(6,9001) RINCH,RINCH
 9001 FORMAT('  FREQUENCY  REAL PART OF MAGNETIC INTENSITY',T57,'IMAG PA
     *RT OF MAGNETIC INTENSITY',/,'    (HERTZ)',T20,'H(R=',F3.1,',F)',T38
     *,'IER   N',T63,'H(R=',F3.1,',F)',T81,'IER   N')
C   BEGINNING OF MAIN LOOP TO CALCULATE INVERSE HANKEL TRANSFORM AT 77
C    DIFFERENT FREQUENCIES
        DO 900 IMAIN=1,77
        TWOPIF=OMEGA(IMAIN)
        CURNT=CURR(IMAIN)
C   CALCULATE REAL PART OF HR(R,TWOPIF)
        IFUN=1
C   FORM THE SEQUENCE OF PARTIAL INVERSE HANKEL TRANSFORMS BY INTEGRATING
C    BETWEEN LAMBDA SUB(I) AND LAMBDA SUB(I+1), FOR I=1 TO NARRAY (THESE
C    LIMITS ARE IN THE ARRAY DHINTL).
C   SET UP ABSOLUTE AND RELATIVE QUADRATURE ERROR REQUESTS
        DABSER=1.D-12
        DRER=1.D-12
C   INITIALIZE THE VARIABLE USED TO ACCUMULATE THE RESULTS OF THE
C    NUMERICAL INTEGRATION OVER EACH LAMBDA SUB-RANGE.
        DINTR=0.D0
        DO 2 I=1,NARRAY
C   FORM THE LOWER AND UPPER INTEGRATION LIMITS
        DA=DHINTL(I)
        DB=DHINTL(I+1)
C   INTEGRATE (THESE VALUES ARE PASSED TO THE FUNCTION DFCT THRU COMMON).
C    RESULT OF THE INTEGRATION IS STORED IN DARRAY(I) FOR FUTURE USE IN
C    THE EULER CONVERGENCE ACCELERATION ALGORITHM DTEUL.
        CALL QGAUSS(DA,DB,DFUN,DRER,DABSER,DARRAY(I),DERR,IER)
C   STORE ERROR FLAG
        IERFLG(1,IMAIN,I)=IER
C   NOW SUM THE INTEGRALS FOR COMPARISION WITH THE ACCELERATED SUM TO
C    BE CALCULATED IN SUBROUTINE DTEUL.
      2 DINTR=DINTR+DARRAY(I)
C   NOW USE THE EULER CONVERGENCE ACCELERATION ROUTINE TO BEST ESTIMATE
C    THE REAL PART OF THE TOTAL INVERSE HANKEL TRANSFORM AT THE
C    FREQUENCY TWOPIF.
        CALL DTEUL(DFCT,DSUMR,NARRAY,1.E-14,IERR,NR)
        DHRRO(IMAIN)=DSUMR
        HRRO(IMAIN)=SNGL(DSUMR)
C   CALCULATE IMAGINARY PART OF HR(R,TWOPIF)
        IFUN=2
C   FORM THE SEQUENCE OF PARTIAL INVERSE HANKEL TRANSFORMS BY INTEGRATING
C    BETWEEN LAMBDA SUB(I) AND LAMBDA SUB(I+1), FOR I=1 TO NARRAY (THESE
C    LIMITS ARE IN THE ARRAY DHINTL).
C   INITIALIZE THE VARIABLE USED TO ACCUMULATE THE RESULTS OF THE
C    NUMERICAL INTEGRATION OVER EACH LAMBDA SUB-RANGE.
        DINTI=0.D0
        DO 3 I=1,NARRAY
C   FORM THE LOWER AND UPPER INTEGRATION LIMITS
        DA=DHINTL(I)
        DB=DHINTL(I+1)
C   INTEGRATE (THESE VALUES ARE PASSED TO THE FUNCTION DFCT THRU COMMON).
C    RESULT OF THE INTEGRATION IS STORED IN DARRAY(I) FOR FUTURE USE IN
C    THE EULER CONVERGENCE ACCELERATION ALGORITHM DTEUL.
        CALL QGAUSS(DA,DB,DFUN,DRER,DABSER,DARRAY(I),DERR,IER)
C   STORE ERROR FLAG
        IERFLG(2,IMAIN,I)=IER
C   NOW SUM THE INTEGRALS FOR COMPARISION WITH THE ACCELERATED SUM TO
C    BE CALCULATED IN SUBROUTINE DTEUL.
      3 DINTI=DINTI+DARRAY(I)
C   NOW USE THE EULER CONVERGENCE ACCELERATION ROUTINE TO BEST ESTIMATE
C    THE REAL PART OF THE TOTAL INVERSE HANKEL TRANSFORM AT THE
C    FREQUENCY TWOPIF.
        CALL DTEUL(DFCT,DSUMI,NARRAY,1.E-14,IERI,NI)
        DHIRO(IMAIN)=DSUMI
        HIRO(IMAIN)=SNGL(DSUMI)
        F=OMEGA(IMAIN)/6.283185
  900 WRITE(6,9010) F,DHRRO(IMAIN),IERR,NR,DHIRO(IMAIN),IERI,NI,DINTR,
     *DINTI
 9010 FORMAT(T4,F7.0,T14,2(D23.16,2X,I1,2X,I3,12X),/,T10,'SUM=',D23.16,
     *T53,'SUM=',D23.16,/)
C   END OF DEVELOPMENT STAGE CODE
C
C   BLOCK 3  -   FORM HR(R,N*DELTAW) NEEDED FOR IDFT.  USE SPLINE FUNCTION
C                INTERPOLATION ON THE RESULTS OF BLOCK 2.
C
        NSPL=77
C   FORM SPLINE COEFFICIENTS FOR THE REAL PART OF HR(R,O)
        CALL SPLINE(NSPL,OMEGA,HRRO,HRSB,HRSC,HRSD)
```

```
C   FORM SPLINE COEFFICIENTS FOR THE IMAGINARY PART OF HR(R,O)
      CALL SPLINE(NSPL,OMEGA,HIRO,HISB,HISC,HISD)
C   SET UP PARAMETERS FOR USE IN IDFT CALCULATIONS
      TSAMP=5.E-6
      NDFT=1024
      TWOPI=2.*3.141593
      WO=TWOPI/(TSAMP*NDFT)
      ISTOP=NDFT/2+1
C   FORM THE SPECTRUM OF THE FIRST (N/2+1) FREQUENCIES
      DO 40 I=1,ISTOP
      RADFRQ=WO*FLOAT(I-1)
   40 CFHR(I)=CMPLX(SEVALR(NSPL,RADFRQ,OMEGA,HRRO,HRSB,HRSC,HRSD),SEVALI
     *(NSPL,RADFRQ,OMEGA,HIRO,HISB,HISC,HISD))
C   NOW FORM THE CONJUGATE PART OF THE SPECTRUM
      ISTART=ISTOP+1
      DO 50 I=ISTART,NDFT
   50 CFHR(I)=CONJG(CFHR(NDFT+2-I))
C
C   BLOCK 4  -  CALCULATE THE INVERSE FOURIER TRANSFORM OF THE MAGNETIC
C               INTENSITY.  USES AN IDFT TO SIMPLIFY THE NUMERICAL
C               PROCEDURE.
C
      DELTA=1./(TSAMP*FLOAT(NDFT))
      KODE=-1
      CALL FFT(KODE,NDFT,DELTA,CFHR,&60)
C   PRINT RESULTS - TIME DOMAIN MAGNETIC INTENSITY
      WRITE(6,2000)
 2000 FORMAT(//'  TIME(MILLISEC)   INDUCTION (TESLA)')
      DO 70 I=1,201
      TIME=.005*FLOAT(I-1)
      CFHR(I)=CFHR(I)*CMUO
   70 WRITE(6,2010) TIME,CFHR(I)
 2010 FORMAT(4X,F8.3,T22,F8.5,T41,E11.4)
      DO 80 I=226,1001,5
      TIME=.005*FLOAT(I-1)
      CFHR(I)=CFHR(I)*CMUO
   80 WRITE(6,2010) TIME,CFHR(I)
C   PRINT ERROR FLAGS
      WRITE(6,4500)
 4500 FORMAT(' 1ERROR FLAGS FROM REAL INTEGRATION:'/)
      DO 216 I=1,NARRAY
  216 WRITE(6,4501) (IERFLG(1,II,I),II=1,77)
 4501 FORMAT(2X,77(I1))
      WRITE(6,4502)
 4502 FORMAT(' 1ERROR FLAGS FROM IMAG INTEGRATION:'/)
      DO 217 I=1,NARRAY
  217 WRITE(6,4501) (IERFLG(2,II,I),II=1,77)
C   99 CONTINUE
   60 STOP
      END
      REAL FUNCTION SEVALR(N,U,X,Y,B,C,D)
C   COPIED SUBPROGRAM SEVAL FOLLOWS
      REAL U,X(N),Y(N),B(N),C(N),D(N)
      DATA I/1/
      IF(I.GE.N) I=1
      IF(U.LT.X(I)) GOTO 10
      IF(U.LE.X(I+1)) GOTO 30
   10 I=1
      J=N+1
   20 K=(I+J)/2
      IF(U.LT.X(K)) J=K
      IF(U.GE.X(K)) I=K
      IF(J.GT.I+1) GOTO 20
   30 DX=U-X(I)
      SEVALR=Y(I)+DX*(B(I)+DX*(C(I)+DX*D(I)))
      RETURN
      END
      REAL FUNCTION SEVALI(N,U,X,Y,B,C,D)
C   COPIED SUBPROGRAM SEVAL FOLLOWS
      REAL U,X(N),Y(N),B(N),C(N),D(N)
      DATA I/1/
      IF(I.GE.N) I=1
      IF(U.LT.X(I)) GOTO 10
      IF(U.LE.X(I+1)) GOTO 30
   10 I=1
      J=N+1
   20 K=(I+J)/2
      IF(U.LT.X(K)) J=K
      IF(U.GE.X(K)) I=K
      IF(J.GT.I+1) GOTO 20
   30 DX=U-X(I)
      SEVALI=Y(I)+DX*(B(I)+DX*(C(I)+DX*D(I)))
      RETURN
      END
```

```
      SUBROUTINE SPLINE(N,X,Y,B,C,D)
C   COPIED SUBROUTINE SPLINE FOLLOWS
      INTEGER N
      REAL X(N),Y(N),B(N),C(N),D(N)
      INTEGER NM1, IB, I
      REAL T
      NM1=N-1
      IF(N.LT.2)RETURN
      IF(N.LT.3)GO TO 50
      D(1)=X(2)-X(1)
      C(2)=(Y(2)-Y(1))/D(1)
      DO 10 I = 2, NM1
         D(I) = X(I+1)-X(I)
         B(I) = 2.*(D(I-1)+D(I))
         C(I+1) = (Y(I+1)-Y(I))/D(I)
         C(I) = C(I+1)-C(I)
   10 CONTINUE
      B(1)=-D(1)
      B(N)=-D(N-1)
      C(1)=0.
      C(N)=0.
      IF(N.EQ.3) GO TO 15
      C(1)=C(3)/(X(4)-X(2)) - C(2)/(X(3)-X(1))
      C(N)=C(N-1)/(X(N)-X(N-2)) - C(N-2)/(X(N-1)-X(N-3))
      C(1)=C(1)*D(1)**2/(X(4)-X(1))
      C(N)=-C(N)*D(N-1)**2/(X(N)-X(N-3))
   15 DO 20 I = 2, N
         T=D(I-1)/B(I-1)
         B(I)=B(I)-T*D(I-1)
         C(I)=C(I)-T*C(I-1)
   20 CONTINUE
      C(N)=C(N)/B(N)
      DO 30 IB= 1, NM1
         I=N-IB
         C(I)=(C(I)-D(I)*C(I+1))/B(I)
   30 CONTINUE
      B(N) = (Y(N)-Y(NM1))/D(NM1) + D(NM1)*(C(NM1) + 2.*C(N))
      DO 40 I = 1, NM1
         B(I) = (Y(I+1)-Y(I))/D(I) - D(I)*(C(I+1)+2.*C(I))
         D(I) = (C(I+1)-C(I))/D(I)
         C(I)=3.*C(I)
   40 CONTINUE
      C(N)=3.*C(N)
      D(N)=D(N-1)
      RETURN
   50 B(1)=(Y(2)-Y(1))/(X(2)-X(1))
      C(1)=0.
      D(1)=0.
      B(2)=B(1)
      C(2)=0.
      D(2)=0.
      RETURN
      END
      SUBROUTINE FFT(KODE,N,DELTA,X,*)
C   FILE:  FFT FORTRAN
C   PROGRAM TO IMPLEMENT THE FAST FOURIER TRANSFORM WHEN THE NUMBER OF
C    DATA POINTS IS AN INTEGER POWER OF TWO.  TAKEN FROM PAGES 264-265
C    OF "METHODS OF DISCRETE SIGNAL AND SYSTEM ANALYSIS", BY JONG.
C
      COMPLEX X(N),W,X1,CMPLX
      IR=0
      N1=N
    5 N2=N1/2
      IF(N2*2.NE.N1) GOTO 100
      IR=IR+1
      N1=N2
      IF(N1.GT.1)GOTO 5
      PN=6.283185/N
      L=N/2
      IR1=IR-1
      K1=0
      DO 30 IS=1,IR
   15 DO 20 I=1,L
      K=K1+1
      KPL=K+L
      AM=KBITR(K1/2**IR1,IR)
      IF(AM.NE.0.) GOTO 18
      X1=X(KPL)
      GOTO 19
   18 ARG=AM*PN
      C=COS(ARG)
      S=-KODE*SIN(ARG)
      W=CMPLX(C,S)
      X1=W*X(KPL)
```

```
10  X(KPL)=X(K)-X1
    X(K)=X(K)+X1
20  K1=K1+1
    K1=K1+L
    IF(K1.LT.N) GOTO 15
    K1=0
    IR1=IR1-1
30  L=L/2
    DO 40 K=1,N
    K1=KBITR(K-1,IR)+1
    IF(K1.LE.K) GOTO 40
    X1=X(K)
    X(K)=X(K1)
    X(K1)=X1
40  CONTINUE
    IF(DELTA.EQ.1.) RETURN
    DO 50 K=1,N
50  X(K)=DELTA*X(K)
    RETURN
100 WRITE(6,101) N
101 FORMAT(//,' *** N= ',I6,' IS NOT A POWER OF 2, FFT RUN ABORTED ***
   1')
    RETURN1
    END
    FUNCTION KBITR(K,IR)
    KBITR=0
    K1=K
    DO 1 I=1,IR
    K2=K1/2
    KBITR=2*KBITR+K1-2*K2
1   K1=K2
    RETURN
    END
    DOUBLE PRECISION FUNCTION DFUN(DX)
C   SUBROUTINE TO FORM THE INTEGRAND IN GAUSSQ.  SINCE GAUSSQ IS USED FOR
C    NUMERICAL QUADRATURE WITH TWO DIFFERENT INTEGRANDS, WHICH INTEGRAND
C    IS EVALUATED BY FUN IS DETERMINED BY THE FLAG IFUN, PASSED TO FUN
C    BY THE MAIN PROGRAM THRU COMMON STORE.
    IMPLICIT COMPLEX*16 (C), REAL*8 (D)
    COMPLEX*16 CD/(.81D-3,0.D0)/,CONE/(1.D0,0.D0)/,CTWO/(2.D0,0.D0)/,
   *DCMPLX
    COMPLEX CURNT
    REAL*8 DMUSIG/21.8654800/,DHD3/1.59D-3/,DG/2.78D-3/,DCOMP(2),
   *DARRAY(100)
    EQUIVALENCE (CHR,DCOMP(1))
    COMMON DARRAY,CURNT,IFUN,R,TWOPIF
C   FORM COMPLEX*16 VERSION OF THE COMPLEX*8 CURRENT PASSED TO IFUN THRU
C    THE COMMON VARIABLE CURNT
    CURNTD=DCMPLX(DBLE(REAL(CURNT)),DBLE(AIMAG(CURNT)))
    IF(DX .NE. 0.D0) GOTO 10
C   LAMBDA=0: INTEGRAND=0
    DFUN=0.D0
    RETURN
C   EVALUATE THE NUMERATOR (WITHOUT THE KERNEL)
10  DT1=DEXP(-DX*DHD3)
    DT2=((DT1+1.D0)*DT1+1.D0)*DEXP(-DX*DG)*DKPRLK(DX)
C   IF FREQUENCY=0, ALMOST DONE
    IF(TWOPIF .NE. 0.) GOTO 20
C   FREQUENCY IS ZERO
    CHR=DCMPLX(DT2/2.D0,0.D0)*CURNTD
    GOTO 30
C   NEITHER LAMBDA NOR FREQUENCY IS ZERO
20  CSQ=CDSQRT(DCMPLX(DX*DX,DBLE(TWOPIF)*DMUSIG))
    CT=CDEXP(CD*CSQ)
    CTI=CONE/CT
    CCOSH=(CT+CTI)/CTWO
    CSINH=CCOSH-CTI
    CRATIO=DCMPLX(DX,0.D0)/CSQ
    CDENOM=CONE+(CCOSH+CRATIO*CSINH)/(CSINH/CRATIO+CCOSH)
    CHR=DCMPLX(DT2,0.D0)*CURNTD/CDENOM
C   NOW CALCULATE INTEGRAND
30  DRTL=DX*DBLE(R)
    DJ1=DJ1LK(DRTL)
    IF(IFUN .EQ. 1) DFUN=DCOMP(1)*DJ1*DX
    IF(IFUN .EQ. 2) DFUN=DCOMP(2)*DJ1*DX
    RETURN
    END
```

```
      DOUBLE PRECISION FUNCTION DKPRLK(DLMBDA)
C     SUBPROGRAM TO EVALUATE THE FUNCTION KPRIME(LAMBDA).  THE ARGUMENT
C      DLMBDA MUST BE REAL*8.  USES THE RESULT THAT THE ANTIDERIVATIVE
C      OF    J1(X) * X    IS EQUAL TO
C               PI * X * (J1(X) * HO(X) - H1(X) * JO(X)) / 2
C      FOR ARGUMENTS DLMBDA*RX .LE. 8, THE DIFFERENCE IS EVALUATED
C      DIRECTLY.   FOR DLMBDA*RX .GT. 8, SOME SIMPLIFICATION IS
C      UTILIZED (SEE THE PAPER DATED JULY 23).
C      REF:  "HIGHER TRANSCENDENTAL FUNCTIONS", VOL. 2, P. 89,
C            EQUATION (5) WITH NU=1
C      REQUIRES FUNCTION SUBPROGRAMS DHOLK(DX), DHILK(DX),DAOSM(DX),
C      DAISM(DX), AND THE REAL*8 IMSL SUBROUTINE MMBSJN.
C      MODIFIED SEPT 19 85 AT WSU TO REPLACE MMBSJN WITH MY E.P. FUNCTIONS
C      DJOLK AND DJILK.
C
      IMPLICIT REAL*8 (D)
      REAL*8 DPI/3.14159265358979/,DR1/.003175D0/,DR2/.0254D0/,DJU(2),  -
     *DJL(2)
      DATA IFLAG/-1/
C     CHECK TO SEE IF ROUTINE HAS BEEN CALLED BEFORE
      IF (IFLAG .NE. -1) GOTO 10
C     NO PREVIOUS CALL - PERFORM INITIALIZATION
      DCONST=5.D0*DPI/(DR2-DR1)
C     RESET FLAG SO INITIALIZATION WON'T BE PERFORMED AGAIN
      IFLAG=-1
C
C     CALCULATE KPRIME(LAMBDA)
C
   10 DKPRLK=0.D0
C     CHECK TO SEE IF ARGUMENT = 0
      IF(DLMBDA .EQ. 0.D0) RETURN
C     BEGIN BY FORMING UPPER AND LOWER INTEGRATION LIMITS
      DU=DR2*DLMBDA
      DL=DR1*DLMBDA
C     FORM BESSEL FUNCTIONS OF THE FIRST KIND AT THE UPPER AND LOWER
C      INTEGRATION LIMITS
      DJU(1)=DJOLK(DU)
      DJU(2)=DJILK(DU)
      DJL(1)=DJOLK(DL)
      DJL(2)=DJILK(DL)
C     FORM DIFFERENCE AT THE UPPER INTEGRATION LIMIT
C     DECIDE WHICH TECHNIQUE TO USE TO EVALUATE J1(DU)*HO(DU)-H1(DU)*JO(DU)
      IF (DU .GT. 8.D0) GOTO 20
      DIFFU=DJU(2)*DHOLK(DU)-DHILK(DU)*DJU(1)
      GOTO 30
   20 DIFFU=DJU(2)*DAOSM(DU)-DAISM(DU)*DJU(1) + 2.D0/(DPI*DU)
C     FORM DIFFERENCE AT THE LOWER INTEGRATION LIMIT
C     DECIDE WHICH TECHNIQUE TO USE TO EVALUATE J1(DL)*HO(DL)-H1(DL)*JO(DL)
   30 IF (DL .GT. 8.D0) GOTO 40
      DIFFL=DJL(2)*DHOLK(DL)-DHILK(DL)*DJL(1)
      GOTO 50
   40 DIFFL=DJL(2)*DAOSM(DL)-DAISM(DL)*DJL(1) + 2.D0/(DPI*DL)
C     EVALUATE KPRIME
   50 DKPRLK=DCONST*(DR2*DIFFU-DR1*DIFFL)/DLMBDA
      RETURN
      END
      FUNCTION DHOLK(DX)
C     DOUBLE PRECISION SUBPROGRAM TO EVALUATE THE STRUVE FUNCTION OF
C      ORDER ZERO FOR DOUBLE PRECISION ARGUMENTS  DX .LE. 8  USING A
C      SUMMATION OF WEIGHTED CHEBYSHEV POLYNOMIALS.
C      REQUIRES THE SUBROUTINE DCNPS (NASA LEWIS COMPUTER LIBRARY) TO
C      FORM AND SUM THE POLYNOMIALS.
C      REF:  "THE SPECIAL FUNCTIONS AND THEIR APPROXIMATIONS",
C            VOL. 2, P. 370, BY YUDELL LUKE.
C
      IMPLICIT REAL*8 (D)
      REAL*8 B(15)/1.00215845609712,-1.63969292681309,1.50236939618293, -
     *-.724951153021218,.189553273710931,-.0306705202298 4,             -
     *337.561447375194D -5,-26.955014312602D-5,1.6374616926123D-5,      -
     *-7824.4408508254D-10,302.1593188153D-10,-9.632664495D-10,         -
     *.25779337089D-10,-589.53949D-15,11.58332D-15/
C     CHECK FOR ARGUMENT OUT OF RANGE
      IF(DABS(DX) .GT. 8.D0) RETURN
C     FORM THE ARGUMENT FOR THE CHEBYSHEV POLYNOMIALS
      DXD8=DX/8.D0
      DARG=2.D0*DXD8*DXD8-1.D0
C     SUM THE POLYNOMIALS
      CALL DCNPS(DHOLK,DARG,B,15,99)
C     COMPLETE THE EVALUATION AND RETURN
      DHOLK=DHOLK*DXD8
   99 RETURN
      END
```

```
      SUBROUTINE DCNPS(Y,X,C,N,*)
C
      DIMENSION C(N)
      DOUBLE PRECISION C,Y,X,H0,H1,H2,ARG
C
C        TEST OF DIMENSION
      IF(DABS(X) .GT. 1.D0)RETURN1
      IF(N)1,1,2
    1 RETURN
C
    2 IF(N-2)3,4,4
    3 Y=C(1)
      RETURN
C
C        INITIALIZATION
    4 ARG=X+X
      H1=0.D0
      H0=0.D0
C
      DO 5 I=1,N
      K=N-I
      H2=H1
      H1=H0
    5 H0=ARG*H1-H2+C(K+1)
      Y=0.5D0*(C(1)-H2+H0)
      RETURN
      END
      FUNCTION DH1LK(DX)
C   DOUBLE PRECISION SUBPROGRAM TO EVALUATE THE STRUVE FUNCTION OF
C    ORDER ONE FOR DOUBLE PRECISION ARGUMENTS  DX .LE. 8  USING A
C    SUMMATION OF WEIGHTED CHEBYSHEV POLYNOMIALS.
C    REQUIRES THE SUBROUTINE DCNPS (NASA LEWIS COMPUTER LIBRARY) TO
C    FORM AND SUM THE POLYNOMIALS.
C    REF:  "THE SPECIAL FUNCTIONS AND THEIR APPROXIMATIONS",
C          VOL. 2, P. 370, BY YUDELL LUKE.
C
      IMPLICIT REAL*8 (D)
      REAL*8 C(15)/.55788914464816,-.111883257265698,-.163379581252009, -
     *.322369320724059,-.145816323672442,3292.677399374D-5,              -
     *-460.372142093573D-5,44.3470616331396D-5,-3.14209952934117D-5,     -
     *.171237199380035D-5,-741.6987005204D-10,26.1837670705D-10,         -
     *-.7635839395D-10,1906.70416D-15,-40.52291D-15/
C   CHECK FOR ARGUMENT OUT OF RANGE
      IF(DABS(DX) .GT. 8.D0) RETURN
C   FORM THE ARGUMENT FOR THE CHEBYSHEV POLYNOMIALS
      DXD8=DX/8.D0
      DARG=2.D0*DXD8*DXD8-1.D0
C   SUM THE POLYNOMIALS
      CALL DCNPS(DH1LK,DARG,C,15,99)
   99 RETURN
      END
      FUNCTION DA0SM(DX)
C   DOUBLE PRECISION SUBPROGRAM TO EVALUATE THE SUMMATION ASSOCIATED
C    WITH THE STRUVE FUNCTION OF ORDER ZERO FOR DOUBLE PRECISION ARGU-
C    MENTS DX .GE. 8 USING A SUMMATION OF WEIGHTED CHEBYSHEV POLYNOMIALS.
C    REQUIRES THE SUBROUTINE DCNPS (NASA LEWIS COMPUTER LIBRARY) TO
C    FORM AND SUM THE POLYNOMIALS.
C    REF:  "THE SPECIAL FUNCTIONS AND THEIR APPROXIMATIONS",
C          VOL. 2, P. 371, BY YUDELL LUKE.
C
      IMPLICIT REAL*8 (D)
      REAL*8 D(20)/.992837275764239,-696.891281138625D-5,                -
     *18.2051037870371D-5,-1.06325825284416D-5,9819.3294286525D-10,      -
     *-1223.0645444977D-10,189.40833118D-10,-34.4358225604D-10,          -
     *7.1119101711D-10,-1.6288744137D-10,.4065680728D-10,                -
     *-.1091504796D-10,3120.05243D-15,-942.0207D-15,298.47947D-15,       -
     *-98.72416D-15,33.93712D-15,-12.0798D-15,4.43821D-15,-1.67859D-15/
      REAL*8 DPID2/1.5707963267949/
C   CHECK FOR ARGUMENT OUT OF RANGE
      IF(DABS(DX) .LT. 8.D0) RETURN
C   FORM THE ARGUMENT FOR THE CHEBYSHEV POLYNOMIALS
      D8DX=8.D0/DX
      DARG=2.D0*D8DX*D8DX-1.D0
C   SUM THE POLYNOMIALS
      CALL DCNPS(DA0SM,DARG,D,20,99)
C   COMPLETE THE EVALUATION AND RETURN
      DA0SM=DA0SM/(DPID2*DX)
   99 RETURN
      END
```

```
      FUNCTION DA1SM(DX)
C   DOUBLE PRECISION SUBPROGRAM TO EVALUATE THE SUMMATION ASSOCIATED
C    WITH THE STRUVE FUNCTION OF ORDER ONE FOR DOUBLE PRECISION ARGU-
C    MENTS DX .GE. 8 USING A SUMMATION OF WEIGHTED CHEBYSHEV POLYNOMIALS.
C    REQUIRES THE SUBROUTINE DCNPS (NASA LEWIS COMPUTER LIBRARY) TO
C    FORM AND SUM THE POLYNOMIALS.
C    REF:  "THE SPECIAL FUNCTIONS AND THEIR APPROXIMATIONS",
C          VOL. 2, P. 371, BY YUDELL LUKE.
C
      IMPLICIT REAL*8 (D)
      REAL*8 E(17)/1.00757647293866,750.31605124825T0-5,
     *-7.04393326451905D-5,.266205393382266D-5,-1884.11577534050-10,
     *194.90149583940-10,-26.12619899050-10,4.2362690104D-10,
     *-.79551555310-10,.16799730060-10,-3907.198210-15,985.43090-15,
     *-266.357940-15,76.450350-15,-23.129610-15,7.332120-15,
     *-2.423340-15/
      REAL*8 DPID2/1.5707963267949/
C   CHECK FOR ARGUMENT OUT OF RANGE
      IF(DABS(DX) .LT. 8.DO) RETURN
C   FORM THE ARGUMENT FOR THE CHEBYSHEV POLYNOMIALS
      D8DX=8.DO/DX
      DARG=2.DO*D8DX*D8DX-1.DO
C   SUM THE POLYNOMIALS
      CALL DCNPS(DA1SM,DARG,E,17,99)
C   COMPLETE THE EVALUATION AND RETURN
      DA1SM=DA1SM/DPID2
   99 RETURN
      END
      DOUBLE PRECISION FUNCTION DJ1LK(DX)
C   DOUBLE PRECISION SUBPROGRAM TO EVALUATE THE BESSEL FUNCTION OF THE
C    FIRST KIND OF ORDER 1 AT THE DOUBLE PRECISION ARGUMENT DX.  FOR
C    ARGUMENTS  DABS(DX) .LE. 8  A TRUNCATED JACOBI SERIES OF CHEBYSHEV
C    POLYNOMIALS IS USED (SEE THE FIRST REFERENCE BELOW).  FOR ARGUMENTS
C    DABS(DX) .GT. 8  A TRUNCATED ASYMPTOTIC SERIES IS USED (SEE SECOND
C    REFERENCE BELOW).
C   REQUIRES THE SUBROUTINE DCNPS (NASA LEWIS COMPUTER LIBRARY) TO FORM
C    AND SUM THE CHEBYSHEV POLYNOMIALS.
C   REF:  "THE SPECIAL FUNCTIONS AND THEIR APPROXIMATIONS",
C         VOL. 2, P. 332, BY YUDELL LUKE.
C   REF:  "CHEBYSHEV SERIES FOR MATHEMATICAL FUNCTIONS", NAT. PHYS.
C         LAB. MATH. TABLES, VOL V, P. 33, BY C.W. CLENSHAW.
C
      IMPLICIT REAL*8 (D)
      REAL*8 DB(15)/.648358770605264DO,-1.191801160541220O,
     *1.28739940988576800,-.66144393413454300,.17770911723972800,
     *-2917.55248061542D-5,324.027012683860-5,-26.04443893485810-5,
     *1.38870192399321D-5,-7617.58780540030-10,294.97070072780-10,
     *-9.4242129816D-10,25281.234640-15,-577.740420-15,
     *11.385720-15/
      REAL*8 DP1(15)/2.00187608172003DO,89.89983308534410-5,
     *-39872.34300488910-10,617.753395D6440-10,-18.71890749110-10,
     *88168.986600-15,-5704.363540-15,469.919550-15,-46.842240-15,
     *5.452570-15,-72212.D-20,10668.D-20,-1731.D-20,305.D-20,
     *-58.D-20/
      REAL*8 DQ1(15)/9355.55741390707D-5,-9.627723549157080-5,
     *9138.615257955D-10,-209.537813840BD-10,8.22919332770-10,
     *-46863.536380-15,3515.218790-15,-326.431570-15,35.967770-15,
     *-4.561250-15,55083.D-20,-10269.D-20,1768.D-20,-328.D-20,
     *65.D-20/
      DATA DPI/3.14159265358979/,IFLAG/-1/
C   CHECK TO SEE IF ROUTINE HAS BEEN CALLED BEFORE
      IF(IFLAG .NE. -1) GOTO 5
C   PERFORM INITIALIZATION AND RESET FLAG
      DCONST=DSQRT(2.DO/DPI)
      D3PID4=3.DO*DPI/4.DO
      DP1(1)=DP1(1)/2.DO
      DQ1(1)=DQ1(1)/2.DO
      IFLAG=1
    5 DJ1LK=0.DO
C   CHECK FOR ARGUMENT EQUAL TO ZERO
      IF(DX .EQ. 0.DO) RETURN
C   DECIDE IF JACOBI OR ASYMPTOTIC SERIES WILL BE USED
      IF(DABS(DX) .GT. 8.DO) GOTO 10
C   USE JACOBI SERIES
C   FORM THE ARGUMENT FOR THE CHEBYSHEV POLYNOMIALS
      DXD8=DX/8.DO
      DARG=2.DO*DXD8*DXD8-1.DO
C   SUM THE POLYNOMIALS
      CALL DCNPS(DJ1LK,DARG,DB,15)
C   FINISH THE CALCULATION AND RETURN
      DJ1LK=DXD8*DJ1LK
   99 RETURN
C   USE MODIFIED ASYMPTOTIC SERIES
   10 D8DX=8.DO/DX
      DARG=2.DO*D8DX*D8DX-1.DO
```

```
C   SUM THE POLYNOMIALS FOR P1(X)
       CALL DCNPS(DP,DARG,DP1,15)
C   SUM THE POLYNOMIALS FOR Q1(X)
       CALL DCNPS(DQ,DARG,DQ1,15)
       DQ=DQ*D8DX
C   FORM THE ASYMPTOTIC EXPRESSION
       DJ1LK=(DCONST*(DP*DCOS(DX-D3PID4)-DQ*DSIN(DX-D3PID4)))/DSQRT(DX)
       RETURN
       END
       DOUBLE PRECISION FUNCTION DJ0LK(DX)
C   DOUBLE PRECISION SUBPROGRAM TO EVALUATE THE BESSEL FUNCTION OF THE
C    FIRST KIND OF ORDER 0 AT THE DOUBLE PRECISION ARGUMENT DX.  FOR
C    ARGUMENTS  DABS(DX) .LT. 8  A TRUNCATED JACOBI SERIES OF CHEBYSHEV
C    POLYNOMIALS IS USED (SEE THE FIRST REFERENCE BELOW).  FOR ARGUMENTS
C    DABS(DX) .GE. 8  A TRUNCATED ASYMPTOTIC SERIES IS USED (SEE SECOND
C    AND THIRD REFERENCE BELOW).
C   REQUIRES THE SUBROUTINE DCNPS (NASA LEWIS COMPUTER LIBRARY) TO FORM
C    AND SUM THE CHEBYSHEV POLYNOMIALS.
C   REF:  "THE SPECIAL FUNCTIONS AND THEIR APPROXIMATIONS",
C         VOL. 2, P. 331, BY YUDELL LUKE.
C   REF:  "CHEBYSHEV SERIES FOR MATHEMATICAL FUNCTIONS", NAT. PHYS.
C         LAB. MATH. TABLES, VOL V, P. 32, BY C.W. CLENSHAW.
C
       IMPLICIT REAL*8 (D)
       REAL*8 DB(19)/.15772797147489000,-872.3442352852220-5,
      *.26517861320333600,-.37009499387264900,.15806710233209700,
      *-3489.37694114084D-5,461.91800694676000-5,-46.062616520627500-5,
      *3.24603288210051D-5,-17619.46907762150-10,760.81635924190-10,
      *-26.79253530960-10,78436.953140-15,-1943.834690-15,
      *41.253210-15,-75885.D-20,1222.D-20,-17.D-20/,
      *DPO(14)/1.99892069869504D0,-53.65220468132120-5,
      *30751.84787519470-10,-517.05945376060-10,16.30646463520-10,
      *-78640.91377D-15,5168.262390-15,-430.457890-15,43.265960-15,
      *-5.069030-15,67481.D-20,-10912.D-20,1631.D-20,-288.D-20/,
      *DQ0(14)/-3111.17092106740D-5,6.83851994261165D-5,
      *-7414.49941106060-10,179.72457247970-10,-7.27191593690-10,
      *42201.219050-15,-3206.74742D-15,300.614510-15,-33.363280-15,
      *4.255230-15,-60999.D-20,9662.D-20,-1669.D-20,311.D-20/
       DATA DPI/3.141592653589797/,IFLAG/-1/
C   CHECK TO SEE IF ROUTINE HAS BEEN CALLED BEFORE
       IF(IFLAG .NE. -1) GOTO 5
C   PERFORM INITIALIZATION AND RESET FLAG
       DCONST=DSQRT(2.D0/DPI)
       DPID4=DPI/4.D0
       DPC(1)=DPO(1)/2.D0
       DQO(1)=DQO(1)/2.D0
       IFLAG=1
     5 DJ0LK=1.D0
C   CHECK FOR ARGUMENT EQUAL TO ZERO
       IF(DX .EQ. 0.D0) RETURN
C   DECIDE IF JACOBI OR ASYMPTOTIC SERIES WILL BE USED
       IF(DABS(DX) .GT. 8.D0) GOTO 10
C   USE JACOBI SERIES
C   FORM THE ARGUMENT FOR THE CHEBYSHEV POLYNOMIALS
       DXD8=DX/8.D0
       DARG=2.D0*DXD8*DXD8-1.D0
C   SUM THE POLYNOMIALS
       CALL DCNPS(DJ0LK,DARG,DB,18)
    99 RETURN
C   USE MODIFIED ASYMPTOTIC SERIES
    10 D8DX=8.D0/DX
       DARG=2.D0*D8DX*D8DX-1.D0
C   SUM THE POLYNOMIALS FOR P0(X)
       CALL DCNPS(DP,DARG,DPO,14)
C   SUM THE POLYNOMIALS FOR Q0(X)
       CALL DCNPS(DQ,DARG,DQO,14)
       DQ=DQ*D8DX
C   NOW FORM ASYMPTOTIC APPROXIMATION TO J0(X)
       DJ0LK=(DCONST*(DP*DCOS(DX-DPID4)-DQ*DSIN(DX-DPID4)))/DSQRT(DX)
       RETURN
       END
       DOUBLE PRECISION FUNCTION DFCT(I)
C   FUNCTION TO EVALUATE THE INDIVIDUAL TERMS IN THE SERIES OF MAGNETIC
C    FIELD INTENSITIES (EITHER REAL OF IMAGINARY) ARISING FROM THE
C    INVERSE HANKEL INTEGRATION BETWEEN THE LIMITS OF LAMBDA SUB(I)
C    AND LAMBDA SUB(I+1).  SEE THE PAPER DATED JULY 25.
C
       IMPLICIT REAL*8 (D)
       REAL*8 DARRAY(100)
       COMMON DARRAY
       DFCT=DARRAY(I)
       RETURN
       END
```

```
      SUBROUTINE DTEUL(FCT,SUM,MAX,EPS,IER,N)
C   COPIED EULER CONVERGENCE ACCELERATION SUBROUTINE
      DIMENSION Y(15)
      DOUBLE PRECISION FCT,SUM,Y,AMN,AMP
      IF(MAX)1,1,2
    1 IER=-1
      GOTO 12
C   INITIALIZE EULER TRANSFORMATION
    2 IER=1
      I=1
      M=1
      N=1
      Y(1)=FCT(N)
      SUM=Y(1)*.5D0
C   START EULER LOOP
    3 J=0
    4 I=I+1
      IF(I-MAX)5,5,12
    5 N=I
      AMN=FCT(I)
      DO 6 K=1,M
      AMP=(AMN+Y(K))*.5D0
      Y(K)=AMN
    6 AMN=AMP
C   CHECK EULER TRANSFORMATION
      IF(DABS(AMN)-DABS(Y(M)))7,9,9
    7 IF(M-15)8,9,9
    8 M=M+1
      Y(M)=AMN
      AMN=.5D0*AMN
C   UPDATE SUM
    9 SUM=SUM+AMN
      IF(ABS(SNGL(AMN))-EPS*ABS(SNGL(SUM)))10,10,3
C   TEST END OF PROCEDURE
   10 J=J+1
      IF(J-5)4,11,11
   11 IER=0
   12 RETURN
      END
      SUBROUTINE DGAUSS(DLOWER,DUPPER,DFUN,DRELER,DABSER,DINT,DERR,
     *     IFLAG)
C   SUBROUTINE TO ESTIMATE THE INTEGRAL OF THE FUNCTION DFUN BETWEEN THE
C    LIMITS DLOWER AND DUPPER.
C    PARAMETERS DRELER AND DABSER ARE THE USER REQUESTED RELATIVE AND
C    ABSOLUTE ERRORS IN THE ESTIMATED VALUE OF THE INTEGRAL DINT.  IF
C    DABSER=0, ONLY THE RELATIVE ERROR CRITERION IS USED.  COMPUTATION
C    STOPS WHEN EITHER THE ABSOLUTE ERROR CRITERION OR THE RELATIVE
C    ERROR CRITERION HAS BEEN ESTIMATED TO BE ACHIEVED.
C    PARAMETER DERR IS THE RETURNED ESTIMATE OF THE ABSOLUTE ERROR IN
C    DINT.  PARAMETER IFLAG IS SET TO ZERO IF NO CONVERGENCE IS OBTAINED;
C    OTHERWISE, IFLAG INDICATES THE NUMBER OF INTEGRAL ESTIMATES
C    CALCULATED MINUS 1.
C   SUBPROGRAMS REQUIRED -  DFUN,DGQUAD,CONVT
C   REF:  "GAUSSIAN QUADRATURE FORMULAS", BY STROUD AND SECREST
C         (THE FUNCTION ARGUMENTS AND THEIR WEIGHTS WERE TAKEN FROM
C         THIS BOOK.)
C
      IMPLICIT REAL*8 (D)
      REAL*8 DGX12(6),DGW12(6),DGX16(8),DGW16(8),DGX24(12),DGW24(12),
     *DGX32(16),DGW32(16),DGX40(20),DGW40(20)
      DATA DGX12/.981560634246719,.904117256370475,.769902674194305,
     *.587317954286617,.367831498998180,.125233408511469/
      DATA DGW12/.4717533638651180-1,.106939325995318,
     *.160078328543346,.203167426723066,.233492536538355,
     *.249147045813403/
      DATA DGX16/.989400934991650,.944575023073233,.865631202387832,
     *.755404408355003,.617876244402644,.458016777657227,
     *.281603550779259,.950125098376374D-1/
      DATA DGW16/.2715245941175410D-1,.6225352393864790D-1,
     *.9515851168249280D-1,.124628971255534,.149595988816577,
     *.169156519395003,.182603415044924,.189450610455068/
      DATA DGX24/.995187219997021,.974728555971309,
     *.938274552002733,.886415527004401,.820001985973903,
     *.740124191578554,.648093651936976,.545421471388840,
     *.433793507626045,.315042679696163,.191118867473616,
     *.640568928626056D-1/
      DATA DGW24/.1234122979998720D-1,.2853138862893370D-1,
     *.4427743881741980D-1,.5929858491543680D-1,.7334648141108030D-1,
     *.8619016153195330D-1,.9761865210411390D-1,.107444270115966,
     *.115505668053726,.121670472927803,.125837456346828,
     *.127938195346752/
      DATA DGX32/.997263861849482,.985611511545268,
     *.964762255587506,.934906075937740,.896321155766052,
     *.849367613732570,.794483795967942,.732182118740290,
     *.663044266930215,.587715757240762,.506899908932229,
     *.421351276130635,.331868602282128,
     *.239287362252137,.144471961582796,.483076656877383D-1/
```

```
      DATA DGW32/.7018610009470100D-2,.1627439473090570D-1,
     *.2539206530926210D-1,.3427386291302140D-1,.4283589802222670D-1,
     *.5099805926237620D-1,.5868409347853550D-1,.6582222277636180D-1,
     *.7234579410884850D-1,.7819389578707030D-1,.8331192422694680D-1,
     *.8765209300440380D-1,.9117387869576390D-1,.9384439908080460D-1,
     *.9563872007927490D-1,.9654008851472780D-1/
      DATA DGX40/.998237709710559,.990726238699457,
     *.977259949983774,.957916819213792,.932812808278677,
     *.902098806968874,.865959503212260,.824612230833312,
     *.778305651426519,.727318255189927,.671956684614180,
     *.612553889667980,.549467125095128,.483075801686179,
     *.413779204371605,.341994090825758,.268152185007254,
     *.192697580701371,.116084070675255,.3877241750605080D-1/
      DATA DGW40/.4521277098533190D-2,.1049828453115280D-1,
     *.1642105838190790D-1,.2224584919416700D-1,.2793700698002340D-1,
     *.3345019524254780D-1,.3878216797447200D-1,.4387090818567330D-1,
     *.4869580763507220D-1,.5322784698393680D-1,.5743976909939160D-1,
     *.6130624249292890D-1,.6480401345660100D-1,.6791204581523390D-1,
     *.7061164739128680D-1,.7286532395804100D-1,.7472316905796830D-1,
     *.7611036190062620D-1,.7703981816424800D-1,.7750594797842480D-1/
      EXTERNAL DFUN
C   CALCULATE THE 12 POINT AND 16 POINT INTEGRAL ESTIMATES
      DINT12=DGQUAD(DLOWER,DUPPER,DFUN,6,DGX12,DGW12)
      DINT16=DGQUAD(DLOWER,DUPPER,DFUN,8,DGX16,DGW16)
C   DETERMINE WHETHER CONVERGENCE WAS OBTAINED
      CALL CONVT(DINT12,DINT16,DRELER,DABSER,DERR,ICONV)
      IF(ICONV .NE. 1) GOTO 10
C   CONVERGENCE - SET UP VALUES, AND RETURN
      IFLAG=1
      DINT=DINT16
      RETURN
C
C   NO CONVERGENCE - CALCULATE THE 24 POINT INTEGRAL ESTIMATE
   10 DINT24=DGQUAD(DLOWER,DUPPER,DFUN,12,DGX24,DGW24)
C   DETERMINE WHETHER CONVERGENCE WAS OBTAINED
      CALL CONVT(DINT16,DINT24,DRELER,DABSER,DERR,ICONV)
      IF(ICONV .NE. 1) GOTO 20
C   CONVERGENCE - SET UP VALUES, AND RETURN
      IFLAG=2
      DINT=DINT24
      RETURN
C
C   NO CONVERGENCE - CALCULATE THE 32 POINT INTEGRAL ESTIMATE
   20 DINT32=DGQUAD(DLOWER,DUPPER,DFUN,16,DGX32,DGW32)
C   DETERMINE WHETHER CONVERGENCE WAS OBTAINED
      CALL CONVT(DINT24,DINT32,DRELER,DABSER,DERR,ICONV)
      IF(ICONV .NE. 1) GOTO 30
C   CONVERGENCE - SET UP VALUES, AND RETURN
      IFLAG=3
      DINT=DINT32
      RETURN
C
C   NO CONVERGENCE - CALCULATE THE 40 POINT INTEGRAL ESTIMATE
   30 DINT40=DGQUAD(DLOWER,DUPPER,DFUN,20,DGX40,DGW40)
C   DETERMINE WHETHER CONVERGENCE WAS OBTAINED
      CALL CONVT(DINT32,DINT40,DRELER,DABSER,DERR,ICONV)
      IF(ICONV .NE. 1) GOTO 40
C   CONVERGENCE - SET UP VALUES, AND RETURN
      IFLAG=4
      DINT=DINT40
      RETURN
C
C   NO CONVERGENCE
   40 IFLAG=0
      DINT=DINT40
      RETURN
      END
      SUBROUTINE CONVT(DOLD,DNEW,DRELER,DABSER,DERR,ICONV)
C   SUBROUTINE TO TEST CONVERGENCE FOR THE SUBROUTINE DGAUSS.  DOLD AND
C    DNEW ARE THE PREVIOUS AND PRESENT ESTIMATES OF THE INTEGRAL.
C   REF:  MY PAPER DATED AUG 22.
C
      IMPLICIT REAL*8 (D)
      ICONV=1
      DERR=DABS(DNEW-DOLD)
C   IF THE PRESENT INTEGRAL ESTIMATE IS EQUAL TO ZERO, PROCEED TO THE
C    ABSOLUTE ERROR TEST (AFTER MAKING SURE THAT DABSER .NE. 0).
      IF(DNEW .EQ. 0.D0) GOTO 10
C   ESTIMATE NOT EQUAL TO ZERO - CHECK THE RELATIVE ERROR CRITERION
      IF(DERR/DABS(DNEW) .LE. DRELER) RETURN
C   NO RELATIVE ERROR CONVERGENCE - IF DABSER=0, THEN THERE IS NO
C    CONVERGENCE.
   10 IF(DABSER .EQ. 0.D0) GOTO 20
C   CHECK THE ABSOLUTE ERROR CRITERION.
      IF(DERR .LE. DABSER) RETURN
```

```
C   NO CONVERGENCE
 20 ICONV=0
    RETURN
    END
    DOUBLE PRECISION FUNCTION DGQUAD(DLOWER,DUPPER,DFUN,NPTD2,DGX,
   *        DGW)
C   FUNCTION SUBPROGRAM TO ESTIMATE THE INTEGRAL FROM DLOWER TO DUPPER
C    OF THE FUNCTION DFUN USING GAUSSIAN QUADRATURE WITH 2*NPTD2 POINTS.
C    ARRAYS DGX AND DGW CONTAIN THE NORMALIZED ARGUMENTS ON THE INTERVAL
C    (0,1) (WITH DGX(1) THE POINT CLOSEST TO 1) AND THE RESPECTIVE
C    WEIGHTS.
C   REF:  NUMERICAL METHODS, BY HORNBECK, SECTION 8.4 P. 154.
C         MY PAPER DATED AUG22.
C
    IMPLICIT REAL*8 (D)
    REAL*8 DGX(NPTD2),DGW(NPTD2)
C   CALCULATE THE CONSTANTS USED IN FORMING THE ARGUMENTS OF DFUN.
    DC1=(DUPPER+DLOWER)/2.D0
    DC2=DC1-DLOWER
C   NOW PERFORM THE INTEGRATION
    DGQUAD=0.D0
    DO 10 I=1,NPTD2
 10 DGQUAD=DGQUAD+DGW(I)*(DFUN(DC1+DC2*DGX(I))+DFUN(DC1-DC2*DGX(I)))
    DGQUAD=DGQUAD*DC2
    RETURN
    END
```

ORIGINAL PAGE IS
OF POOR QUALITY

APPENDIX E

FORTRAN SOURCE CODE FOR CALCULATING FORCE AT TIME T=50 MICROSECONDS

```
C    FILE:   FORWU FORTRAN              V1.1
C    PROGRAM TO ESTIMATE THE TOTAL FORCE BETWEEN THE COIL AND THE SKIN
C     BY CALCULATING   (10**7)/4   TIMES THE ESTIMATE OF THE INTEGRAL OF
C           BR*BR*R - BZ*BZ*R
C     BETWEEN R=.01  AND R=1.9 INCHES.
C    REF:  MY PAPER DATED JAN 13 '86.
C
        REAL BR50N(11)/.017014,.306449,.459552,.503336,.461798,.287143,
       *.128437,.048180,.025120,.014479,.008802/
        REAL BZ50N(11)/.224464,.213477,.142827,.082718,.033232,-.031324,
       *-.047354,-.017196,-.006434,-.002941,-.001629/
        REAL BR50NS(11),CR50NS(11),DR50NS(11),BZ50NS(11),CZ50NS(11),
       *DZ50NS(11)
        REAL RR(11)/.01,.2,.4,.6,.8,1.,1.2,1.4,1.6,1.8,2./
        REAL RZ(11)/.01,.1,.3,.5,.7,.9,1.1,1.3,1.5,1.7,1.9/
        REAL MONTH/' JAN'/,DATE/' 17 '/
        DATA CONST/2.5E6/,TOMTRS/.0254/,TOLBS/.2248/
        N=11
C    SQUARE THE CALCULATED B FIELDS
        DO 10  I=1,11
        BR50N(I)=BR50N(I)*BR50N(I)
     10 BZ50N(I)=BZ50N(I)*BZ50N(I)
C    CHANGE THE RADII AT WHICH THE B FIELDS WERE CALCULATED FROM INCHES
C     TO METERS
        DO 15  I=1,11
        RR(I)=RR(I)*TOMTRS
     15 RZ(I)=RZ(I)*TOMTRS
C    FIT SPLINE FUNCTIONS TO BR*BR AND BZ*BZ
        CALL  SPLINE(N,RR,BR50N,BR50NS,CR50NS,DR50NS)
        CALL  SPLINE(N,RZ,BZ50N,BZ50NS,CZ50NS,DZ50NS)
C
C    PERFORM THE INTEGRATIONS
C
        RINT50=0.
        ZINT50=0.
C    LOOP TO ADD THE CONTRIBUTIONS TO THE INTEGRAL BETWEEN KNOTS
        DO 20  I=1,10
        IP1=I+1
        RINT50=RINT50+SPLINT(I,RR(IP1),RR(I),BR50N(I),BR50NS(I),CR50NS(I),
       *   DR50NS(I))
     20 ZINT50=ZINT50+SPLINT(I,RZ(IP1),RZ(I),BZ50N(I),BZ50NS(I),CZ50NS(I),
       *   DZ50NS(I))
C
C    DONE EXCEPT FOR MULTIPLICATION BY CONSTANT
C
        F50MET=CONST*(RINT50-ZINT50)
        F50LBS=F50MET*TOLBS
        WRITE(6,1000) MONTH,DATE,F50MET,F50LBS
   1000 FORMAT('1OUTPUT FROM FORWU FORTRAN V1.1',10X,A4,A4,//' TOTAL FORCE
       * AT 50USEC IS ',F9.4,' NEWTONS',/,T25,'= ',F9.4,' POUNDS',//)
        STOP
        END

        FUNCTION SPLINT(I,RUP,RLO,F,B,C,D)
C    FORTRAN SUBPROGRAM TO EVALUATE THE INTEGRAL OF      F(R) * R
C     OVER THE INTERVAL  RLO .LE. R .LE. RUP  WITH
C       I = SPLINE FUNCTION INDEX CORRESPONDING TO THIS INTERVAL
C       RUP = UPPER INTEGRATION LIMIT (A KNOT)
C       RLO = LOWER INTEGRATION LIMIT (A KNOT)
C       F = F(RLO)
C       B = B(I) IN THE SPLINE INTERPOLATING POLYNOMIAL OF F(R)
C       C = C(I) IN THE SPLINE ...
C       D = D(I) IN THE SPLINE ...
C     ASSUMES A CUBIC SPLINE INTERPOLATING POLYNOMIAL AS DESCRIBED IN
C     "COMPUTER METHODS FOR MATHEMATICAL COMPUTATIONS", BY FORSYTHE ET.
C     AL.
C    REF:  MY PAPER DATED JAN 14 86.
```

```
      RLO2=RLO*RLO
      RLO3=RLO2*RLO
      RLO4=RLO3*RLO
      RLO5=RLO4*RLO
      RUP2=RUP*RUP
      RUP3=RUP2*RUP
      RUP4=RUP3*RUP
      RUP5=RUP4*RUP
C   CALCULATE FIRST TERM
      SPLINT=(((D*RLO-C)*RLO+B)*RLO-F)*(RLO2-RUP2)/2.
C   ADD SECOND TERM
      SPLINT=SPLINT+((3.*D*RLO-2.*C)*RLO+B)*(RUP3-RLO3)/3.
C   ADD THIRD TERM
      SPLINT=SPLINT-(3.*D*RLO-C)*(RUP4-RLO4)/4.
C   ADD FOURTH TERM; DONE
      SPLINT=SPLINT+D*(RUP5-RLO5)/5.
      RETURN
      END

      SUBROUTINE SPLINE(N,X,Y,B,C,D)
C   COPIED SUBROUTINE SPLINE FOLLOWS
      INTEGER N
      REAL X(N),Y(N),B(N),C(N),D(N)
      INTEGER NM1, IB, I
      REAL T
      NM1=N-1
      IF(N.LT.2)RETURN
      IF(N.LT.3)GO TO 50
      D(1)=X(2)-X(1)
      C(2)=(Y(2)-Y(1))/D(1)
      DO 10 I = 2, NM1
         D(I) = X(I+1)-X(I)
         B(I) = 2.*(D(I-1)+D(I))
         C(I+1) = (Y(I+1)-Y(I))/D(I)
         C(I) = C(I+1)-C(I)
   10 CONTINUE
      B(1)=-D(1)
      B(N)=-D(N-1)
      C(1)=0.
      C(N)=0.
      IF(N.EQ.3) GO TO 15
      C(1)=C(3)/(X(4)-X(2)) - C(2)/(X(3)-X(1))
      C(N)=C(N-1)/(X(N)-X(N-2)) - C(N-2)/(X(N-1)-X(N-3))
      C(1)=C(1)*D(1)**2/(X(4)-X(1))
      C(N)=-C(N)*D(N-1)**2/(X(N)-X(N-3))
   15 DO 20 I = 2, N
         T=D(I-1)/B(I-1)
         B(I)=B(I)-T*D(I-1)
         C(I)=C(I)-T*C(I-1)
   20 CONTINUE
      C(N)=C(N)/B(N)
      DO 30 IB= 1, NM1
       I=N-IB
       C(I)=(C(I)-D(I)*C(I+1))/B(I)
30 CONTINUE
   B(N) = (Y(N)-Y(NM1))/D(NM1) + D(NM1)*(C(NM1) + 2.*C(N))
   DO 40 I = 1, NM1
      B(I) = (Y(I+1)-Y(I))/D(I) - D(I)*(C(I+1)+2.*C(I))
      D(I) = (C(I+1)-C(I))/D(I)
      C(I)=3.*C(I)
40 CONTINUE
   C(N)=3.*C(N)
   D(N)=D(N-1)
   RETURN
50 B(1)=(Y(2)-Y(1))/(X(2)-X(1))
   C(1)=0.
   D(1)=0.
   B(2)=B(1)
   C(2)=0.
   D(2)=0.
   RETURN
   END
```

APPENDIX F

NOTATION AND LIST OF SYMBOLS

Unless stated otherwise, the rationalized MKS system is used in all equations and calculations. Equations are numbered consecutively, beginning with (1) in each chapter. Only those equations that are referenced in the text are numbered. Figures are identified by two alphanumeric characters. The first character is a number, indicating the number of the chapter in which the figure appears. The second character is a letter, alphabetically identifying the order in which the figures appear.

A chapter by chapter summary of the symbols used in this dissertation, listed in the order of their appearance, follows.

Chapter One

$Z(\omega)$	Terminal coil impedance (page 7)
ω	Radian frequency (Fourier transform) variable (page 7)
$i(t)$	Time domain coil current (page 7)
$I(\omega)$	Fourier transform of $i(t)$ (page 7)
$E_\phi(z,r,t)$	Azimuthal real space component of the electric intensity (page 7)
z	Axial coordinate in cylindrical coordinate system (page 7)
r	Radial coordinate in cylindrical coordinate system (page 7)

$H_r(z,r,t)$ Radial real space component of the magnetic intensity (page 7)

$H_z(z,r,t)$ Axial real space component of the magnetic intensity (page 7)

$f(t)$ Separation force magnitude between the coil and metal target (page 7)

Γ Impulse delivered to metal target by the coil (page 7)

<u>Chapter Three</u>

R_1 Inner coil radius (page 12)

R_2 Outer coil radius (page 12)

h Coil axial width (page 12)

d Metal target thickness (page 12)

ϕ Azimuthal coordinate in cylindrical coordinate system (page 12)

μ Permeability of free space (all materials considered in this dissertation are non-magnetic) (page 14)

σ Conductivity of metal target (page 14)

j Principal square root of -1 (page 15)

$J_n(x)$ Bessel function of the first kind of order n (page 15)

λ Hankel transform variable (page 15)

$\hat{V}$ Total Fourier-Hankel space transmission line voltage (page 16)

$\hat{I}$ Total Fourier-Hankel space transmission line current (page 16)

γ Fourier-Hankel space transmission line complex propagation coefficient (page 17)

$\hat{I}_{o+}$ Fourier-Hankel space transmission line phasor current corresponding to propagation in the direction of increasing z (page 17)

$\hat{I}_{o-}$ Fourier-Hankel space transmission line phasor current corresponding to propagation in the direction of decreasing z (page 17)

$\hat{V}_{o+}$	Fourier-Hankel space transmission line phasor voltage corresponding to propagation in the direction of increasing z (page 18)
$\hat{V}_{o-}$	Fourier-Hankel space transmission line phasor voltage corresponding to propagation in the direction of decreasing z (page 18)
Z_o	Fourier-Hankel space transmission line characteristic impedance (page 19)
$\tilde{I}$	Fourier space phasor current (page 19)
g	Distance between metal target and the current sheet closest to target (page 20)
z_o	Axial coordinate of current sheet closest to target (page 20)
z_1	Axial coordinate of center current sheet (page 20)
z_2	Axial coordinate of current sheet furthest from target (page 20)

<u>Chapter Four</u>

$\tilde{V}$	Fourier space phasor voltage (page 23)
Z_a	Fourier-Hankel space air transmission line characteristic impedance (page 26)
γ_a	Fourier-Hankel space air transmission line complex propagation coefficient (page 26)
Z_m	Fourier-Hankel space metal transmission line characteristic impedance (page 26)
γ_m	Fourier-Hankel space metal transmission line complex propagation coefficient (page 26)
Z(0)	Fourier-Hankel space impedance seen looking into metal transmission line at z=0 in Figure 3C (page 26)
ρ_H	Fourier-Hankel space current reflection coefficient (page 26)
ρ_E	Fourier-Hankel space voltage reflection coefficient (page 28)
$\hat{V}_a$	Fourier-Hankel space total voltage at coil side face of metal target (page 30)

$\hat{V}_f$ Fourier-Hankel space total voltage on face of target opposite coil (page 30)

$\hat{I}_n$ Fourier-Hankel space total current at coil side face of metal target (page 30)

$\hat{I}_f$ Fourier-Hankel space total current on face of target opposite coil (page 30)

$\overline{F}$ Vector force on metal target (page 32)

ε Permittivity of free space (all materials considered in this dissertation have a relative permittivity of 1) (page 32)

Chapter Five

r_1 Radius of inner loop of wire in field measuring plate (page 38)

r_2 Radius of outer loop of wire in field measuring plate (page 38)

h Distance between two loops of wire of the same radius on front and back sides of field measuring plate (page 38)

Chapter Six

$R(\omega)$ Real part of the total coil impedance (page 47)

$L(\omega)$ Inductance of coil (page 47)

V_o Initial voltage on energy storage capacitor prior to discharge (page 47)

$\delta(\omega)$ Dirac delta distribution (page 47)

$V_c(\omega)$ Fourier transform of energy storage capacitor voltage (page 47)

C Capacitance of energy storage capacitor (page 48)

R_{ac} AC winding resistance of the coil (page 48)

$Real\{\}$ Symbol denoting "real part of $\{\ \}$" (page 48)

I_o Instantaneous current in coil when clamp diode across energy storage capacitor begins conducting (page 51)

Appendix C

$H_n(x)$	Struve function of order n (page 80)
$T_n(x)$	Chebyshev polynomial of the first kind of order n (page 80)
$Y_n(x)$	Bessel function of the second kind of order n (page 81)
$A_n(x)$	Partial sum associated with the Jacobi series expansion of $H_n(x)-Y_n(x)$ (page 81)

REFERENCES

[1] R. D. Rudich, "Weather-Involved U.S. Air Carrier Accidents 1962 - 1984 *A Compendium and Brief Summary*", *American Institute of* Aeronautics and Astronautics paper number AIAA-86-0327, January, 1986.

[2] British Patent Specification No. 505,433 issued to Rudolf Goldschmidt; May 5, 1939.

[3] Dr. Robert Schrag, unpublished paper, "Experimental Study of the "Electro-Impulse Process by Magnetic Field Diagnostics", summarized in NASA CR 174919, May, 1985.

[4] M.H.S. El-Markabi and E.M. Freeman, "Electromagnetic Properties of a Circular Cylindrical Coil in a Set of Planar Ferromagnetic Regions", IEE Proc., Vol. 129, Pt. A, No. 8, Nov., 1982.

[5] General Electric Co., SCR Manual - Fifth Edition, Syracuse Park, N.Y., 1972.

[6] Richard G. Hoft, ed., SCR Applications Handbook, International Rectifier Corp., El Segundo, Ca., 1977.

[7] RCA Solid State Division, Solid State Devices Manual, Somerville, N.J., 1975.

[8] Samuel Levy, "Electromagnetic Shielding Effect of an Infinite Plane Conducting Sheet Placed Between Circular Coaxial Coils", Proceedings of the Institute of Radio Engineers, Vol. 24, No. 6, June, 1936.

[9] F.W. Grover, Inductance Calculations - Working Formulae and Tables, Dover, 1962.

[10] C.V. Dodd and W.E. Deeds, "Analytical Solutions to Eddy-Current Probe-Coil Problems", Journal of Applied Physics, Vol. 39, No. 6, May, 1968.

[11] M. Onoe, "Analysis of Finite Solenoid Coil Near a Conductor", Electr. Eng. Jpn., 88, 1968.

[12] Ian N. Sneddon, The Use of Integral Transforms, McGraw Hill Book Co., 1972.

[13] Robert A. Chipman, *Transmission* Lines, McGraw Hill Book Co., 1968.

[14] Robert Grover Brown, Robert A. Sharpe, William Lewis Hughes, and Robert E. Post, Lines, Waves, and Antennas: The Transmission of Electric Energy, 2nd. ed., Ronald Press, 1973.

[15] Richard E. Matick, Transmission Lines for Digital and Communication Networks, McGraw Hill Book Co., 1969.

[16] F.B. Hildebrand, Advanced Calculus for Applications, 2nd. edn., Prentice Hall, 1976.

[17] Murray R. Spiegel, Mathematical Handbook of Formulas and Tables, McGraw Hill Book Co., 1968.

[18] Arthur Erdelyi, ed., Higher Transcendental Functions, Vol. II, Bateman Manuscript Project, McGraw Hill Book Co., 1953.

[19] G.N. Watson, A Treatise on the Theory of Bessel Functions, 2nd. edn., Cambridge University Press, 1980.

[20] Milton Abramowitz and Irene A. Stegun, Handbook of Mathematical Functions with Formulas, Graphs, and Mathematical Tables, Dover Publications Inc., 1965.

[21] Robert W. Hornbeck, Numerical Methods, Prentice Hall, 1975.

[22] ACM Algorithms Distribution Service, IMSL Inc., Sixth Floor, NBC Building, 7500 Bellaire Boulevard, Houston, Texas, 77036.

[23] International Mathematical and Statistical Library (IMSL) Inc., Sixth Floor, NBC Building, 7500 Bellaire Boulevard, Houston, Texas, 77036.

[24] John R. Rice, Numerical Methods, Software, and Analysis, McGraw Hill Book Co., 1983.

[25] George E. Forsythe, Michael A. Malcolm, and Cleve B. Moler, Computer Methods for Mathematical Computations, Prentice Hall, 1977.

[26] Peter Henrici, Essentials of Numerical Analysis, John Wiley and Sons, 1982.

[27] Avram Sidi, "Extrapolation Methods for Oscillatory Infinite Integrals", Journal of the Institute of Mathematics and its Applications, vol. 26, 1980.

[28] David Levin and Avram Sidi, "Two New Classes of Nonlinear Transformations for Accelerating the Convergence of Infinite Integrals and Series", Applied Mathematics and Computation, vol. 9, 1981.

[29] Avram Sidi, "The Numerical Evaluation of Very Oscillatory Infinite Integrals by Extrapolation", Mathematics of Computation, Vol. 38, No. 158, April 1982.

[30] William F. Ford and Avram Sidi, "An Algorithm for a Generalization of the Richardson Extrapolation Process" (to be published).

[31] A. H. Stroud and D. Secrest, Gaussian Quadrature Formulas, Prentice Hall, 1966.

[32] Personal conversation with Dr. Avram Sidi, The Technion, Israel Institute of Technology, Haifa, Israel.

[33] J. H. Wilkinson, Rounding Errors in Algebraic Processes, Prentice Hall, 1963.

[34] Frances B. Hildebrand, Introduction to Numerical Analysis, 2nd. edn., McGraw-Hill Book Co., 1974.

[35] Mark Jong, Methods of Discrete Signal and System Analysis, McGraw-Hill Book Co., 1982.

[36] Janet P. Mason, A Fortran Subroutine to Evaluate Struve Functions for Integer Orders and Positive Real Arguments, NRL Memorandum Report 3181, Research Computation Center, Naval Research Laboratory, Washington, D.C., December 1975.

[37] Yudell Luke, The Special Functions and their Approximations, Vol. II, Mathematics in Science and Engineering, Vol. 53-II, Academic Press, 1969.

[38] Cornelius Lanczos, Applied Analysis, Prentice Hall, 1956.

[39] C.W. Clenshaw, Mathematical Tables, Vol. 5, Chebyshev Series for Mathematical Functions, Her Majesty's Stationery Office, London, 1962.

[40] John F. Hart et. al., Computer Approximations, John Wiley and Sons, 1968.

[41] J.A. Stratton, Electromagnetic Theory, McGraw-Hill Book Co., 1941.

[42] R.L. Schrag and G.W. Zumwalt, "Electro-Impulse Deicing: Concept and Electrodynamic Studies", American Institute of Aeronautics and Astronautics paper number 84-0021, January, 1984.

[43] R.M. Bowley, P.J. King, G.J. Lewis, and I.J. Shellard, "Production of Short Mechanical Impulses by Means of Eddy Currents", Proc. IEE, Vol. 130, Pt. B, No. 6, Nov. 1983.

[44] G.J. Lewis, "The Electrodynamic Operation of Electro-Impulse De-Icing Systems", American Institute of Aeronautics and Astronautics paper AIAA-86-0547, January, 1986.